Long-term measurements of global horizontal and tilted solar irradiance for Photovoltaic Applications

Von der Fakultät für Mathematik und Physik
der Gottfried Wilhelm Leibniz Universität Hannover
zur Erlangung des Grades

Doktor der Naturwissenschaften
Dr. rer. nat.

genehmigte Dissertation
von

Dipl.-Met. Riyad Mubarak

2021

Abstract

In the past four decades, great efforts have been made worldwide to collect accurate ground-based measurements of solar radiation. This comes in light of the growing interest in climate change, of which solar radiation is a critical factor. At the same time, solar-radiation-based energy is one of the most promising energy alternatives to fossil fuels. This present thesis is primarily based on irradiance data collected at different orientations. The measurements were conducted over several years in Hannover, Germany, through the use of silicon solar sensors and thermopile pyranometers to investigate the following research questions: (1) How accurate are the transposition models that estimate the global and diffuse solar irradiance on tilted planes; (2) is there an alternative concept for increasing self-consumption via use another orientation of photovoltaic (PV) systems than the south direction; and (3) how accurate are the silicon-based irradiance sensors, and what is the deviation to thermopile sensors?

To answer the first question, the performance of five well-known and widely used transposition models that estimate the global and diffuse solar irradiance on tilted planes based on the global horizontal irradiance was assessed. The models were selected if there were sufficient input data available at the examined measurement sites, and because they present the three most common model types: isotropic, anisotropic with two components, and anisotropic with three components. The modeled tilted irradiance values are compared to measured one-minute values at different tilt angles at Hannover (Germany) and NREL (Golden, CO, USA). It has been found that particularly the assumption of an isotropic distribution of diffuse irradiance according to the analytic approach of Liu & Jordan leads to an underestimation of the results compared to measurement data. In comparison to the isotropic models, it has been shown that the anisotropic models overestimate the irradiance of south-facing sensors and most of the vertically tilted sensors. The deviations of the anisotropic models from the measurements grow with increasing deviation from the southern direction. It has also clearly shown that the basic criteria for selecting the most suitable model for simulating the electrical output of a PV module is its ability to simulate the diffuse radiation of the sky under all kinds of weather conditions.

In the next part of the thesis, it has been sought to answer the second research question by comparing different orientations of PV systems in respect to their generated energy, self-consumption (SC), and degree of Autarky (AD). The measured irradiance has been used to evaluate the generated photovoltaic energy at various orientations and tilt angles. The SC of the all of the orientations is calculated by using a set of separately measured load profiles from household load data in order to evaluate the most economic orientations for rooftop PV systems. It has been found that south-oriented (S) collectors provide the highest electrical power during the day, whereas combinations of east and west orientations (E-W) result in the highest SC; combinations of southeast and southwest (SE-SW) orientations result in the highest AD, although SE-SW orientations reduce the yearly PV Power by 5-6%. The economic analysis of PV systems without feed-in tariff (FIT) indicates that the SE-SW and E-W combinations have the lowest electricity cost, compared to the S orientation at the same tilt. For PV systems with FIT, the S orientation presently provides the highest transfer of money from the supplier. However, as a result of the continuing decline of FIT, the economic advantage of S orientation is decreasing. E-W and SE-SW orientations are more beneficial for the owner once FIT decreases to 7 Ct/kWh. Further, two types of prevalent PV software (PVSOL and PVsyst) were used to simulate the system performance. A comparison with measurements showed that both types of PV software underestimate SC and AD for all the studied orientations, leading to the conclusion that improvements are necessary in modeling.

In terms of the third research question regarding the uncertainty of silicon-based sensors, the global horizontal irradiance (GHI) of the silicon-based sensor (SiS) was compared to those measured by the thermopile pyranometer (Pyr). It has been found that GHI measured by the thermopile pyranometer is generally higher than the uncorrected SiS irradiance; the monthly differences range between 3.7% in July and 17.1% in January, while the average annual Pyr irradiation is 6.5% higher. However, the SiS measured higher irradiance than Pyr during overcast days. Based on the differences between both sensors, a correction model to minimize these discrepancies was proposed. The goal of this model is to equip silicon sensors for radiometric measurements in order to mimic thermopile sensors. Applying the correction model to the SiS irradiance, improved the matching of the two kinds of sensor measurements. The difference in daily measurements of global horizontal irradiance under clear sky conditions between both sensors decreases to be within ± 2.0 % during most times of the day. The difference in total annual irradiation decreases from 70 kWh/m^2 (6.5%) to 15 kWh/m^2 (1.5%) due to the correction.

Kurzfassung

In den letzten vier Jahrzehnten wurden große Fortschritte im Hinblick auf die präzisen Bodenmessungen der Solarstrahlung gemacht. Dies beruht zum großen Teil auf dem wachsenden Interesse am Klimawandel, für den die Solarstrahlung ein kritischer Faktor ist. Gleichzeitig ist die auf Sonnenstrahlung basierende Energie eine der vielversprechendsten Energiealternativen zu fossilen Brennstoffen. Diese Arbeit basiert im Wesentlichen auf Bestrahlungsstärkedaten, die in unterschiedlichen Ausrichtungen gesammelten wurden. Die Messungen wurden über viele Jahre hinweg in Hannover mit Hilfe von Siliziumsolarsensoren (SiS) und Thermopile-Pyranometern (Pyr) durchgeführt, um die folgenden Forschungsfragen zu untersuchen: (1) Wie genau sind die Transpositionsmodelle, welche die globale und diffuse Sonneneinstrahlung auf geneigten Ebenen abschätzen? (2) Gibt es ein alternatives Konzept zur Steigerung des Eigenverbrauchs durch Neuorientierung von PV Systeme als die nach Süden ausgerichteten Systeme und (3) wie genau sind die Silizium-Solarstrahlungssensoren und wie groß ist die Abweichung zu Thermopile-Sensoren?

Zur Beantwortung der ersten Frage, wird die Leistung von fünf bekannten und weit verbreiteten Transpositionsmodellen, welche die Global- und Diffusstrahlung auf geneigten Flächen basierend auf der globalen horizontalen Bestrahlungsstärke berechnen, verglichen. Folgende Modelle werden ausgewählt, da die erforderlichen Eingabedaten an den untersuchten Messsorten verfügbar sind und da sie die drei häufigsten Modelltypen darstellen: isotrop, anisotrop mit zwei Komponenten und anisotrop mit drei Komponenten. Die modellierten Daten der geneigten Bestrahlungsstärke werden mit Daten von verschiedenen Messwinkeln in Hannover (Deutschland) und NREL (Golden, CO, USA) verglichen. Die Ergebnisse zeigen, dass insbesondere die Annahme einer isotropen Verteilung der diffusen Himmelsstrahlung nach dem analytischen Ansatz von Liu & Jordan zu einer Unterschätzung der Ergebnisse verglichen mit den Messdaten führt. Im Vergleich zu den isotropen Modellen überschätzen die anisotropischen Modelle die Bestrahlungsstärke von nach Süden gerichteten Sensoren und den größten Teil der vertikal geneigten Bestrahlungsstärke. Die Abweichungen der anisotropen Modelle von den Messungen nehmen mit zunehmender Entfernung von der Südausrichtung zu. Es hat sich auch deutlich gezeigt, dass das grundlegende Kriterium für die Auswahl eines Transpositionsmodells zur Simulation der elektrischen Leistung eines PV-Systems seine Fähigkeit ist, die diffuse Strahlung des Himmels unter allen Wetterbedingungen zu simulieren.

Im nächsten Teil dieser Arbeit, wird die zweite Frage beantwortet, in dem die verschiedenen Ausrichtungen von PV-Anlagen in Bezug auf erzeugte Energie, Eigenverbrauch (SC) und Grad der Autarkie (AD) verglichen werden. Die gemessene Bestrahlungsstärke wird verwendet um die erzeugte PV-Energie von verschiedenen Kombinationen von Neigung und Ausrichtung zu evaluieren. Der Eigenverbrauch wird mit Hilfe von einem Satz von Lastprofilen aus Mehrfamilienhaushaltsmessungen berechnet, um die besten und wirtschaftlichsten Ausrichtungen für PV-Dachanlagen zu bewerten. Die Ergebnisse zeigen, dass südlich (S) ausgerichtete Anlagen tagsüber die höchste elektrische Leistung liefern, während Kombinationen aus Ost- und Westausrichtung (E-W) zu den höchsten Eigenverbrauchsraten führen. Dies führt dazu, dass die Kombinationen aus Südost- und Südwestausrichtung (SE-SW) den höchsten Grad an Autarkie liefern, obwohl sie die jährliche PV-Leistung um 5-6% reduzieren. Die wirtschaftliche Analyse von PV-Anlagen ohne Einspeisetarif (FIT) zeigt, dass die SE-SW- und E-W-Kombinationen die niedrigsten Stromkosten im Vergleich zur S-Ausrichtung bei gleicher Neigung aufweisen. Bei PV-Anlagen mit FIT liefert derzeit die Südausrichtung die beste Energieausbeute. Jedoch nimmt der wirtschaftliche Vorteil der S-Orientierung infolge des anhaltenden Rückgangs der FIT ständig ab. Sinkt der Einspeisetarif auf 7 Ct/kWh, so sind die E-W- und SE-SW-Orientierungen vorteilhafter für den Eigentümer. Zusätzlich wurde die Systemleistung

mit Hilfe von zwei häufig verwendeten PV-Software (PVSOL und PVsyst) simuliert. Die Vergleichsergebnisse zeigen, dass sowohl beide PV-Software den SC als auch die AD für alle untersuchten Orientierungen unterschätzen, was zu dem Schluss führt, dass Verbesserungen bei der Modellierung erforderlich sind.

Die dritte Frage beschäftigt sich mit der Genauigkeit von Siliziumsensoren (SiS), indem Messdaten auf horizontaler Ebene mit den Thermopile-Pyranometer-Daten als Referenz-Instrument verglichen werden. Es hat sich gezeigt, dass die mit dem Thermopile-Pyranometer (Pyr) gemessenen Werte höher sind, als die unkorrigierte mit dem Siliziumsensor gemessene Bestrahlungsstärke. Die monatliche Differenz liegt zwischen 3,7% im Juli und 17,1% im Januar, und die jährliche Pyr-Bestrahlungsstärke ist um 6,5% höher. Der Siliziumsensor misst jedoch während der bewölkten Tage eine höhere Bestrahlungsstärke als Pyr. Der Messfehler des Siliziumsensors wurde im Rahmen dieser Arbeit analysiert. Basierend auf den untersuchten Messfehlern und den Unterschieden der beiden Sensoren wurde ein Korrekturmodell vorgeschlagen, um diese zu minimieren. Das Ziel des Modells ist die Siliziumsensoren an die radiometrischen Messungen anzupassen, um thermopile Sensoren zu simulieren. Durch die Anwendung des Korrekturmodells auf die SiS-Messdaten werden die Unterschiede zwischen den Sensoren signifikant verringert. Der Unterschied im Tagesverlauf zwischen beiden Sensoren unter wolkenlosem Himmel lag meistens unter $\pm 2{,}0\%$. Zudem sinkt der jährliche Wert der Bestrahlung von 70 kWh/m^2 (6,5%) auf 15 kWh/m^2 (1,5%) durch die Anwendung des Korrekturmodels.

Schlüsselwörter : Einfallende Sonnenstrahlung; Transpositionsmodelle; geneigte Oberfläche, Modellierung der PV-Ausgangsleistung; Neigungswinkel; Orientierung; PV-Dachanlagen

Contents

List of Figures

List of Tables

List of Symbols

A	Area
α	Temperature coefficient
AD	Degree of Autarky
AM	Air mass
AOI	Angle of incidence
E	Irradiance
E_0	Extraterrestrial radiation and incident irradiance
E_b	Direct (beam) irradiance
E_d	Diffuse irradiance
E_{gr}	Ground-reflected irradiance
$E_{t,b}$	Beam tilted irradiance
$E_{t,d}$	Diffuse tilted irradiance
$E_{t,g}$	Global tilted irradiance
GHI	Global Horizontal Irradiance
GHI	Diffuse Horizontal Irradiance
HTW	Hochschule fuer Technik und Wirtschaft Berlin
I_{bn}	Direct-normal solar irradiance
IMuK	Institute for Meteorology and Climatology
λ	Wavelength
NREL	National Renewable Energy Laboratory
Ω	Solid angle
PV	Photovoltaic
Pyr	Thermopile Pyranometer
Q	Radiant energy
SC	Self Consumption
SiS	Silicon Sensor
SMM	spectral mismatch factor
STC	Standard Test Conditions
t	time
θ	Solar Zenith angle (SZA)
T sen	Sensor Temperature

1 Introduction

1.1 Background

The sun is a sphere consisting of intensively hot ionized gaseous matter, called plasma. In fact, the sun is a large nuclear reactor where thermo-nuclear fusion reactions take place continuously, generating huge amounts of energy [1]. The mean distance between the sun and the earth is 1.4961x 10^{11} m and is known as the astronomical unit-AU [2]. The sun represents the most important source of energy for our life. Other sources are: the geothermal heat flux generated by the earth's interior, natural terrestrial radioactivity, and cosmic radiation, which are all negligible relative to solar radiation [3]. The energy distribution of electromagnetic radiation over different wavelengths is called spectrum. Solar spectrum consists of a continuum with numerous dark absorption lines superposed (Fraunhofer lines) [4]. The solar electromagnetic spectrum is divided into different spectral ranges. The visible (400 - 700 nm) and infrared (700 - 1 x 10^6 nm) bands contain 40% and 44% of the energy, respectively, while the ultraviolet bands (100 - 400 nm) contain only 6% of the total energy. The peak radiation wavelength is approximately 480 nm [5]. The solar spectrum is a key input in radiative transfer and balance in the various layers of the atmosphere of Earth and other planets [4]. The amount of solar radiation that reaches the outside of the earth's atmosphere is called extraterrestrial radiation. The intensity of this radiation depends on the radiant output of the sun, the distance of the earth from the sun, and the latitude at which the radiation is being measured [6]. The integral of the extraterrestrial solar spectrum (Figure 1.1) equates to the integral of a blackbody spectrum at 5772 K (Planck's law). The solar radiation received at a given geographical site varies in time: between day and night due to the earth's rotation and between seasons because of the earth orbit.
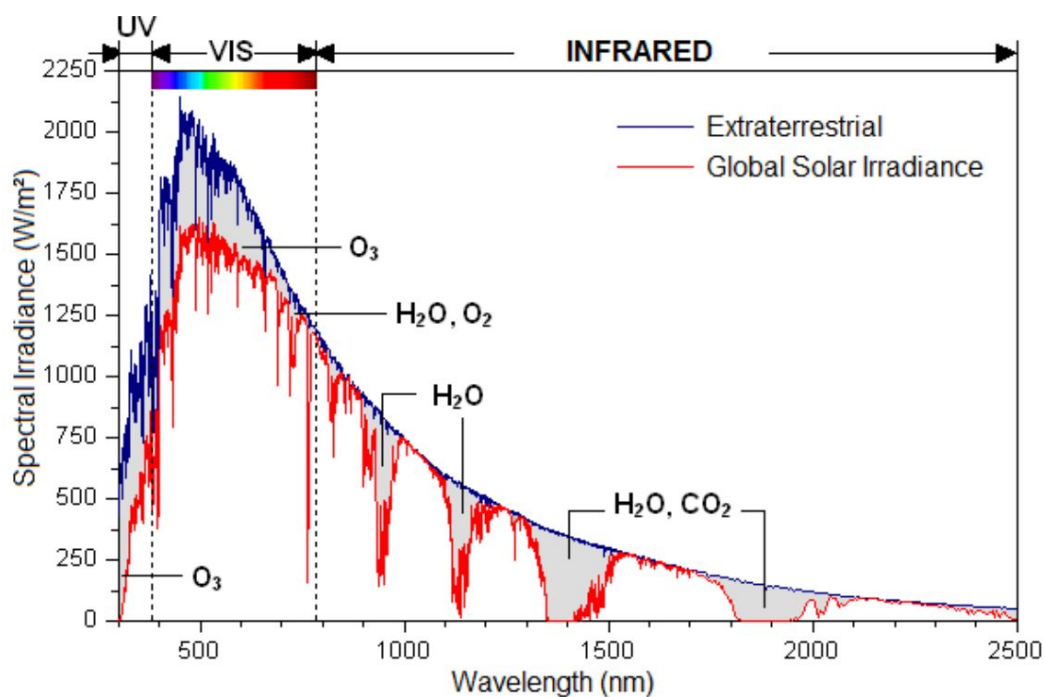

Figure 1.1: Standard solar spectrum that is provided by he American Society for Testing and Materials-ASTM [7], (data from [8]).

At a given time, it also varies in space, because of the changes in the obliquity of the solar rays with longitude and latitude [3]. The atmosphere of the earth absorbs and scatters large parts of the incoming solar radiation dependent on wavelength. Due to the absorption of certain wavelengths by atmospheric constituents such as water vapor, dust particles, ozone, and other molecules in the air, the spectrum that is received by the earth's surface is significantly altered [9]. For instance, there is nearly a complete extinction of solar ultraviolet radiation below 300 nm (Figure 1.1) because of ozone and molecular oxygen absorption in the middle atmosphere [10]. Solar radiation can be divided into shortwave (280-2800 nm) and long-wave (2800-100 000 nm) components. Over 85% of the radiation that comes directly from the sun is shortwave radiation. Shortwave radiation is the energy source that drives evaporation, transpiration, photosynthesis, and many other important processes [11]. In the absence of clouds, a major fraction of incoming shortwave solar radiation reaches the surface, and part of it is reflected back into outer space. Solar radiation provides the energy for many processes on Earth including processes that sustain living systems and circulation of the atmosphere and oceans [12]. This energy is also readily available to provide electricity and heat for both industrial and domestic applications.

1.2 Solar Irradiance on Inclined Surfaces

Solar irradiance E_λ is the amount of solar energy dQ that reaches the surface of a receiver with a square meter in a second [13].

$$E_\lambda = \frac{dQ}{dA \cdot dt \cdot d\lambda} \left[\frac{W}{m^2\,nm} \right]. \tag{1.1}$$

where, dA is the area, dt the time interval, and $d\lambda$ the wavelength interval. The SI units of irradiance are watts per square meter (W/m^2). In the literature and in some articles, on which this thesis is based, the symbol I is also used for solar irradiance instead of E. The solar irradiance that is measured on a horizontal surface is defined as the Global Horizontal Irradiance (GHI). For photovoltaic and thermal solar systems, solar radiation is collected generally on non-horizontal (inclined) surfaces in order to maximize the use of solar energy. The solar irradiance incident on a collector is strongly affected by the collector's orientation [14], [15], which has two main features: Azimuth direction (N, S, SE, etc.) and the tilt angle from the ground (β). The irradiance will always be at its maximum when the collector surface is perpendicular to the incoming solar radiation. However, as the angle between the sun and a fixed surface is continually changing, the irradiance measured on a fixed surface is less than that of the incident irradiance (Figure 1.2). On the other hand, using a tracking system over the life of a system (about 20 years for PV systems) is too expensive. Therefore, finding the optimum tilt angle to receive maximum solar radiation on a thermal collector or a photovoltaic module is the cheapest and most effective method [16]. Irradiance components that compose the total amount of solar irradiance on tilt surface (Global Tilted Irradiance-GTI) are the beam, the diffuse, and the ground-reflected irradiance.

Irradiance components change differently with changing the orientation of the collector, so irradiance components, should be separately studied to understand the effect of a collector's orientation on the irradiance measured on it. In the following section, we highlight the effect of irradiance components and how they change according to collector's orientation.

1.2.1 Beam Irradiance

The beam irradiance E_b is the solar radiation transmitted directly from the sun down to the receiving surface on a straight-line path. The beam irradiance is the key resource for any concentrating solar system, and it has a significantly higher variability in space and time. Beam solar radiation is measured usually by means of pyrheliometers, the receiving surfaces of which are arranged to be normal
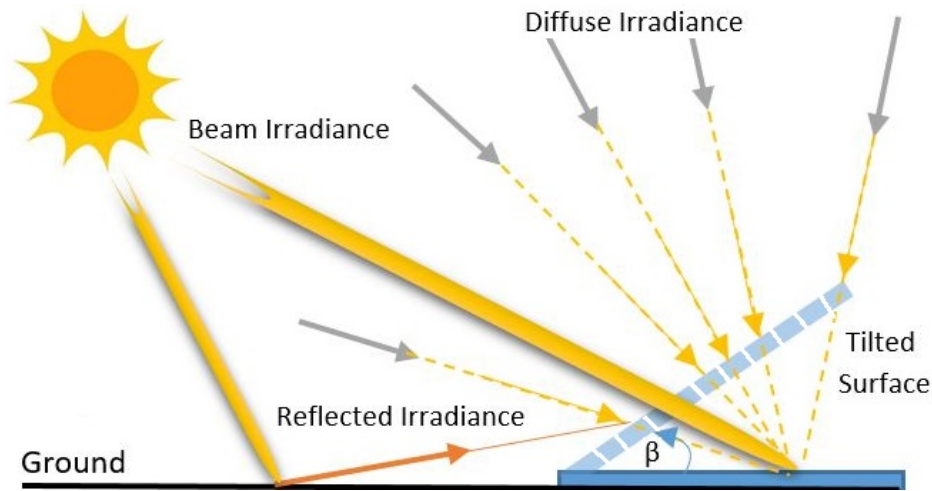
Figure 1.2: Composition of the global solar radiation on a tilted surface.

to the solar direction. Measurement of beam irradiance requires higher accuracy and attention; therefore, it's uncertainty is higher [17]. The beam irradiance measured on a tilted surface (Beam tilted Irradiance-$E_{t,b}$) depends strongly on the orientation of the collected surface. It can be expressed by multiplying the direct-normal solar irradiance I_{bn} by a geometrical orientation factor. This can be denoted by:

$$E_{t,b} = E_{bn}.\cos(i). \tag{1.2}$$

where: $E_{t,b}$ is the tilted beam irradiance; E_{bn} the direct-normal solar irradiance; and $\cos(i)$ is a geometrical factor; the angle of incidence with the normal to the surface.

1.2.2 Diffuse Irradiance

The diffuse solar irradiance E_d is the result of the interaction of the solar radiation and the atmosphere. The diffuse irradiance received for a particular geophysical location on Earth's surface depends mainly on the solar elevation, turbidity in the atmosphere, and cloudiness. The variability in the amount and type of cloud has a dominant role on the value of diffuse radiation [18]. The phenomena of scattered radiation in the atmosphere are very complex and varied, and it is not uniform throughout the sky dome [19]. Diffuse irradiance on a tilted surface (Diffuse tilted irradiance-$E_{t,d}$) depends on the view factor of the receiving surface to the sky and the sky irradiance distribution. Therefore, the orientation of the receiving surface is an essential factor in determining the diffuse irradiance that reaches the surface.

1.2.3 Ground-reflected Irradiance

Ground-reflected irradiance E_{gr} is the part of the solar radiation that is first reflected on the ground and then reaches the receiving surface. It depends on ground albedo and the view factor of the collector to the ground. The distribution of the ground reflected radiation is normally assumed to be isotropic [20].

1.2.4 Global Tilted Irradiance

The global tilted irradiance $E_{t,g}$ is the total amount of shortwave radiation that falls on a tilted surface, and it is computed as the sum of all three components: the beam, the diffuse, and the global tilted

irradiances.

$$E_{t,g} = E_{t,b} + E_{t,d} + E_{gr} \tag{1.3}$$

1.3 Atmospheric Effects on Solar Irradiance

Solar radiation passing through the atmosphere undergoes changes, which make it heterogeneous and intermittently distributed [21]. According to the earth energy budget [22], 22% (76 W m^2) of the extraterrestrial radiation is reflected back to space, 23 % (79 W m^2) is absorbed by the atmospheric components (clouds, gases, aerosols), and only 54 % (185 W m^2) of the radiation reaches the earth's surface (Figure 1.3).
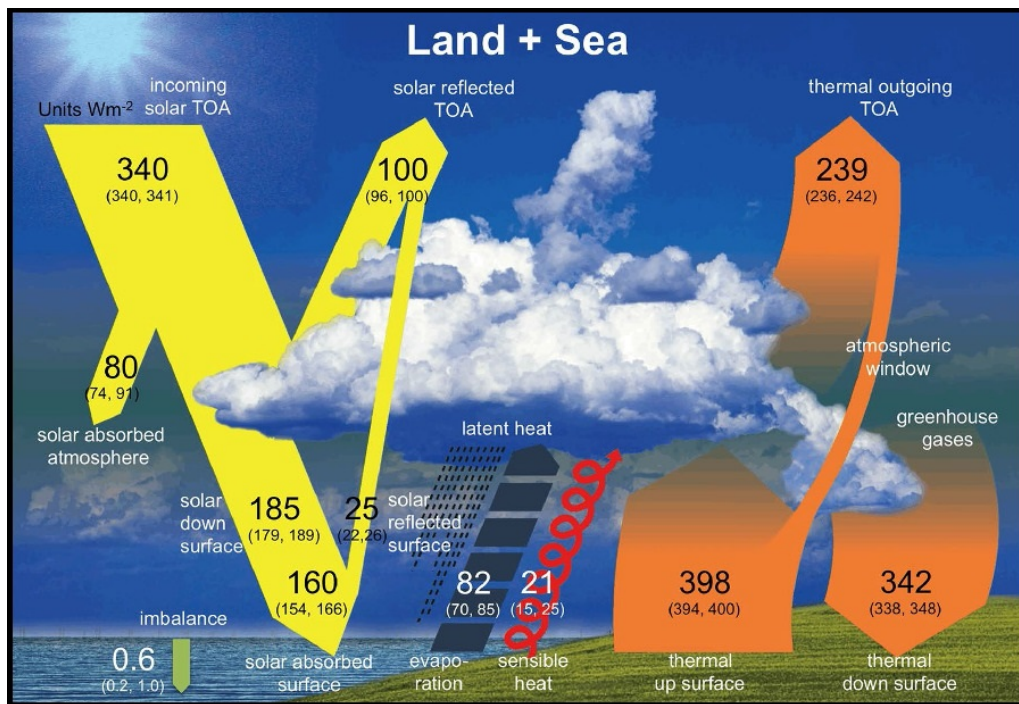
Figure 1.3: Schematic diagram of the global mean energy balance of the earth. Numbers indicate best estimates for the magnitudes of the globally averaged energy balance components together with their uncertainty ranges, representing present day climate conditions at the beginning of the twenty first century [22].

The solar irradiance measured on the earth's surface depends on many factors that affect their temporal and spatial variation. These factors include the geographical, astronomical, physical, and meteorological factors. The astronomical factors are related to the solar constant, solar declination, hour angle, and duration of sunshine. The latitude, longitude and altitude of the site belong to the geographic factor. The physical factors are related to the content of water vapor in the atmosphere, the scattering by air molecules and miscible gases, the presence of aerosols, and the effect of ozone [23], [24]. Meteorological factors are related to the temperature, precipitation, humidity, and the other meteorological parameters [25]. We will focus in this section on the latter two factors, which represent the interaction of the atmosphere and the solar radiation. When solar radiation enters the atmosphere, it is absorbed and scattered by atmospheric constituents, such as air molecules, aerosols, water vapor, liquid water droplets, and clouds [26]. Scattering occurs when the radiation interacts with air molecules, water vapor, and dust particles in the atmosphere and part of the incident energy is distributed in space in the form of photons, which continue travelling in all directions. The

degree of scattering is determined by the wavelength of the radiation in relation to particle size, the concentration of particles in the atmosphere, and the total mass of air through which the radiation has to travel [27]. The absorption of solar radiation is a process that occurs due to the presence of different components in the atmosphere and varies with the wavelength [28]. In the process of absorption, the solar radiation is converted to heat, which is emitted by the particles as long-wave radiation. Through scattering and absorption processes, the atmosphere controls the amount of incoming shortwave solar radiation that reaches the ground and the amount of solar radiation that reflects back into space. The atmospheric extinction of the beam solar irradiance can be described by the famous Beer-Bouguer Lambert law:

$$E(\lambda) = E_0(\lambda)exp(-\tau(\lambda)AM(\theta)) \qquad (1.4)$$

where E(λ) is the beam irradiance at wavelength λ on the ground, $E_0(\lambda)$ is the extraterrestrial solar irradiance, $\tau(\lambda)$ is the total optical thickness, and AM(θ) is the optical air mass at zenith angle (θ).

In the following, we will give a short overview of the main factors influencing the solar irradiance on its way through the atmosphere and how they affect it.

1.3.1 Effects of Atmospheric Gases

Atmospheric gases can contribute to the attenuation of incoming solar radiation through scattering and absorption. The scattering of solar radiation by air molecules can be described by the theory of Rayleigh. Rayleigh scattering theory was based on the assumption that the amount of scattering is inversely proportional to the fourth power of the wavelength (λ^{-4}), when the sizes of particles are much smaller than the wavelength of the incident radiation (diameter $< 0.2\lambda$) [29]. Since blue light is the shortest visible wavelength, the sky appears blue on a clear-sky days as a result of Rayleigh scattering. Rayleigh scattering effects are well understood, although there is still disagreement over the depolarization factor that should be used [30]. Atmospheric gases also absorb solar radiation in selected wavelength bands, leading to a qualitative modification of the terrestrial spectrum with typical absorption bands, as shown in figure 1.1. The UV radiation in the wavelength interval between 200 and 300 nm is mainly absorbed by Ozone O_3 in the stratosphere. In the troposphere, the absorption of solar radiation occurs in the visible and near-infrared regions, owing primarily to H_2O, CO_2, O_2, and O_3 [28].

1.3.2 Effects of Aerosols

Aerosols are suspensions of particles in air, liquids, or solids, excluding clouds and precipitation, within a size range from 0.001 to above 100 μm [31]. Atmospheric aerosols contain a mixture of organic and inorganic components. The aerosols may be classified according to their origin into marine, continental, rural, remote, background, and urban aerosols, where each category has different characteristics, size distribution, and shapes [32]. Concentrations and compositions of aerosols vary significantly with location and time. Atmospheric aerosols scatter and absorb solar radiation leading to variable effects on Earth's radiative balance [33]. Depending on their optical properties, aerosols reduce the direct solar radiation component and modify the direction of the diffuse component, compared to aerosol-free atmospheric conditions. The Angstrom turbidity formula [34] is used in general for characterization of the attenuation effects of scattering and absorption by atmospheric aerosols. According to this formula, the aerosol optical depth (AOD) can be expressed over a limited wavelength range by:

$$\tau_a(\lambda) = \beta\lambda^{-\alpha} \qquad (1.5)$$

where $\tau_a(\lambda)$ is the AOD in the vertical direction, β is the extinction coefficient that relates to the concentration of aerosols in the atmosphere, and α is the wavelength exponent which is closely

correlated to the size distribution of the scattering particles. In the visible range, aerosols affect atmospheric radiation balance through direct, semi-direct, and indirect effects. In the direct effect, aerosols scatter and absorb the incoming solar radiation; scattering by aerosols can be described by Mie theory [35]. They affect the atmosphere as semi-direct effect by heating it through absorption of incoming solar radiation. Moreover, aerosols can also modify solar radiation indirectly through their role in cloud condensation and as ice nuclei, an effect known as aerosol indirect radiative forcing [36],[33]. Aerosols that consist mostly of inorganic matter (such as sea salt, sulfate, and nitrate) tend to be scattering, affecting climate through the direct effect [37]. On the other hand, aerosols that consist of elemental carbon, mineral dust, and certain moderately absorbing organics tend to be absorbing, affecting climate through the direct and semi-direct effects [38].

1.3.3 Effects of Clouds

Clouds cover about 60% of the earth's surface, and they are the most important atmospheric phenomena influencing the spatial and temporal distribution of solar radiation [39]. Clouds reflect the incoming solar radiation back to space (cloud albedo effect), causing the cooling of the Earth-atmosphere system, which occurs primarily at the surface [40]. The amount of reflected radiance is significantly influenced by cloud optical thickness, which can be deduced from cloud liquid water content (LWC) and cloud droplet effective radius [41]. Another important role of the clouds is the protection of Earth's surface against cooling at night (greenhouse effect). This is due the fact that the maximum of the terrestrial emission is in the far infrared, where water droplets are highly absorbing. Therefore, any change of cloud optical properties can disturb the energy balance of the earth-atmosphere system. According to Turner et al. [40], the net longwave radiation at the surface increases with increasing the liquid water path (LWP), while the downward shortwave radiation decreases with increasing LWP. The reflection of solar radiation and the greenhouse effect of terrestrial radiation depends on several cloud parameters: droplet size distribution, cloud density, thickness, altitude, and temperature profile [42]. Clouds influence the solar shortwave radiation by reflection, scattering, and to a lesser extent, by absorption. Clouds are made up of liquid and solid particles that are generally much larger than the wavelengths of incident solar radiation. Therefore, wavelength-independent Mie scattering dominates the scattering process. According to Kokhanovsky et al. [43], the microphysical properties of water or ice clouds (droplet size, ice crystal shape, and distribution), the spectral reflection, absorption, and scattering rates depend strongly on the angle of incidence of the solar irradiance .

1.3.4 Effects of Air Mass

The optical path length through the atmosphere is described by the air mass (AM). In general, air mass actually refers to relative air mass that is measured relative to the path length when the sun is directly overhead (SZA = 0°). For example, at AM2.0, the path length through the atmosphere is two times longer than if the sun were directly overhead. The value AM1.5 is often used as a standard for testing solar cells (Standard Test Conditions-STC), while irradiance at AM0 is the extraterrestrial irradiance. The AM value is location, date, and time dependent.

Figure 1.4 shows three global solar spectra on the earth's surface that are calculated by the radiative transfer model UVSPEC in the Libradtran package [44] at three different air mass ratios (AM1.5, AM2.0, AM4.0) after having interactions with the atmosphere. As air mass increases, the direct beam traverses longer path lengths in the atmosphere, which results in more scattering and absorption of the direct beam and a lower percentage of beam-to-global ratio (for the same atmospheric conditions). The air mass is often approximated for a constant density atmosphere and ignoring Earth's curvature using the geometry of a parallel plate:
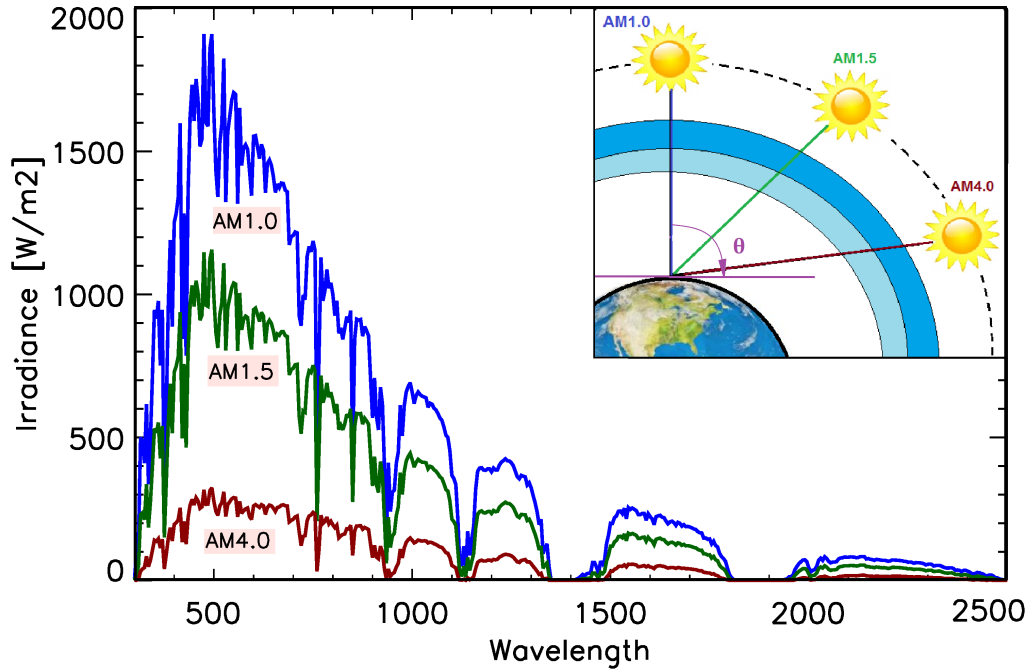
Figure 1.4: Clear-sky spectral irradiance at three different AM values (AM1.0, AM1.5, AM4.0) calculated by UVSPEC and illustration of AM. AM1 refers to atmosphere at solar zenith, AM1.5, where the radiation is incident at a SZA of 48.2°, and AM4.0 refers to atmosphere near the horizon at SZA of 75.5°.

$$AM = \frac{1}{cos(\theta)} \tag{1.6}$$

where θ is the solar zenith angle.

This simple approach is adequate for zenith angles as large as 80°, but at larger zenith angles and especially near the horizon, the accuracy degrades rapidly because AM goes to infinity at 90°. There are many formulas developed to fit the tabular values of air mass. In this work, we used the formula developed by Kasten and Young [45], which gives reasonable results for zenith angles of up to 90°, with an air mass of approximately 38 at the horizon (Eq.1.7) .

$$AM = \frac{1}{cos\theta + 0.50572(96.07995 - \theta)^{-1.6354}} \tag{1.7}$$

1.4 Utilization of Solar Radiation on a Solar Photovoltaic

Solar power has the potential to be the most important energy source in the world. A typical argument that exhibits the potential of solar power is that the energy offered freely to us by the sun in one hour is comparable to the global consumption in one year [46]. Photovoltaic (PV) is one of the technologies that make use of the sun's great energy resource. The most common method of solar energy conversion into electricity is based on the use of solar cells, as it has shown promise in producing devices with a stable performance and high-efficiency [47].

7

1.4.1 Solar Cell

The solar cell or photovoltaic cell is an electronic device that converts solar radiation into electrical energy. The photovoltaic cell working principle is based on the photovoltaic effect. This effect is closely related to the photoelectric effect, where the emission of electrons from a material is due to light (photon) absorption with a frequency above a material-dependent threshold frequency. A solar cell consists of n-type (having electrons as a majority charge carrier) and p-type (having holes as a majority charge carrier) semiconductor materials, an electrical pn-junction, and electrical terminals to conduct electric current. When solar radiation falls on the cell, the photons are absorbed in the semiconductor, and negatively charged electrons and positively charged holes are created, while the electrical junction separates these electrons and holes from one another. The structure of a solar cell can be well understood from Figure 1.5. If a wire is connected from the cathode (n-type material) to the anode (p-type material), electrons flow through the wire.
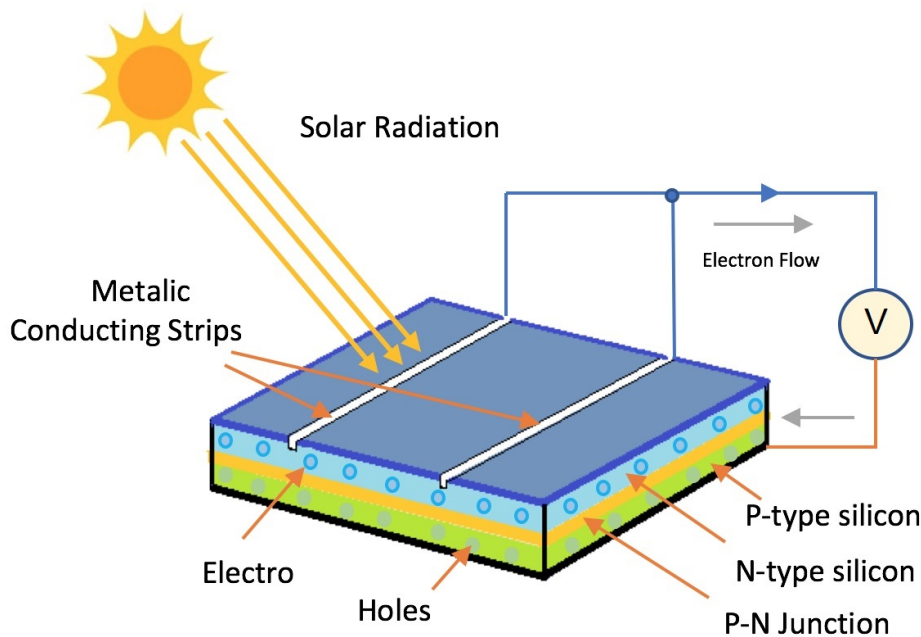
Figure 1.5: Cross section of solar cell [48].

Thus, the solar cell has two major operations: generation of a photo-generated charge carrier (holes and electrons) in the absorption layer (p-n junction) and the separation and collection of these charge carriers at their respective metal contacts. Both sides of solar cells have conductive surfaces referred to as the rear metal contact and the front metal contact.

There are various semiconductor materials usable in PV cells, and silicon is the most common. Silicon has several advantages, such as abundance on Earth, low contamination rate, high durability, and the wide experience of the microelectronics industry [49]. There are two major types of the silicon cells, monocrystalline and polycrystalline, although many other technologies have been developed. The two types share the same theoretical background, but there are some variations. Solar panels, which are made up of many solar cells, are nonlinear energy sources, and the operation points of the system also change along with the change in weather conditions [50]. Thus, the current/voltage values, power outputs, and efficiency of photovoltaic devices depend on weather parameters [51], [52].

1.4.2 Spectral Response

Spectral response (SR) is one of the most important parameters in PV device characterization. The spectral response of a solar cell is defined as the ratio between the short circuit spectral current density $J_{sc\lambda}$ and the spectral irradiance E_λ [53]. SR can be written as:

$$SR = \frac{J_{sc\lambda}}{E_\lambda} \tag{1.8}$$

where the units are A/W. The spectral response provides information on the physics at play in the device, taking into account not only the material but also the reflectance and transmittance of the device [54].
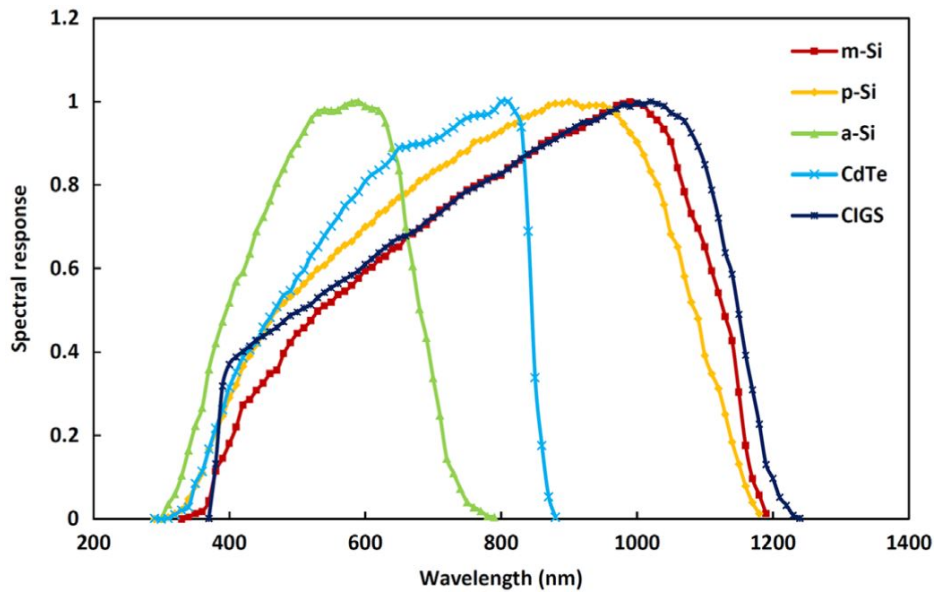
Figure 1.6: Normalized spectral response of different single-junction PV technologies. Data obtained from [55].

The spectral response of a PV device is determined traditionally by illuminating the device with a series of monochromatic beams at different wavelengths and measuring the short-circuit current generated under each wavelength [56]. Figure 1.6 shows the spectral response of different PV technologies. It can be seen that the solar cells do not respond to the spectrum equally, and the spectral response of copper indium gallium selenide (CiGS), mono-crystalline (m-Si), and poly-crystalline (P-si) silicon cells covers a larger area of the spectrum than an amorphous silicon (a-Si) or Cadmium telluride (CdTe) cell. These PV technologies have been selected because they cover virtually all the photovoltaic market share. The influence of spectral variations of incident solar radiation on the PV performance depends on the spectral response of each photovoltaic cell technology [57]. The spectral matching between incident solar radiation and the spectral response of a PV material can lead to higher PV efficiency and longer PV lifetimes due to the reduction of thermalization heating losses [58].

2 Instruments and Methods

This chapter provides a brief description of the measurement system used in this work. This includes a detailed description of the sensors used for collecting the irradiance data, the mean features and differences between the sensors, and the methods used to improve the quality of the data .

2.1 Measurement System

The measurement system was installed in January 2014 on the roof of the Institute for Meteorology and Climatology (IMuK) of the Leibniz Universität Hannover (Hannover, Germany; 52.23° N, 09.42° E and 50 m above sea level). The measurement system is a part of the meteorological measuring system of the IMuK, which consists of different meteorological and radiation instruments (Figure 2.1). However, we will focus here only on the irradiance sensors, as their data will be used in this thesis, namely thermopile pyranometers and silicon-based sensors. The sensors were described shortly in [59], [60], [61]. In the following section, we introduce them with more details.

Figure 2.1: Set of silicon-based solar sensors mounted at different tilt angles and orientations, and a thermopile pyranometer available and operational at IMuK.

2.1.1 Thermopile Pyranometers

Thermopile pyranometers are broadband instruments that measure global solar irradiance received from the whole skydome (2Ω solid angle). They are widely used and represent the workhorse of solar irradiance measurements for climatological research and weather monitoring purposes due to their nearly constant spectral sensitivity for the whole solar spectral range. However, the time response of thermopile sensors is typically in the order of 1-10 s [62]. This long response time makes them unable to follow rapid changes of solar radiation associated with clear/cloudy transitions during partly cloudy conditions. Consequently, significant measurement errors may occur. The International Standard and the World Meteorological Organization (WMO) distinguish three classes of pyranometers: the best is called secondary standard, the second best is called first class, and the third one is second-class (Table 2.1).

A typical pyranometer is schematically represented in Figure 2.2. It consists of a black painted disk (detector) sealed by two glass domes, which protects the sensor from thermal convection and weather threat (rain, wind, and dust). The double glass domes also limit the spectral sensitivity of the instrument in the wavelength range of 280 - 2800 nm and usually have a bubble for leveling. Moreover, the specially designed double glass domes also produce a more accurate cosine response in the sensor and reduce thermal losses [63]. Passive thermopile pyranometers, such as the ones used, do not require a power supply. The detector generates a small voltage in proportion to the temperature difference between the black absorbing surface and the instrument housing. This is of the order of 10 μV (microvolts) per W/m^2, so on a sunny day, the output will be around 10 mV (millivolts) [64].
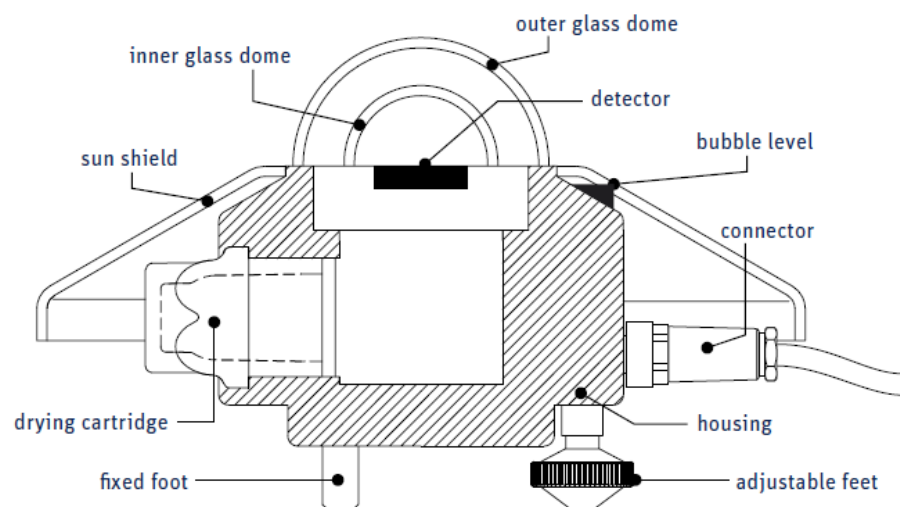
Figure 2.2: Schematic of thermopile pyranometer (Kipp & Zonen models CMP6, CMP11, CMP21 and CMP22) [65].

Pyranometer Working Principle

Thermopile pyranometers are based on the thermoelectric detection principle. The incoming radiation is almost completely absorbed by a horizontal blackened surface over a very wide wavelength range [64]. The resulting increase of temperature is measured via thermocouples connected in series or series-parallel to make a thermopile. The hot junctions are located beneath the blackened receiver surface and are heated by the radiation absorbed in the black coating. This design allows for excellent spectral absorption and long-term stability characteristics. The cold junctions of the thermopile are in thermal contact with the pyranometer housing, which serves as a heat-sink. When solar radiation passes through the dome and falls on the sensing element of the pyranometer, a temperature difference is created between the two junctions of the thermopile and hence an electromagnetic field

Table 2.1: Accepted categorizations of pyranometer accuracy defined by ISO 9060: 2018 and WMO Guide 8th edition.

ISO Specification (ISO) WMO Characteristics (WMO)	Class A (Secondary standard)	Class B (First class)	Class C (second class)
Quality	high	Good	Moderate
Response time (to 95% of final value) ISO WMO	< 10s < 15s	< 20s < 30s	< 30s < 60s
Zero offset response A: response to 200 W/m^2 net thermal radiation ISO&WMO B: response to 5 K/h change in ambient temperature ISO&WMO C: total, including zero offset A, B, and other sources ISO	±7 W/m^2 ±2 W/m^2 ±10Wm^2	±15 W/m^2 ±4 W/m^2 ±21Wm^2	±30 W/m^2 ±8 W/m^2 ±41Wm^2
Resolution (smallest detectable change) WMO	1 W/m^2	5 W/m^2	10 W/m^2
Non-stability (change in sensitivity per year) ISO&WMO	±0.8 %	±1.5 %	±3.0 %
Non-linearity (percentage deviation from the sensitivity at 500 W/m^2 due to the change in irradiance within 100 W/m^2 to 1000 W/m^2) ISO&WMO	±0.5 %	±1.0 %	±3.0 %
Directional response for beam radiation (errors caused by assuming that the normal incidence responsivity at 1000 W/m^2 is valid for all directions) ISO&WMO	±10 W/m^2	±20 Wm/^{2}	±30 W/m^2
Spectral error ISO	±0.5 %	±1.0 %	±5.0%
Temperature response percentage deviation due to change in ambient temperature within the interval from 10C to 40C relative to 20C ISO 50C Interval WMO	±1 % 2 %	±2 % 4 %	±4 % 8 %
Tilt response (deviation from the responsivity at 0° tilt (horizontal) due to change in tilt from 0 to 180 at 1000 W/m^2 irradiance) ISO&WMO	±0.5 %	±2.0 %	±5.0 %
Additional signal processing errors WMO hourly totals WMO daily totals	3 % 2 %	8 % 5 %	20 % 10 %

(EMF) is developed. The thermo-EMF is recorded by the data logger and finally converted into the output in W/m^2 as the irradiance.

In most models, a white plastic cover (sun shield) protects the metal body from heating up and reduces reflection. Additionally, they contain a cartridge of silica gel inside the dome that absorbs water vapor.

Besides global irradiance, pyranometers can be also used to measure diffuse irradiance. For this, a small shading disk (or ball) can be mounted on an automated solar tracker to ensure that the pyranometer is continuously shaded. Alternatively, a shadow ring (also known as a shadow band) may prevent the direct component from reaching the sensor, so that the shaded pyranometer measures diffuse radiation only.

Traditionally, pyranometers were mainly used for climatological research and weather monitoring purposes. However, recent worldwide interest in solar energy has also led to an increased interest in pyranometers.

The thermopile sensors used in this work are CMP11 pyranometers from Kipp & Zonen [65] and are classified as class A specification sensors with the ISO 9060 standard (referred to simply as Pyr). The sensors were used to measure Global Horizontal Irradiance (GHI) and Diffuse Horizontal Irradiance (DHI). Although thermopile pyranometers have nearly constant spectral sensitivity for the whole solar spectral range and provide reproducible measurements of solar irradiance, the cost of these sensors is high. A field station equipped to measure only the global and diffuse horizontal irradiance will typically use two thermopile sensors. These two instruments and the associated data acquisition will cost several thousand euros. If we consider tilted irradiance measurements and the maintenance costs associated with such facilities, it can be an appreciable fraction of capital investment, limiting the ability of the solar research community to monitor climate change and obtain the data needed for the resource assessment.

2.1.2 Silicon Sensors

During the past decades, silicon-based sensors have been used as low-cost radiation instruments to monitor PV solar plants. These sensors have time responses of about 10 μs, enabling the sensors to measure rapid solar radiation variation when clouds move in front of the sun [66], [67],[62]. Silicon sensors have a similar spectral response as a PV panel. As a result, silicon-based sensors provide a more accurate representation of the energy available for conversion to electricity by a solar PV panel.

Silicon Sensor Working Principle

Silicon-based sensors work in a very different way than thermopile pyranometers; their Working Principle is based on the photovoltaic effect. Photons with energy above the bandgap of the PV material are converted directly into positive and negative charges that can be collected and used in an external circuit. They generate a current that is dependent on the number and spectral distribution of the incident photons [68]. Typically, the current of the sensor is measured by measuring the voltage across a small resistor (shunt) that is included in the sensor package. This voltage is calibrated under the STC. In general, there exist two main types of silicon sensors, namely silicon-photodiode pyranometers and reference solar cells. Photodiode pyranometers were developed as a low-cost alternative to thermopile-based pyranometers to provide integrated solar resource information for climatological researches [66]. The photodiode-based pyranometer is based on measuring the short circuit current (I_{sc}) of a solar cell under a diffusing lens (Figure 2.3, left). The pyranometer body and diffuser are designed to minimize deviations from a true angular response [69]. They also contain some internal circuitry that helps minimize the effect of temperature on the pyranometer's performance. However, the irradiance values indicated by these pyranometers, without correction, may differ from the (true) broadband solar irradiance.

Unlike photodiode-based pyranometers, reference solar cells do not contain a diffuser; they have glazing that affects the transmission of light, like PV modules (Figure 2.3, right). Reference solar
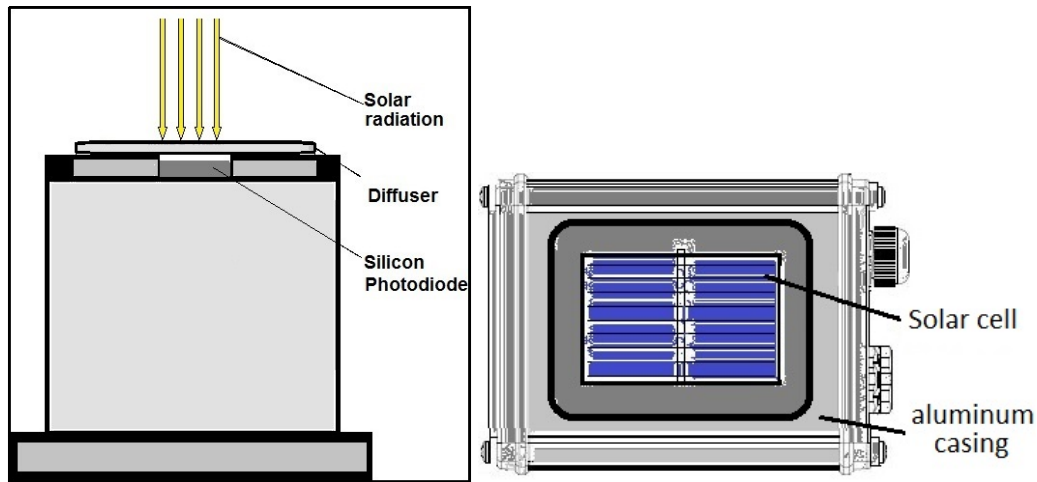
Figure 2.3: Schematic depiction of a photodiode-based Pyranometer (left) and a reference solar cells (right)

cells utilize single crystalline silicon cells, and they are used in the field to evaluate the performance of PV systems that utilize the same technology. The reference solar cells are expected to have a similar spectral response as the photodiode-based pyranometers since photodiodes and reference solar cells are both solar cells for which the output is monitored in a short circuit configuration [69]. The silicon sensors used in this work are reference solar cells from Ingenieurbüro Mencke and Tegtmeyer [70], Model Si-mV-85-PT100-4L-E (referred to simply as SiS). The sensors are build-out of a monocrystalline silicon solar cell connected to a shunt and embedded in Ethylene-vinyl acetate (EVA) between glass and Tedlar. Due to the low resistance of the shunt, the cell operates next to short-circuit [70]. The laminated cell is integrated into a case of powder-coated aluminum and the electrical connection is realized by a waterproof connector. Therefore, the sensor construction is comparable to that of a standard PV module. The sensors offer an economical and reliable solution for measuring solar irradiance levels, particularly for monitoring photovoltaic systems [70]. In addition, a SiS can measure the temperature of the solar cell using a temperature sensor laminated to the back of the cell. The IMuK measurement system includes eighteen silicon sensors at different orientations according to table 2.2. All sensors were factory calibrated in October 2013 and have traceable calibration certificates. Manufacturer specifications indicate that it should agree to within 5% of a pyranometer reading within an ambient temperature range of -20 to 70°C and normally incident irradiance.

Table 2.2: Silicon-based sensors and their orientations at IMuK measurement system.

Direction	S	E	W	SE	SW	N
Tilt angle	0°, 10°, 20°, 30°, 40°, 50°, 60°, 70°, 90°	45°, 90°	45°, 90°	45°, 90°	45°, 90°	90°
Nr. of Cells	9	2	2	2	2	1

The system was installed in January 2014 and one-minute data from all of the sensors were continuously collected, covering wide ranges of atmospheric conditions. Only cases at a solar zenith angle of less than 85° are used in this thesis. There were lost values in some periods during the year. Instead of these missing data, new values were written according to the previous and next measured values. The sensors are cleaned regularly to prevent the accumulation of dirt and dust. The data was collected continuously by the sensors and stored in data loggers. The loggers record the irradiance

and temperature data from the sensors centrally every 1 min and transfer them to a PC. Figure 2.4 shows a block diagram of measurements.
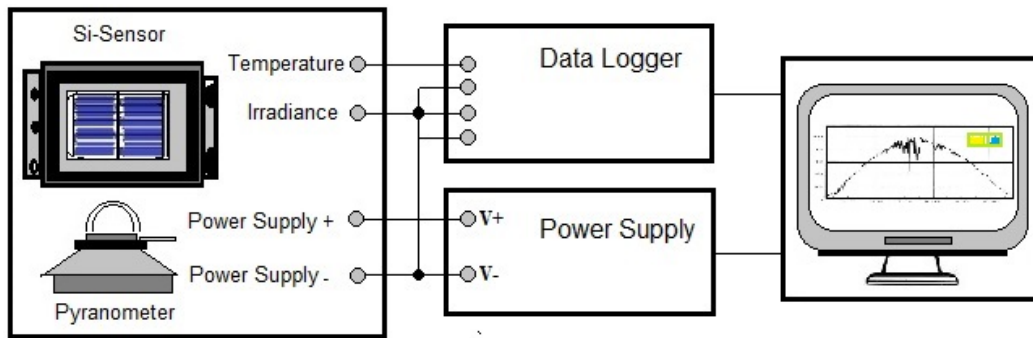

Figure 2.4: Block diagram of measurements of solar irradiance and sensor's temperature at IMuK.

2.2 Irradiance Data and Correction Procedures

Solar radiation reaches the surface is a variable source of energy. This is due to variation in the angle of incidence between the sun and the collector, the sky conditions, the spectral distribution, and many other factors. Both thermopile pyranometers and silicon sensors do not react equally to these factors, and the measured data of both sensors may contain errors that affect the accuracy of the measured irradiance (Table 2.3). The main differences between the sensors were discussed in [61].

Table 2.3: Analysis of the differences between sensors according to the manufacturers [64], [70]

Specifications	CMP11	Si-mV-85
Spectral sensitivity range (nm)	285-2800	360-1200
Response time (s)	< 5	< 0.001
Offset (W/m^2)	< 2	0
Temperature dependence (-20 - 40° C) (%)	< 1	0.2
Uncertainty (W/m2)	< 5	± 5
Non-linearity (100 to 1000 W/m^2) (%)	< 0.2	± 0.1
Cosine response (% up to 80° SZA)	< 1	< 30

Within this thesis, the measured data were used for different purposes, and a lot of quality control procedures and correction methods were applied in order to improve the quality of measurements. In the following, we will present the correction methods applied on the data of both sensors:

- Only GHI and DHI values recorded at solar zenith angles less 85° were used.

- All irradiance values less than 0 W/m^2 were removed from the analysis, since these values were likely erroneous measurements.

- Any DHI measurement that exceeded the concurrent GHI measurement was set equal to the GHI measurement because it is not physically possible for DHI to exceed GHI [71].

Moreover, the following corrections were applied to IMuK data for improving the measurement uncertainties:

2.2.1 Zero-Offset Correction

The zero-offset correction is the first correction that was applied to the data of both sensors and the only correction applied to the thermopile pyranometer data. Zero offsets in sensor signals are values that persist even if the solar irradiance is zero. The offset is negligible compared to the solar irradiance during most of the day. However, under low irradiance conditions, the zero offsets can become important. Zero offsets in solar irradiance sensors can have several origins. Most of them can be returned to thermal gradients, i.e., temperature differences inside the instrument. In the case of thermopile sensors, the thermal offset usually results from the infrared exchange between the radiometer and the sky (zero offset A) and the difference between the sensor and dome temperatures (zero offset B) [64]. The latter causes radiation cooling, which leads to the negative voltage signal from the thermopile [72]. Unlike thermopile sensors, silicon sensors convert the light energy directly into electrical energy, so they have a very low offset signal (see Figure 2.5).
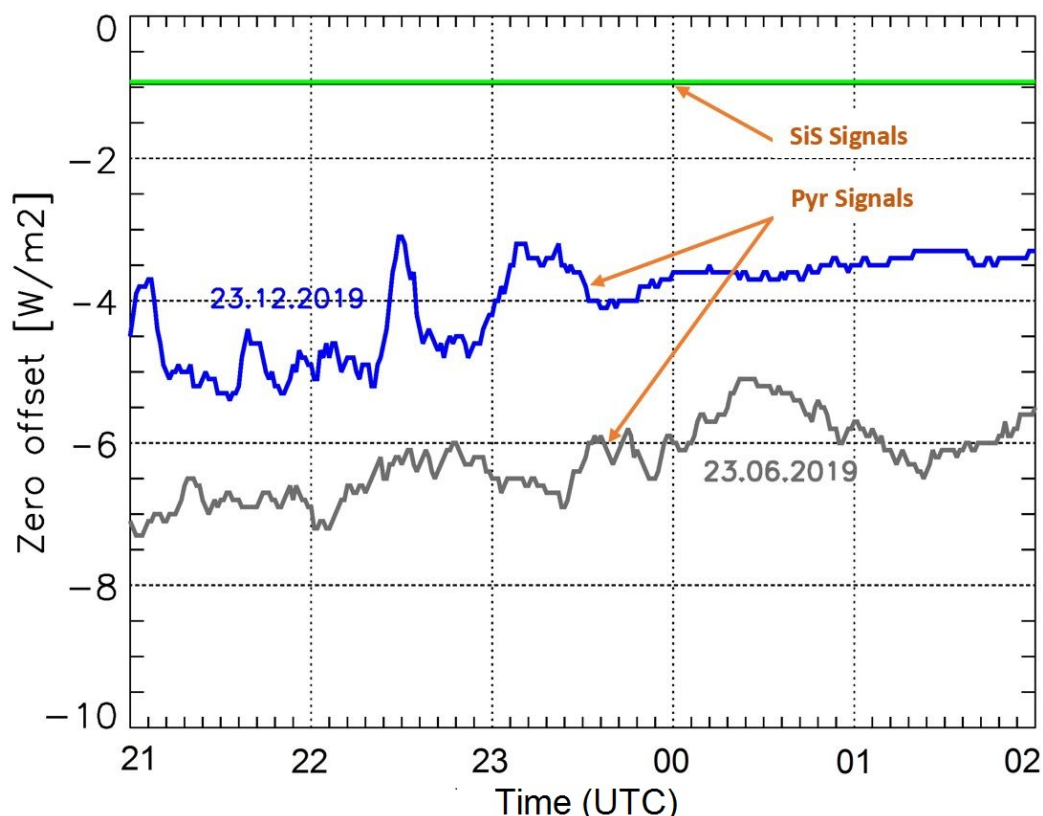
Figure 2.5: Zero-offset data of thermopile and silicon sensors measured during the night. Two days were selected; one in summer (23 June) and one in winter (23 December). Both sensors read below zero during the night; the SiS signal is constant over the night and the year, where the Pyr signal shows seasonal dependence.

Figure 2.5 shows zero-offset signals of both Pyr and SiS during the night of 23 June and 23 December of 2019. It can be seen that both sensors read slightly below zero with no irradiance (dark signal). The dark signal of SiS is low (below -1W/m^2), constant over the night, and does not show seasonal dependence. This dark signal may be caused by the data logger, not by the sensor. On the other hand, the negative read of Pyr is higher and changes slightly ($\pm$ 1.5 W/m^2) during the night. Moreover, the negative signal of Pyr increases during the summer; this may return to the increase of temperature differences inside the sensor. The offset signal is negligible at high irradiances but is increasingly important when the available solar irradiance is low.

In this thesis, zero-offset errors have been experimentally corrected by subtracting the average

negative values at night from the pyranometer readings during the day. The neglect of thermal offset error causes a generalized underestimation in solar radiation measurements, that depends on the used sensor. The used correction method may correct the measured irradiance of Pyr only partly because the thermal offset is expected to be higher during the day due to the higher temperature. The ideal correction of thermal offset error required simultaneous measurements for the dark signal of sensors. This can be done by changing the measurement's principal to shade the sensor after each reading or by using similar sensors to measure the thermal offset during the day.

2.2.2 Temperature Correction

One of the main parameters affecting the real-world measurement of solar irradiance is the temperature response. In general, temperature response is the change in a sensor's sensitivity due to the change in ambient temperature. The effect of temperature is lower on thermopile pyranometer data [64],[73],[74] than the measurements of silicon-based sensors [75],[67]. In the latter, the high temperature affects the short-circuit current of the monocrystalline silicon cells, increasing the measured signal [76], as shown in Figure 2.6.
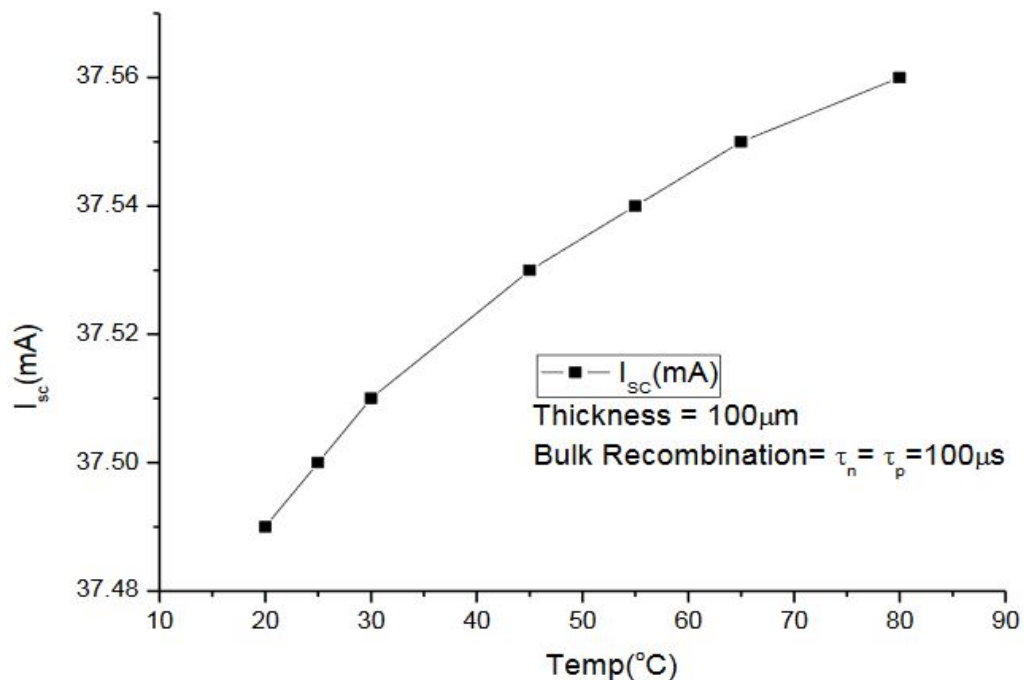
Figure 2.6: Effect of temperature variation on Isc [77].

The daytime temperature of SiS as a reference cell is not simply equal to the ambient temperature, since reference cells are dark in color and, therefore, absorb a greater portion of the solar radiation [78]. Thus, during the day, the silicon sensor operates hotter than the ambient temperature by a factor that depends on the sensor's temperature. As the cell temperature increases, the measured I_{sc} increases, and accordingly, the measured irradiance increases, because the SiS operates next to the short circuit [70]. Unlike photodiode-based pyranometers, the used sensors don't have a temperature compensation that reduces temperature dependency. However, all sensors have internal temperature sensors that can be used to adjust the temperature dependence of the measured irradiance. The temperature response of the silicon-based sensors is usually corrected by using a temperature coefficient (α), which represents the change in the sensor's output with temperature changes. A typical value of α for crystalline silicon sensors is 0.05% /°C and it is the value that is considered by the manufacturer

[70]. The temperature effect has been corrected within this thesis according to the equation:

$$E_{cor} = E_{uncor}(1 + \alpha(T_{sen} - 25°C)).$$ (2.1)

where , E_{uncor}; and E_{cor} are the solar irradiance before and after applying the temperature correction; T_{sen} is the sensor temperature measured by the integrated Pt100 temperature sensor that is mounted to the back of the SiS; and α represents the temperature coefficient (0.05%/°C); the value 25° C is the value used under STC.

Both offset and temperature corrections have been applied on measured irradiance data that are used in the research studies of this thesis. However, SiS data suffer from other measurement uncertainties that influence the accuracy of the data. The most important are the spectral mismatch, the cosine error, and the calibration error. A correction model based on a set of correlations and equations was developed within the thesis to improve the SiS data and to approach the reading of the thermopile sensor. The method addresses the main measurement uncertainties from which the SiS suffers in relation to the thermopile pyranometer. The correction model is explained in detail in [61]. In the following, we will present a short description of the correction methods used in the model.

2.2.3 Cosine Error Correction

The error introduced by the deviation of the angular response of the sensor from the ideal response is known as cosine error. Most of the existing irradiance sensors suffer from the non ideal angular response of their entrance optics, which cause an underestimation of the measured irradiances [79]. In general, cosine error grows with an increasing angle of incidence [80] and is more marked during clear-sky days when beam radiation dominates. The angular response of thermopile pyranometers is mainly a function of the glass domes, the spectral, and spatial uniformity of the black-coated thermopile detector. The used thermopile pyranometer has a good angular response, where the maximum deviation from the ideal angular response is less than 10 W/m^2 (up to an incidence angle of 80°) with respect to 1000 W/m^2 irradiance at normal incidence [64]. In contrast, the cosine error of the used silicon sensor is high, and the deviation from the ideal cosine law increases with an increasing incidence angle, as shown in [61]. This is due to the reflection of incident solar radiation at the sensor's surface, where SiS has a flat glass surface that affects the transmission of light. As cosine error affects the beam irradiance more than diffuse irradiance, which has less dependence on SZA, measurement data have been corrected differently based on sky conditions. The clear-sky irradiance has been corrected according to the sensor's angular response that was measured in the laboratory of the manufacture. In the case of cloudy conditions, data are corrected for the cosine error using the correction factor, which has been obtained as a fit function through empirical measurements.

2.2.4 Spectral Mismatch Correction

Thermopile pyranometers have a flat uniform spectral response and respond to the incident radiation in all wavelengths transmitted through the dome about equally. In contrast, silicon-based sensors have a limited and non-uniform spectral response [81]. Accordingly, using silicon sensors as radiation sensors poses problems associated with its spectral response. The spectral mismatch is the uncertainty introduced by changing the spectral distribution of the incident solar radiation over the time. The major change in the solar global spectrum occurs in the infrared range where water vapor absorption takes place [62]. Silicon-based sensors may also exhibit a response to diffuse radiation that differs from thermopile sensors, introducing additional measurement uncertainty on cloudy days [68]. The difference in spectral response of the sensors should be taken into consideration when comparing the measurement data of both sensors. Within the correction model, spectral correction is applied to SiS data to reduce the spectral mismatch deviation and to approach the reading of Pyr.

Based on the fact that the changes in spectral distribution of beam irradiance differ from that of diffuse irradiance, spectral mismatch factor causes both components to behave differently depending on sky conditions. Thus, spectral mismatch under clear sky conditions has been corrected in a way that differs from that under cloudy conditions. Under clear sky conditions, the spectral mismatch correction factor (SMM) was determined by comparing the spectral distribution of solar irradiance over the day to the AM1.5 spectral distribution that is used for the calibration. For cloudy days, the SMM was obtained as a fit function through empirical measurements.

2.2.5 Calibration Correction

The calibration of silicon sensors used in this work is carried out under STC: 1000W/m^2 of irradiance; AM1.5 spectrum; and 25° C of cell temperature. In fact, these reference conditions are hardly obtainable in the outdoor measurements. Operating the sensors under real atmospheric conditions that differ from the STC introduces a calibration error. In this work, we estimated the calibration error for the clear sky conditions by comparing the irradiance measured by both sensors in outdoor conditions close to the standard test conditions. In the case of cloudy conditions, the calibration factor was obtained as a fit function through empirical measurements.

3 Optimal Tilt Angle

In this chapter, the optimal tilt angle for the south-facing solar systems throughout the year was investigated based on the measured tilted irradiance to ensure the maximum energy generation for both thermal and photovoltaic applications. Moreover, the optimal tilt angle in the individual months was also considered to offer all possible solutions for installing solar systems in Hannover.

3.1 Optimal Orientation of Solar Collectors in Hannover

System properties and prevailing weather conditions play the key role in the energy yield of any solar energy-based system. However, some of the system losses are a function of the installation properties. Angular losses, for example, are governed by the incidence angle of the irradiation, which is influenced by the orientation of the receiving surface. The main objective when installing a solar system is to receive the maximum energy output, while avoiding shading. To achieve this, the solar collector must be positioned so that the sun rays arrive perpendicular to the collector. If not, it does not produce as much power as it could. One possibility to collect the maximum possible daily energy is to use solar tracking systems. However, sun trackers are usually expensive and they are not always applicable [82]. Therefore, most solar PV systems, especially the rooftop systems, are fixed-oriented PV systems. Selecting the optimal tilt angle for these systems is very crucial to secure the maximum system performance.
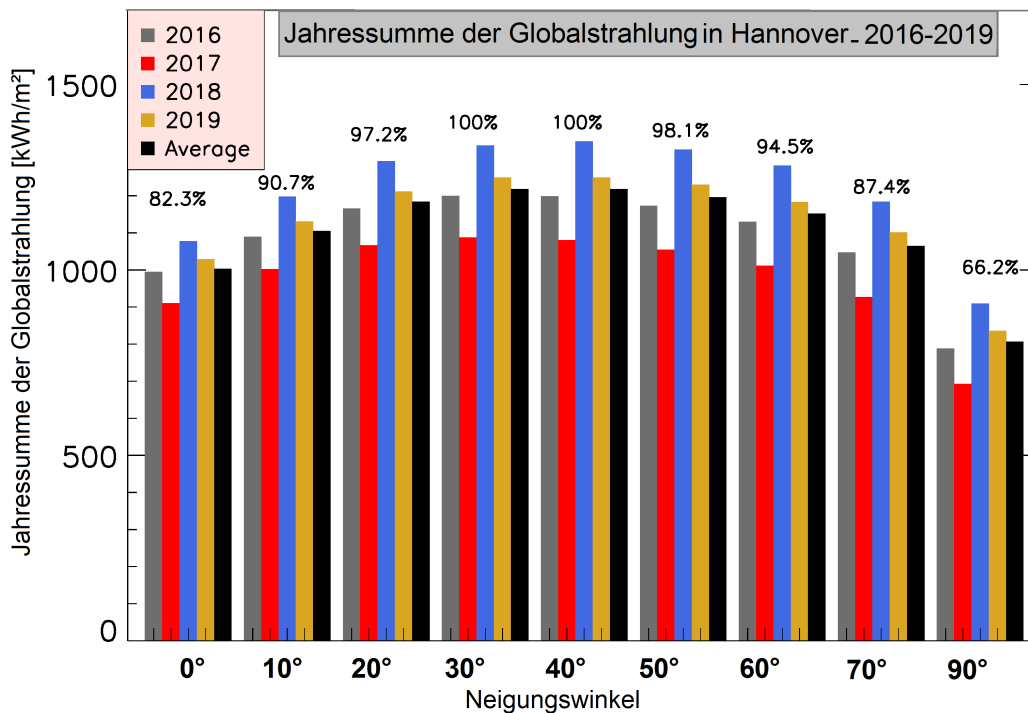

Figure 3.1: Annual global irradiation from 2016 to 2019 and the average values (black) measured by the south-facing sensors at IMuK and its percentage from the maximum value as a function in the tilt angle. The annual irradiation changes significantly from year to year with a maximum between 30° and 40°.

This is because the solar radiation reaching the surface of the collector changes according to both the orientation and tilt angle of the collector. In the case of photovoltaic systems, and due to the non-uniform spectral response of the PV device, the seasonal variation in spectral solar radiation should be taken into account for the optimum orientation of PV systems. One of the aims of this thesis is to determine the optimum tilt of south-facing solar systems in Hannover, as most rooftop PV systems in Germany are mainly facing south [83], and compare this with the values obtained from the PV prediction models. For this purpose, measured tilted irradiance data were used to investigate the tilt angle that yields the highest annual irradiation. Figure 3.1 shows the annual global irradiation from 2016 to 2019 and the average values (black) measured by the south-facing sensors and its percentage from the maximum value as functions of surface tilt angle. The histogram shows that the annual solar irradiation changes significantly from year to year and its maximum ranges between 30° and 40°. The annual irradiation decreases gradually with higher or lower tilt angles, while the minimum irradiation is measured by the vertical sensor (S90). Moreover, using the average annual global irradiation, the optimum tilt angle was calculated more precisely using a polynomial fit curve to be 38° (Figure 3.2); this result agrees with the result obtained from the PVGIS model [48]. The solar
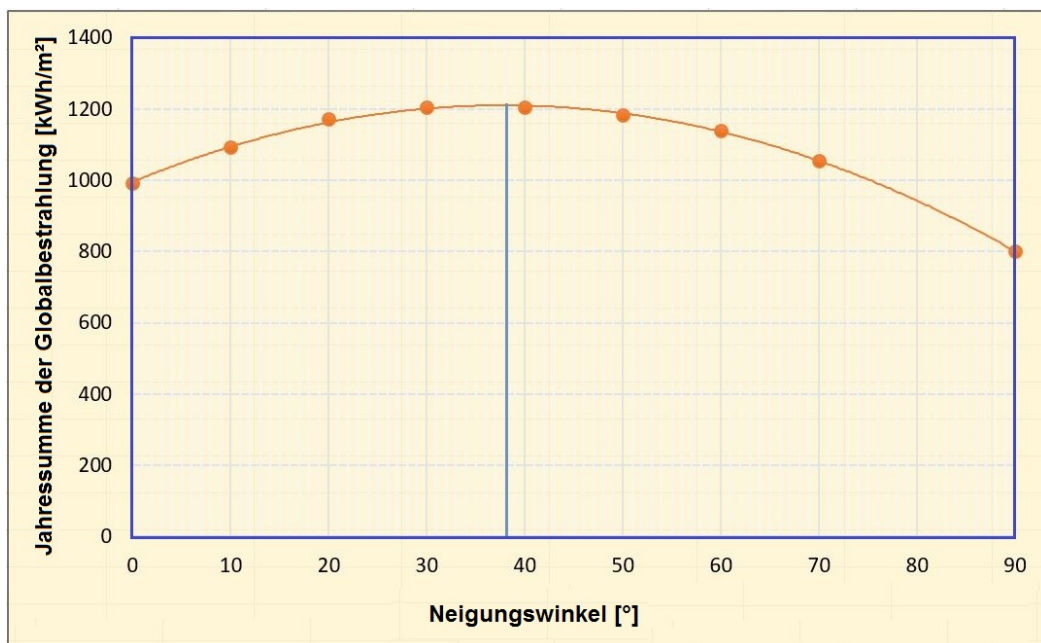

Figure 3.2: Average annual global irradiation (2016-2019) measured at IMuK. A polynomial fit has been used for a precise determination of the optimum tilt angle, which found to be 38° S.

radiation incidence angle varies throughout the year due to the rotation of the earth around its own axis and its elliptical orbit. While the radiation falls to the earth with a steep angle in the summer in the Northern Hemisphere, it falls at a shallow angle in winter months. Therefore, optimum fixed tilt angles of solar collectors should be changed monthly and seasonally. Knowledge of the optimal tilt angle for individual months could be used for planning and comparison purposes. Figure 3.3 shows the average monthly global irradiation measured by south-oriented solar sensors. The monthly optimal tilt angles were found to changed over the year and deviate from the annual value due to seasonal variation of incident solar radiation. During winter months, when the solar angle is low, the high-tilted surfaces receive more solar radiation and accordingly produce more solar-based energy than the low-tilted surfaces. The monthly optimal tilt angle decreases gradually towards the summer months, when the solar elevation angle increases. The monthly optimal tilt angle is found to be at the minimum for the months of May, June, and July (30°) and at the maximum for November, December, and January (70°). The monthly change of the system tilt angle may be feasible for some small solar

PV systems, since it is easy to change the declination of solar collectors. However, in the large-scale PV systems and most of the rooftop systems, monthly changes in the tilt angle are difficult or even impossible. Therefore, the tilt angle of any system should be selected according to the needs of the system owner. In other words, if we aim to produce more solar energy during the summer months, then the system must be tilted at 30° S to collect the maximum solar radiation. In contrast, the system must be tilted at 70° during the winter months to maximize the energy production during the cold season. This result is very similar with the general rule suggested by several researchers that during the winter months solar collectors should be given a tilt of Latitude +15° [84],[85],[86].
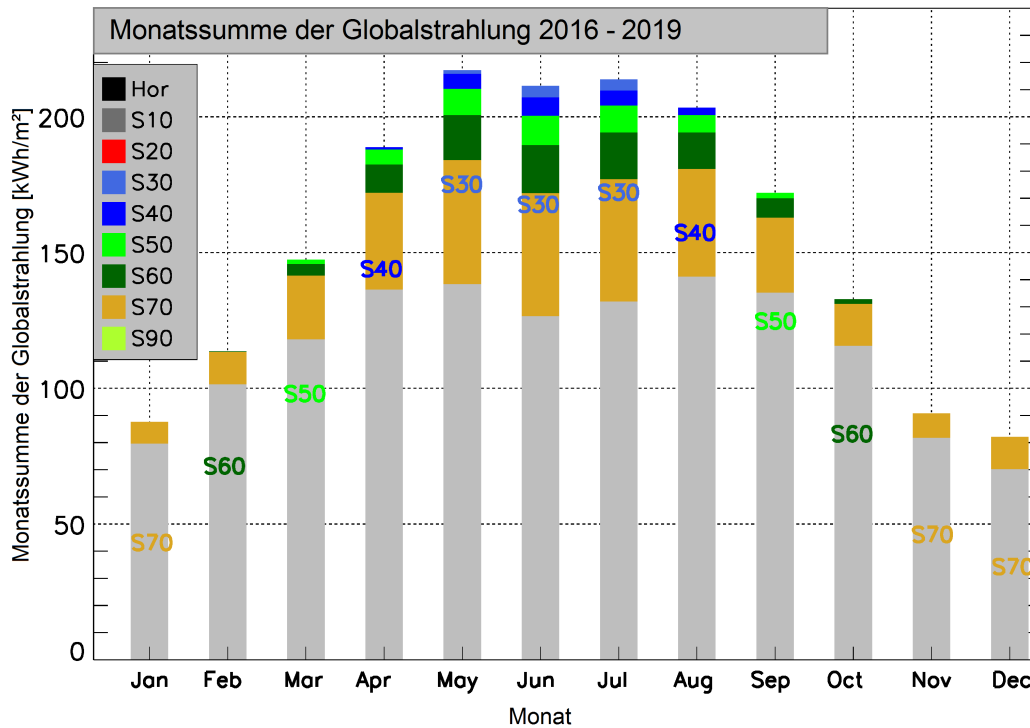

Figure 3.3: Monthly average global irradiation (2016-2019) measured at IMuK. The monthly maximum irradiation and the optimal tilt angle change with the months.

The selection of the optimal tilt angle of the PV system is so far based on the maximum collected solar irradiation (or maximum solar energy production), without considering the energy consumption. The owners of PV systems without feed-in to the grid are more interested in the household electricity self-sufficiency (degree of autarky-AD) that is defined by the proportion of demand met by local generation, i.e., not imported from the grid [87]. In the case of a solar PV system with fixed tilt (e.g., rooftop PV systems), the load curve (electricity demand profile) generally differs from the production curve. Such systems will be beneficial only to the extent of the demand that they are able to cover. Thus, PV solar collectors should be oriented to fit the consumption and to maximize the AD. Producing more energy than the demand for solar systems without feeding into the grid and without a storage system is not significant, because the excess energy will be not used. Therefore, the orientation of the system and the choice of the tilt angle should consider the maximization of the AD.

Using the measurements from IMuK, the power output of the system has been determined and with the help of a set of measured load profiles, the AD of all south orientations has been calculated. The calculations have been used to evaluate the best and more-usable tilt for rooftop PV systems that maximizes the degree of household electricity self-sufficiency.

The load profile used for the calculations is the average of six actual profiles that were measured by HTW Berlin and have an annual consumption between 3900 kWh and 4055 kWh (see [60]). The

Table 3.1: Annual and monthly average daily Autarky (2016-2019)

Tilt	jan	Feb	Mar	Apr	May	Jun	Jul	Aug	Sep	Oct	Nov	Dec	Annual
0°	14.88	27.00	39.85	**49.93**	**57.60**	**60.87**	**58.97**	**53.95**	44.61	31.35	16.72	11.03	38.90
10°	17.59	29.18	40.92	49.87	56.80	59.78	57.95	53.54	45.12	33.19	19.46	14.00	39.78
20°	19.02	30.32	41.52	49.77	56.21	59.05	57.29	53.25	45.47	34.33	21.03	15.64	40.24
30°	19.76	30.92	41.75	49.45	55.51	58.23	56.56	52.78	**45.59**	**34.93**	21.81	16.47	**40.31**
40°	20.11	**31.21**	**41.76**	48.98	54.76	57.34	55.66	52.17	45.48	35.20	22.13	16.86	40.14
50°	**20.14**	31.07	41.61	48.47	54.05	56.61	54.95	51.55	45.32	35.13	**22.14**	**17.00**	39.83
60°	19.96	30.82	41.33	47.84	53.24	55.72	54.19	50.86	45.02	34.81	21.98	16.84	39.38
70°	19.74	30.63	40.80	46.79	51.91	54.21	52.96	49.66	44.39	34.61	21.73	16.71	38.68
90°	18.65	29.62	37.97	43.69	48.31	50.50	49.87	46.43	42.39	33.46	20.11	14.22	36.27

load profiles are measured for German single-family houses with a temporal resolution of 1 min for every day of the year. The average profile has an annual electricity consumption of 4006 kWh that represents a four-person household.

Table 3.1 shows the monthly and annual average of daily AD for all orientations. It can be seen that the horizontal collectors provided the maximum AD during the period from May to August (green cells), while the collectors tilted at 50° provided the maximum valued during the winter period (November, December, and January). The 30° tilt represents the optimal tilt angle for the annual average. The high AD of horizontal collectors during the summer months is due to the fact that the horizontal installation produces more electricity in the mornings and evenings, matching the load profile more closely and increasing the AD.

It can be concluded that the maximum annual solar irradiation for the solar systems in Hannover is collected at 38° south, and the deviation of this tilt leads to a reduction of the collected energy. The monthly optimum tilt angles range between 30° and 70° depending on the sun's height. However, for the PV systems without feed-in, the load profile plays a role in choosing the optimum tilt angle. In this case, the optimum tilt angle is the angle at which the degree of autarky is at the maximum. The calculations show that the horizontal collectors provided the maximum AD during the hot season (May to August), and a tilt of 50° provided the maximum AD during the winter months (November-January). In terms of annual AD-value, the 30° tilt represents the optimal tilt angle. We considered in this chapter only the south-facing orientations; AD can be significantly increased by using combinations between E-W or SE-SW orientations [60] and also by using energy storage and load management.

4 Research articles of this cumulative thesis

In this chapter, the peer-reviewed research articles, which have been written during this PhD work, are presented. At the beginning of each research article, the declaration of the contribution of the author is given.

Research article A: In this study, a two-step algorithm that is capable to synthesize one-minute global irradiance time series based on hourly averaged values has been presented. The method combines the advantages of conventional algorithms and adds new elements like the differentiation of weather conditions. Using the new algorithm, it is possible to synthesize one-minute values of high statistical quality and realistic temporal variability. Moreover, the presented algorithm is location-independent and can be applied to every location worldwide.

Research article B: In this study, we investigated the accuracy of transposition models that are used in photovoltaic prediction models for estimating the global and diffuse solar irradiance on tilted surfaces from data on the horizontal plane. Five transposition models were selected to estimate the tilted irradiance based on the global and diffuse horizontal irradiances with various tilt and azimuth angles. The performance of the models was examined for seven south-facing surfaces tilted at $10°$ intervals between $10°$ and $70°$; and six vertical tilted surfaces facing S, E, SE, SW, W, and N, and a horizontally oriented surface. The calculated values were compared with one-minute values from irradiance sensors facing the same orientation and tilt in Hannover, Germany, and NREL (Golden, CO, USA) in order to produce more significant and spatial applicable results. In addition, the uncertainty caused by using constant albedo value in the calculations was analyzed.

Research article C: We aimed within this study to evaluate the best and most-economic orientations for rooftop PV systems. In this context, we compared different orientations of PV systems in respect to their generated energy, self-consumption rate (SC), and degree of Autarky (AD). The measured irradiance has been used to evaluate the generated photovoltaic energy at various orientations and tilt angles. The SC was calculated by using a set of real, separately measured load profiles from household load data. Further, the results were compared with the simulated values of two widely used PV software packages, PVSOL and PVsyst to validate this software.

Research article D: We focused in this research on the differences between two of the commonly used solar irradiance sensors: thermopile pyranometers and silicon-based sensor. We aimed to analyze the differences between both sensors in order to propose a method to improve the SiS data by minimizing the difference between SiS and Pyr readings using the minimum number of input parameters. We discussed four parameters that influence the sensor measurements, namely the temperature, cosine error, spectral mismatch, and calibration factor. In addition, a correction model was developed to improve the measured SiS-irradiance and to approach the reading of Pyr.

List of additional publications: The following publications are additional co-authored publications that have a reference to the thesis. However, because they are not part of the principal topic, they are not included in this dissertation.

Crisosto, C.; Hofmann, M.; Mubarak, R.; Seckmeyer, G. (2018): One-Hour Prediction of the Global Solar Irradiance from Allsky-Images using Artificial Neural Networks. *Energies* 11, 2906 DOI: 10.3390/en11112906.
A new method was developed to forecast solar irradiance one hour ahead. This new model combines the advantages of using all-sky images and an LM-ANN. The model is also capable of reproducing the nonlinear nature of the solar irradiance more reliably than statistical linear models.

Cordero, R.R.; Damiani, A.; Seckmeyer, G.; Jorquera, J.; Caballero, M.; Rowe, P.; Ferrer, J.; Mubarak, R.; Carrasco, J.; Rondanelli, R.; Matus, M; Laroze, D. (2016): The solar Spectrum in the Atacama Desert
ScientificReports, DOI: 10.1038/srep22457.
In this study, ground-based measurements of spectral solar irradiance at seven locations, include Hannover, were compared. The solar spectrum in Hannover (300-1050nm) was measured by the author of this thesis using a double monochromator-based spectroradiometer.

4.1 Research Article A: Improved Synthesis of Global Irradiance with One-Minute Resolution for PV System Simulations

4.1.1 Declaration of my contribution

Martin Hofmann conceived and designed the study and wrote the draft paper. Together with Gunther Seckmeyer, Stefan Riechelmann, and Cristian Crisosto I contributed to the conception, interpretation, and discussion of the data. All authors contributed substamtoally with comments and revised the manuscript.

4.1.2 Published article

Martin Hofmann, Stefan Riechelmann, Cristian Crisosto, Riyad Mubarak, and Gunther Seckmeyer 2 Improved Synthesis of Global Irradiance with One-Minute Resolution for PV System Simulations. International Journal of Photoenergy 2014:10

Research Article

Improved Synthesis of Global Irradiance with One-Minute Resolution for PV System Simulations

Martin Hofmann,[1] Stefan Riechelmann,[2] Cristian Crisosto,[2] Riyad Mubarak,[2] and Gunther Seckmeyer[2]

[1] *Valentin Software GmbH, Stralauer Platz 34, 10243 Berlin, Germany*
[2] *Institute for Meteorology and Climatology, University Hannover, Herrenhäuser Straße 2, 30419 Hannover, Germany*

Correspondence should be addressed to Martin Hofmann; martin.hofmann@valentin-software.com

High resolution global irradiance time series are needed for accurate simulations of photovoltaic (PV) systems, since the typical volatile PV power output induced by fast irradiance changes cannot be simulated properly with commonly available hourly averages of global irradiance. We present a two-step algorithm that is capable of synthesizing one-minute global irradiance time series based on hourly averaged datasets. The algorithm is initialized by deriving characteristic transition probability matrices (TPM) for different weather conditions (cloudless, broken clouds and overcast) from a large number of high resolution measurements. Once initialized, the algorithm is location-independent and capable of synthesizing one-minute values based on hourly averaged global irradiance of any desired location. The one-minute time series are derived by discrete-time Markov chains based on a TPM that matches the weather condition of the input dataset. One-minute time series generated with the presented algorithm are compared with measured high resolution data and show a better agreement compared to two existing synthesizing algorithms in terms of temporal variability and characteristic frequency distributions of global irradiance and clearness index values. A comparison based on measurements performed in Lindenberg, Germany, and Carpentras, France, shows a reduction of the frequency distribution root mean square errors of more than 60% compared to the two existing synthesizing algorithms.

1. Introduction

The efficiency of PV modules depends mainly on the irradiance, amongst other secondary effects such as module temperature [1, 2]. The nonlinear dependency of the module efficiency on the irradiance and the influence of temperature on the module efficiency require simulations with a high temporal resolution.

For the understanding of the dynamic interaction of PV generator, storage systems, loads, and grids on a world-wide scale, one-minute data series of high quality in terms of realistic variability and frequency distributions are a key factor. Simulating those systems with hourly averaged values neglects significant behavior patterns like short time power enhancements [3].

To illustrate the importance of one-minute data for the simulation of PV systems, a 1 kWp PV example system with

PV generator, DC/AC inverter, and grid is analyzed at the location of HTW Berlin, Germany. DC/AC inverters are used in grid-connected PV systems as power processing interface between the PV power source (DC) and the electric grid (AC). The output power is very sensitive to the temporal variability of the solar radiation which is highest during broken clouds.

In some important markets (e.g., Germany), PV systems can be affected by grid connection restrictions that define the maximum AC power output of the inverter as a percentage of the installed PV power on the DC side, where the usual limit is around 70% [4]. In Figure 1 the power output of the PV example system is shown in a one-minute temporal resolution (grey) and in an hourly averaged temporal resolution (blue) for a day with broken clouds. An energy yield loss of 7% is calculated when the 70% restriction is applied to the hourly averaged power output. When applying the restriction to the
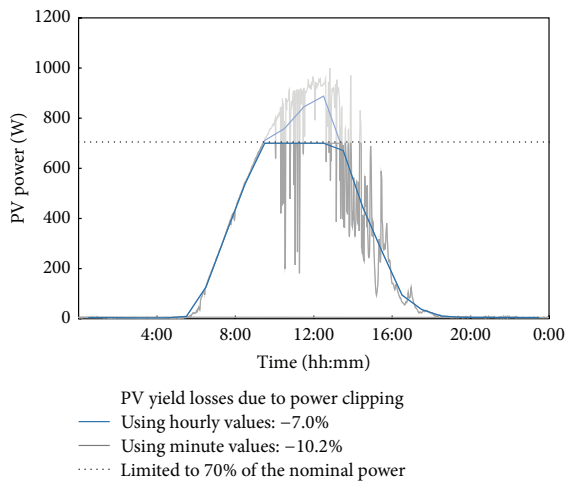
FIGURE 1: Power output of a 1 kWp PV system at HTW Berlin, Germany, on April 01, 2012, measured one-minute values (grey) and hourly averaged values (blue). The yield losses due to maximum power clipping (output power is cut above 700 W) are calculated.
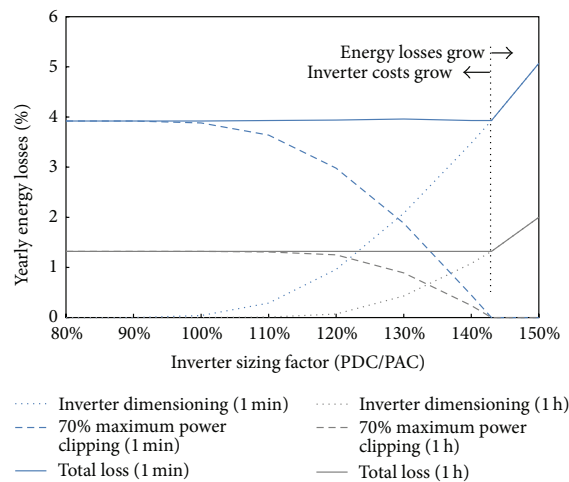

FIGURE 2: Yearly energy yield losses of a 1 kWp PV system at HTW Berlin, Germany, for various inverter sizing factors (the relation between installed PV power on the DC side and nominal AC inverter output) and a maximum power clipping value of 70% (output power is cut at 70% of the installed DC power). Using hourly averaged values for the simulation of PV systems leads to a significant underestimation of the yearly yield losses. With hourly averaged values (grey), the total energy loss is at 1.3% while the more precise simulation with one-minute values (blue) returns a total energy loss of 3.9%. In addition, this figure illustrates that the optimal inverter sizing factor (here, 143%) for systems with maximum power clipping is the reciprocal of the clipping value (70%).

one-minute power output values, an energy yield loss of 10% is calculated.

Following Vanicek et al. in his contribution on the energy yield losses as a function of inverter dimensioning [3], we analyzed the dependency of energy yield losses due to maximum power clipping for PV inverters. Figure 2 shows that these losses are dependent on the inverter sizing factor as well and increase significantly when using one-minute instead of hourly averaged time series. In sum, energy losses due to inverter undersizing and maximum power clipping add up to a constant value within the inverter dimensioning range until the reciprocal of the power clipping value is reached (143%). This threshold marks the optimum inverter sizing factor for PV inverters with maximum power clipping, since losses will not decrease when using a larger inverter. With hourly averaged values (grey), the total energy loss is at 1.3% while the more precise simulation with one-minute values (blue) returns a total energy loss of 3.9%. These examples indicate that the use of hourly averaged irradiance datasets can result in falsified yield predictions.

While there exist several commercial providers and free sources of meteorological data in a resolution of one hour (e.g., Meteotest, SolarGIS, and TMY), covering nearly the whole earth, the availability of measured irradiance data with a resolution of less than an hour is very limited. This limited availability leads to the necessity to synthesize one-minute time series from hourly averaged data.

Several algorithms were developed in the past in order to synthesize one-minute global irradiance datasets with realistic variability and frequency distributions from hourly averaged datasets. The supposedly most established algorithms were developed by Aguiar and Collares-Pereira [5, 6], Skartveit and Olseth [7], and Glasbey [8]. Like many similar algorithms, the aim of those approaches is the reproduction

of the characteristic frequency distributions of the solar irradiance or the clearness index k_t, which is a measure for atmospheric transmission.

The contribution of Aguiar and Collares-Pereira was originally designed for the generation of hourly averaged time series with daily averages as input. It is based on the modeling of probability densities as Gaussian functions that depend on the clearness index k_t. Skartveit and Olseth focused on the modeling of frequency distributions of global and direct irradiance, depending on intrahour and interhour irradiance variability, while using first-order autocorrelation for the generation of the actual time series. Glasbey proposed nonlinear autoregressive time series generation with joint marginal distributions as multivariate Gaussian mixtures. The estimation of probability density distributions of the irradiance has recently been investigated by Voskrebenzev et al. [9].

Other important contributions to this topic were provided by Assunção et al. [10] with investigations on the dependency of k_t from the air mass and by Tovar et al. [11] with the analysis of the relation of hourly averaged *[clearness indices]* to one-minute clearness indices.

However, current algorithms only insufficiently withstand the validation against measurement values, since they underestimate irradiance enhancements caused by broken

clouds, overestimate mid irradiance values, and provide one-minute time series with a variability that is too high.

Therefore, we developed an improved algorithm capable of synthesizing one-minute global irradiance time series based on hourly averaged global irradiance. The algorithm takes three different weather conditions (cloudless, broken clouds and overcast) into consideration. We show that the improved algorithm exceeds the performance of the Aguiar and the Skartveit algorithm in terms of temporal variability and characteristic frequency distributions for the calculation of short-term global irradiance at two exemplary PV installation locations.

2. Measurement Data and Methodology

The new algorithm consists of two parts. The first part comprises a data preparation process that categorizes the input dataset and produces transition probability matrices (TPM) for three weather conditions: cloudless, broken clouds and overcast. The preparation process has to be executed only once.

The input dataset used for the initialization consists of global irradiance measurements conducted by the Baseline Surface Radiation Network (BSRN), featuring more than 50 locations all over the world with up to 20 years of measurements. The BSRN database is updated continuously with new measurement data; in this study we used a snapshot of May 2013. A subset of these data, one-minute global irradiance measurements performed in Lindenberg, Germany (2005), and Carpentras, France (2001), is used for the model validation.

The second part is the synthesis process for one-minute time series from hourly averaged time series. The required input of this process only consists of the prepared set of TPM and the hourly averaged time series of global irradiance that is to be disaggregated. The core of the process is based on Markov chains [12, 13], utilized in a similar way by McCracken [14].

The central idea in both parts of the new algorithm is the classification of weather situations by the temporal feature of the clearness index. In the first part, the preparation process, the BSRN dataset is split into three individual datasets corresponding to three weather conditions: cloudless, broken clouds and overcast. Each subset is then processed separately and transformed into a transition probability matrix. In the second part, the synthesis process, each daily dataset of the hourly averaged input values is categorized as well and processed according to their weather category. As a consequence, the main process steps of the new algorithm are only depending on those weather categories, in disregard of specific location information.

This leads to the advantage that the algorithm can be applied to hourly averaged datasets of arbitrary locations. Furthermore, the only required input is the hourly averaged datasets, once the TPM are created. Hence, the new algorithm combines aspects of existing work on this subject with a universally applicable method for the synthesis of one-minute time series from hourly averaged values.

2.1. Classification of Weather Condition by the Clearness Index. The determination of predominant weather conditions is needed in both steps of the presented algorithm. The weather conditions are determined by the calculation of the clearness index k_t. The clearness index is defined as the ratio of measured global irradiance $E_{measured}$ at Earth's surface and the irradiance calculated for cloudless conditions at the particular measuring site, denoted by clear sky irradiance E_{clear}:

$$k_t = \frac{E_{measured}}{E_{clear}}. \tag{1}$$

The calculation of the clear sky irradiance has a significant influence on the k_t index. A modification of Bourges' calculation [15] is used in this work, since it provided the best results for all analyzed locations:

$$E_{clear} = 0.78 E_{ext} \sin{(\gamma_S)}^{1.15}, \tag{2}$$

where γ_S is the elevation of the sun and E_{ext} is the extraterrestrial irradiance. The extraterrestrial irradiance E_{ext} was calculated using Maxwell's approach [16], whereas the elevation of the sun γ_S was modelled by the algorithm of Reda and Andreas [17] from NREL.

The predominant weather condition on a particular day results in a characteristic temporal pattern of k_t that can be used to categorize the day into one of the three classes. The detection algorithm of the weather condition is based on the daily average of hourly averaged k_t values $\overline{k}_{t,day}$ and the variability during a day $\widetilde{k}_{t,day}$:

$$\overline{k}_{t,day} = \frac{1}{n} \sum_{i=1}^{24} k_{t,i}, \qquad \widetilde{k}_{t,day} = \frac{1}{n} \sum_{i=2}^{24} |k_{t,i} - k_{t,i-1}|, \tag{3}$$

where n is the number of hours where global and clear sky irradiance is above 0 W/m^2.

Table 1 gives an overview about the three weather classes and their detection conditions. An example for the classification is shown in Figure 3 for some days in August 2005 in Lindenberg, Germany. For a better visualization we fall back on one-minute values here, whereas it is to be noted that the detection is based on hourly averaged values of the clearness index k_t, because these values form the input of the synthesis algorithm. The classification conditions are visualized as well in Figure 4 for an example dataset of Lindenberg, Germany.

2.2. Transition Probability Matrices. For each class that represents a specific weather situation, matrices of transition probabilities (TPM) are created. The TPM contain information on how probable the switch is from one specific k_t at time i to another value at the time $i + 1$. To create those matrices, diurnal courses of measured one-minute values of equal weather class, independent of their location, are analyzed and converted into a common matrix. The frequency of every possible transition in the measured data is registered and afterwards normalized to obtain the transition probabilities. Therefore, a TPM contains all probabilities of the change of

TABLE 1: Overview of the three weather classes and their detection conditions.

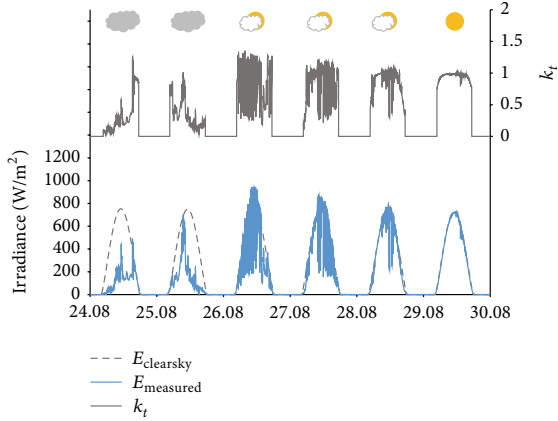| Weather class	Condition
Overcast	$0.6 - \bar{k}_{t,\text{day}} > \tilde{k}_{t,\text{day}}$
Cloudless	$-0.72 + 0.8\bar{k}_{t,\text{day}} \geq \tilde{k}_{t,\text{day}}$
Broken clouds	Otherwise

FIGURE 3: Example results of the weather category detection algorithm based on k_t patterns for 6 subsequent days from 24.08.2005 to 30.08.2005 in Lindenberg. Clear sky irradiance (dotted grey) and the clearness index (grey line on top) in comparison to the measured global irradiance (blue line, bottom). Visualization is done with one-minute values whereas the detection is based on hourly averaged values.

FIGURE 4: Visualization of the classification of weather conditions by k_t patterns using measurement values from Lindenberg, Germany. Cloudless days feature high daily means $\bar{k}_{t,\text{day}}$ with only little daily variability $\tilde{k}_{t,\text{day}}$. Days with overcast sky can be characterized by low daily means and low to mid variability. Days with broken clouds feature a high daily variability and mid to high daily means. The black points refer to the example days of Figure 3.

a specific value of $k_{t,i}$ to $k_{t,i+1}$ from one minute to the next under a specific weather condition. An example for a TPM of broken clouds weather condition is given in Table 2. In this case, the probability of k_t to change from 0.1 to 0.09 during one minute is 17.6%, the probability to stay the same is 53.2%, and the probability to change from 0.1 to 0.01 is 0%.

The excerpt of a TPM shown in Table 2 is an example of how such transition probability matrices are structured. The actual values of the TPM however are subject to the underlying dataset that is used to create those matrices. In this study we will use different subsets of the BSRN databases for the creation process, depending on the dataset we use for validation. The validation dataset is omitted from the dataset for the TPM creation process to avoid self-reference. Hence, the resulting values in the matrices may vary, whereas the presented method to create the matrices is universal. For this reason we refrain from listing all 200×200 TPM in this study.

Since the TPM are created using real weather data in one-minute resolution, each measured irradiance within a given time interval leaves a fingerprint in a TPM. Hence, the spatial and temporal validity of the algorithm is increasing with the number of input datasets. As of May 2013, the BSRN comprises more than 6900 irradiance measurement months distributed globally, which is equal to more than 200 000 measurement days in one-minute resolution that leave their fingerprint in the TPM. The influence of the number of input
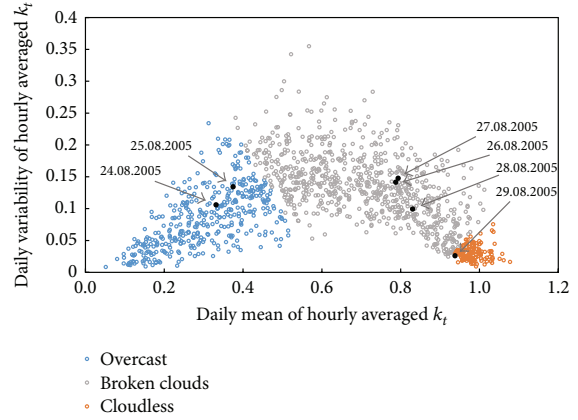
data on the synthesis quality is referred to in Results section as well.

2.3. Generation of k_t Sequences with Markov Chains. To generate one-minute values from hourly averaged sequences of the global irradiance, the weather condition of the day in question is detected at first. Depending on the weather condition the correspondent k_t-TPM is chosen.

The actual generation of the one-minute values is conducted with the help of the so-called discrete-time Markov chains (DTMC). DTMC is a state-based process for the modelling of real-world events. In the first order, the process is memory-less, so that the next state only depends on the current state [12, 13].

To determine the successor $k_{t,i+1}$ of a specific k_t value $k_{t,i}$ at a given point in time i, the probabilities belonging to $k_{t,i}$ are cumulated. Then, a Markov number between 0 and 1 is generated and inserted as a threshold value into the cumulated probability function. The point at which the probability function is bigger than the Markov number for the first time is defined as $k_{t,i+1}$. The process continues in the same manner and generates a chain of 60 k_t values per hour. From these k_t sequences, the global irradiance for every point in time can be calculated with the help of the clear sky irradiance:

$$E_{\text{generated},i} = k_{\text{t},i} \cdot E_{\text{clear sky},i}. \tag{4}$$

This process is repeated until the mean value of the generated one-minute values equals the hourly averaged input value

TABLE 2: Excerpt of an example TPM for broken clouds weather condition. For each k_t value at time i (rows), the probability of a switch to another k_t at time $i + 1$ (columns) is given. The k_t values range from 0 to 2.

$k_{t,i}$	$k_{t,i+1}$											
	0	0.01	0.02	0.03	0.04	0.05	0.06	0.07	0.08	0.09	0.1	$\cdots$
0	0	0	0	0	0	0	0	0	0	0	0	
0.01	0	0.82927	0.17073	0	0	0	0	0	0	0	0	
0.02	0	0.10345	0.72414	0.17241	0	0	0	0	0	0	0	
0.03	0	0	0.06897	0.76724	0.15517	0	0.00862	0	0	0	0	
0.04	0	0	0.00709	0.12057	0.70922	0.14894	0.01418	0	0	0	0	
0.05	0	0	0	0	0.07004	0.75875	0.15564	0.01167	0.00389	0	0	
0.06	0	0	0	0	0.01136	0.14773	0.64394	0.14773	0.03788	0.00758	0.00379	
0.07	0	0	0	0	0	0.0084	0.19328	0.53361	0.2395	0.02521	0	
0.08	0	0	0	0	0.0059	0	0.0236	0.17109	0.57817	0.17404	0.03245	
0.09	0	0	0	0	0	0	0	0.03378	0.19932	0.46959	0.21284	
0.1	0	0	0	0	0	0	0	0	0.02067	0.17571	0.5323	
$\cdots$												

E_{hour} with desired accuracy δ. If necessary, the values are scaled as well:

$$\left| \frac{E_{\text{hour}}}{\sum_{i=1}^{60} E_{\text{generated},i}} - 1 \right| < \delta,$$

$$E_{\text{gen., scaled},i} = \frac{E_{\text{hour}}}{\sum_{m=1}^{60} E_{\text{generated},m}} E_{\text{generated},i}. \tag{5}$$

3. Results

In the following section the new algorithm is validated with measurement data and compared to the algorithms by Aguiar and Skartveit. The result comparison is conducted for two exemplary datasets of one year at two different locations: Lindenberg, Germany, 2005, and Carpentras, France, 2001. Both datasets are taken from the BSRN database. To avoid self-reference in the presented results, the creation process of the TPM excludes all measurement data of the respective location.

First, the results are presented on the basis of diurnal courses to assess the temporal variability, afterwards in the form of frequency distributions. In addition we provide a table with comparative uncertainties.

When assessing the temporal variability of synthetized one-minute values, the results for days with broken clouds and overcast skies are more important, since the simulation of sunny days is not difficult. In Figure 5 the measured course of the global irradiance (black (a)) is displayed in comparison to the temporal course of the values generated with the new algorithm (blue (b)) and the algorithms by Aguiar (c) and Skartveit (d) for an overcast day.

Although the exact occurrence of irradiance peaks in the modelled time series may differ from the measured time series, the variability of the values modelled with the new algorithm agrees with measured values to a very high degree. The mean variability of irradiance changes from one minute to the next is 7.0 W/m^2 for measured time series, whereas it is 8.2 W/m^2 for the data modelled with the new algorithm

in the example dataset of Figure 5. With n being the number of minutes of a day (1440), the mean variability of the global irradiance is calculated as follows:

$$\overline{E_{\text{var}}} = \frac{1}{n} \sum_{i=2}^{n} \left| E_i - E_{i-1} \right|. \tag{6}$$

The methods of Aguiar and Skartveit lead to higher mean variability values of 13.1 W/m^2 and 16.6 W/m^2, respectively. Scientists of the Sandia National Laboratories as well refrain from using these algorithms for this reason:

> Without an adequate method to account for auto-correlations (of relatively high order) in the one-minute time series of clearness index, simulations using these distribution forms would likely prove too variable, as we found for simulations using Glasbey's model, and as we suspect would have resulted using the model of Skartveit and Olseth [18].

A more complete picture of the variability of solar irradiance can be obtained by analyzing the frequency of its gradients over a whole year. The gradients, in this case the absolute difference of the irradiance values of one minute to the next for the measured data and model data, are calculated and transferred into frequency plots. Figure 6 shows the frequency of irradiance gradients for Lindenberg, 2005, whereas the data for Carpentras, 2001, is displayed in Figure 7.

In both cases, the frequency distribution of the data modelled by the algorithms of Aguiar and Skartveit, respectively, shows significant overestimations for the gradient range from 10 to 100 W/m^2, while the new algorithm is able to produce irradiance values that feature a similar frequency distribution in this range. For gradients of less than 10 W/m^2 the data modelled by all algorithms show similar deviations from the measured data. For gradients of more than 100 W/m^2, the new algorithm and the approach of Skartveit display similar
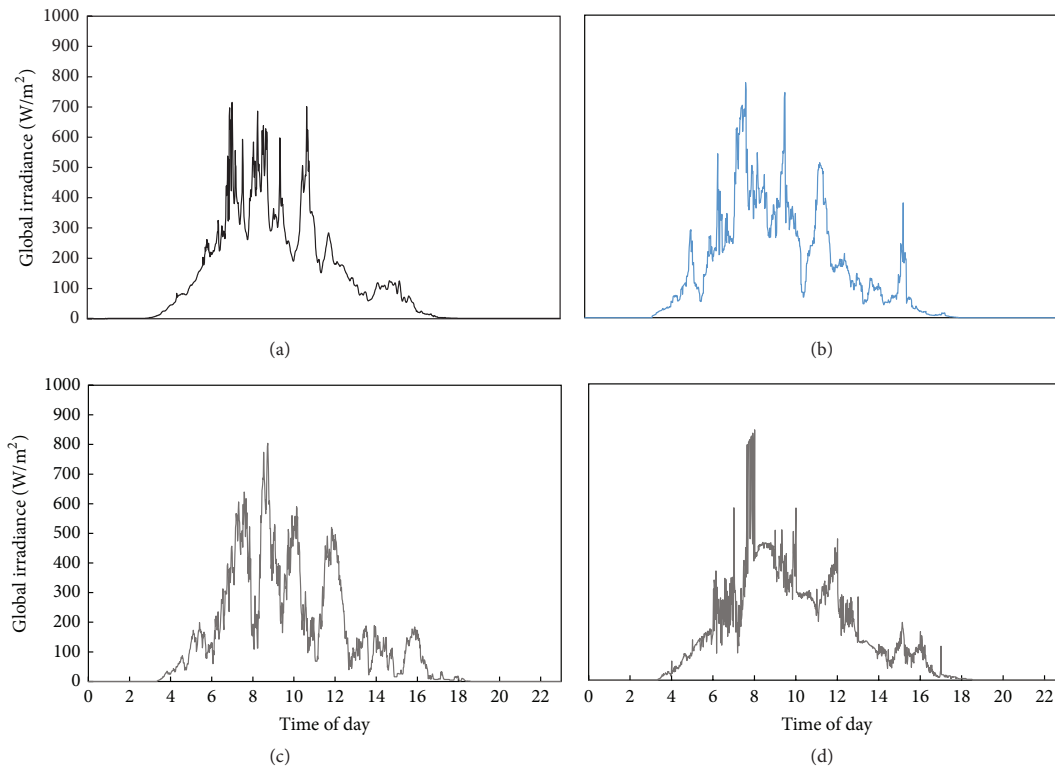
FIGURE 5: Lindenberg, May 14, 2005. The temporal course of the measured global irradiance (a) on a day that was rated as a day with overcast sky is compared to values generated by the new algorithm (b), the algorithm by Aguiar (c), and the algorithm by Skartveit (d). The mean variability, that is, the mean irradiance change from one minute to the next, of the measured irradiance of 7.0 W/m^2 shows good congruence with the new algorithm (8.2 W/m^2), while the usage of the algorithms by Aguiar and Skartveit leads to higher variability values of 13.1 W/m^2 and 16.6 W/m^2.

quality, whereas the algorithm of Aguiar shows significant underestimations for both locations.

For the transfer into deviation indicators, the deviations of the modelled data from the measured ones for each irradiance value are squared, weighed by its frequency, and summed up. The frequency weight f_i is added in order to obtain information about the energetic relevance of each irradiance gradient. For the calculation of root mean square errors, these sums are then divided by the number of gradient steps and the square root is applied. Table 3 shows the results for all three analyzed models. In accordance with the visual impression of the frequency plots in Figures 6 and 7, the RMSE values for the new model presented in this study are significantly smaller than the RMSE values of the other two models by Aguiar and Skartveit:

$$\text{RMSE} = \sqrt{\frac{1}{n}\sum_{i=1}^{n}\left(f_i\left(x_{\text{Model},i} - x_{\text{Measurement},i}\right)\right)^2}. \quad (7)$$

Since the frequency distributions of the global irradiance and the k_t values are more reliable indicators for the applicability to simulations of photovoltaic systems, they are displayed

TABLE 3: Root mean square errors (RMSE) of the frequency distributions of irradiance gradients of modelled data versus measurement in W/m^2. The new model is able to produce significantly smaller values of RMSE than the models of Aguiar and Skartveit for both locations, Lindenberg, 2005, and Carpentras, 2001.

Model	Lindenberg	Carpentras
Aguiar	8131	8541
Skartveit	4758	5112
New	2787	3218

in Figures 8, 9, 10, and 11. Measured values (black) are compared to values calculated by the conventional algorithms by Aguiar and Skartveit (grey dotted and solid), as well as to the new algorithm presented in this study (blue). Each of these distributions is calculated from values of one whole year.

For the generation of those figures, measured one-minute values were averaged to hourly means, which were then fractionized again using the new improved algorithm as
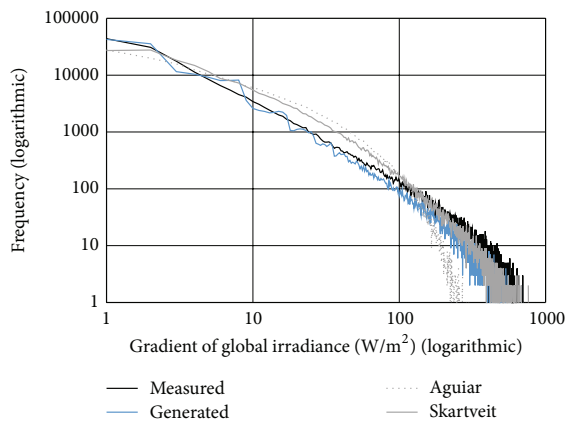
FIGURE 6: Frequency of gradients of the global irradiance in Lindenberg, Germany (2005). The model quality in lower gradient ranges of up to 10 W/m^2 is similar in all models. In the range of 10 to 100 W/m^2, significant deviations can be detected for the models of Aguiar and Skartveit (grey), whereas the new method (blue) shows good congruence. For gradient values of more than 100 W/m^2, the model of Aguiar underestimates the frequency significantly, while the new method and the method of Skartveit feature similar frequency values compared to the measurement data (black).

well as the approaches of Aguiar and Skartveit. The figures show how often a specific irradiance value occurs in a year. The maximum at high irradiance values represents clear sky situations, while the second maximum at lower values is evoked by skies covered by clouds. Hence, the maximum at high irradiance values is considerably more pronounced at sunnier locations than at locations with very variable weather.

It can be seen that the new algorithm is reproducing the frequency distributions of the global irradiance much better than the conventional approaches. Mid irradiance values are not overestimated, and a good modelling quality is present at high irradiance values. However, very high irradiances above 1100 W/m^2 are slightly overestimated.

If those frequency distributions are looked at in the form of the clearness index k_t, the problems of the existing algorithms become equally apparent (see Figures 10 and 11). With the improved algorithm the k_t distributions can be reproduced very well, and the typical bimodal character of the distribution is modelled very precisely for cloudy locations (Lindenberg) as well as for sunnier locations (Carpentras) with a pronounced clear sky peak of a k_t value near 1. The practical relevance of these effects was demonstrated with the help of the introductory example of the maximum power clipping at 70%.

These visual impressions give an indication, but an analysis of the uncertainty can be used for quantitative assessment. Table 4 lists root mean square errors (RMSE) for all distribution diagrams shown in Figures 8–11. For each irradiance or clearness index class i the modelled distributions are compared to the measured data, and the deviations are squared and summed up for the whole range
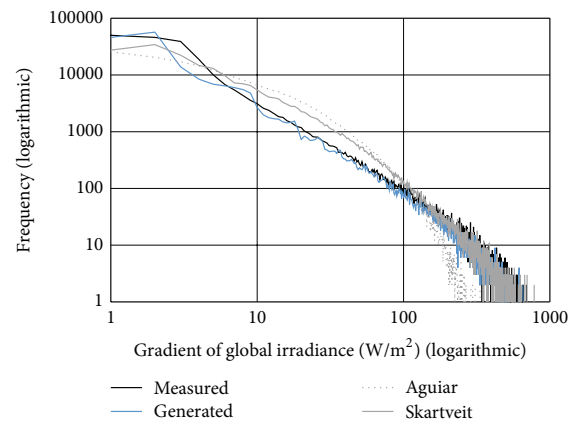

FIGURE 7: Frequency of gradients of the global irradiance in Carpentras, France (2001). As in Figure 6, the differences of the models for gradient values of less than 10 W/m^2 are comparable. In the range of 10 to 100 W/m^2, the new model (blue) shows a better congruence with the measured data (black) than the models of Aguiar and Skartveit (grey), while only the model of Aguiar fails to produce good congruence for gradient values of more than 100 W/m^2.

TABLE 4: Root mean square error (RMSE) values comparing the frequency distributions of the existing and the new algorithms with measured data. Smaller values of RMSE denote better congruence of the frequency distributions of modelled one-minute values with measured values.

Model	RMSE of irradiance in %		RMSE of k_t in counts	
	Lindenberg	Carpentras	Lindenberg	Carpentras
Aguiar	0.530	0.549	596	801
Skartveit	0.684	0.575	862	962
New	0.210	0.237	207	248

and then divided by the number of classes n. The square root of this value gives the RMSE listed:

$$\text{RMSE} = \sqrt{\frac{1}{n}\sum_{i=1}^{n}\left(x_{\text{Model},i} - x_{\text{Measurement},i}\right)^2}. \qquad (8)$$

The RMSE of both the irradiance and the clearness index distributions can be considerably decreased with the new algorithm compared to the conventional ones. In the case of Carpentras both distribution RMSE can be reduced between 24 % and 35 %, in case of Lindenberg between 31 % and 43 %.

To analyze the influence of the amount of input data for the TPM on the synthesis quality of the algorithm, the creation process of the TPM is varied as follows.

First, the algorithm is processed three times with its original setup, which includes all TPM except the ones from the respective location, to estimate the influence of the random Markov number generator on the RMSE range. Second, only TPM of the respective location are used. In a third iteration, the only measurement values included in the creation process are taken from BSRN stations that are located in the same
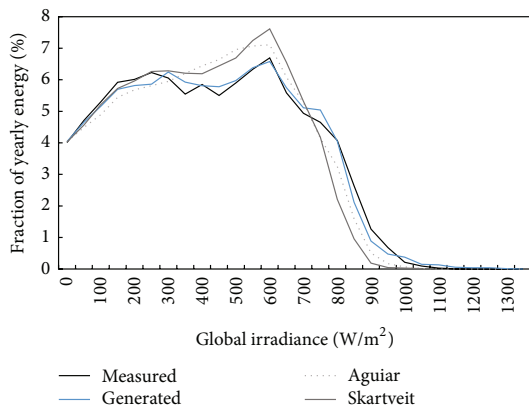
FIGURE 8: Frequency distributions of measured global irradiance for Lindenberg (Germany, 2005) against values generated by different algorithms. Mid values are slightly overestimated, and high values are underestimated by the existing models (grey dotted), resulting in RMSE of 0.530% for Aguiar and 0.684% for Skartveit. The modelling quality of the new method (blue) does not overestimate mid irradiance values and shows only little underestimation of high irradiance values. The new RMSE can be reduced to 0.210%.
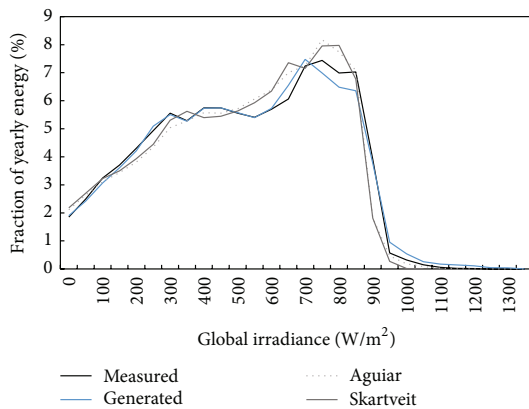

FIGURE 9: Frequency distributions of measured global irradiance for Carpentras (France, 2001) against values generated by different algorithms. For locations with higher yearly global irradiation, the high irradiance peak grows. Mid values are slightly overestimated, and high values are underestimated by the existing models (grey dotted), resulting in RMSE of 0.549% for Aguiar and 0.575% for Skartveit. The modelling quality of the new method (blue) does not overestimate mid irradiance values and shows only little underestimation of high irradiance values. The new RMSE can be reduced to 0.237%.

FIGURE 10: Frequency distributions of the clearness index k_t for Lindenberg (Germany, 2005). With the new method, the RMSE between measurement and synthesis can be reduced significantly (RMSE = 596 and 862 counts for Aguiar and Skartveit and RMSE = 207 counts for new method).

FIGURE 11: Frequency distributions of the clearness index k_t for Carpentras (France, 2001). For locations with higher yearly global irradiation, the second peak (clear sky) of the distribution grows. With the new method, the RMSE between measurement and synthesis can be reduced significantly (RMSE = 801 and 962 counts for Aguiar and Skartveit and RMSE = 248 counts for new method).

climate zone as per the definition of Köppen [19]. Current data published by Rubel and Kottek [20] is taken to assign the locations to climate zones. Lindenberg is located in the climate zone *Cfb,* which mainly comprises Western Europe. In the BSRN dataset there are another seven locations in this climate zone: Cabauw (the Netherlands), Camborne and Lerwick (Great Britain), Cener (Spain), Lauder (New Zealand),
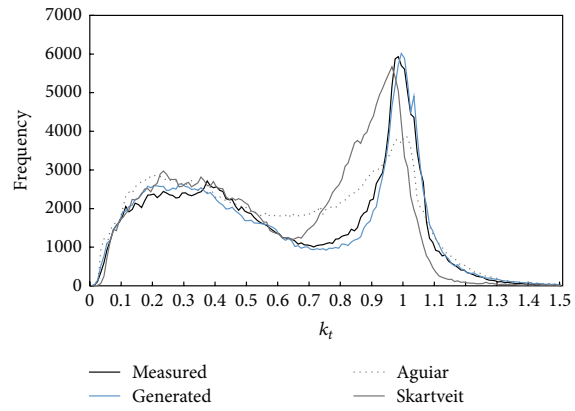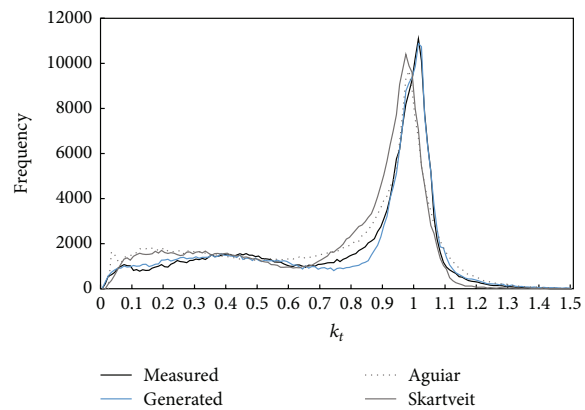
Palaiseau (France), and Payerne (Switzerland). According to Rubel and Kottek, Carpentras lies in climate zone *Csa*, but unfortunately there is no other location of this climate zone in the BSRN dataset. So this third iteration is conducted for Lindenberg only. The fourth iteration comprises the usage of all available TPM, this time including the TPM of Lindenberg and Carpentras.

The synthesis of one-minute irradiance values is now repeated with all varied TPM. The RMSE values are determined according to the previous chapter. Table 5 compares the error values of the variations with the original version of the process.

TABLE 5: Comparison of synthesis quality of the new algorithm as a function of input data for the locations of Lindenberg, Germany, 2005, and Carpentras, France, 2001.

Variation	RMSE of irradiance in %		RMSE of k_t in counts	
	Lindenberg	Carpentras	Lindenberg	Carpentras
All except own (1)	0.210	0.237	207	248
All except own (2)	0.244	0.174	210	273
All except own (3)	0.235	0.217	204	239
Own TPM only	0.232	0.199	202	279
Cfb only	0.193	—	315	—
All TPM	0.253	0.186	204	254

The repetition of the synthesis process with the original setup (all TPM except own 1–3) demonstrates the RMSE range that can be expected due to the random nature of the Markov number generator. The interesting aspect of the various TPM modifications (own TPM only, *Cfb* TPM only, and all TPM) is that the resulting RMSE mostly lie well within the natural RMSE range of the original algorithm. In other words, the synthesis quality remains approximately the same, whether the algorithm uses only data of the respective location or all globally available data except those from the respective location. By classifying the weather situation on a daily level, the influence of location specific weather phenomena is reduced at the best. This implies that the presented algorithm is location-independent and can be applied to every location worldwide.

4. Conclusions

An improved method for synthesizing one-minute time series of global irradiance has been presented that was developed on the basis of a large worldwide measurement dataset. It combines the advantages of conventional algorithms and adds new elements like the differentiation of weather conditions. It could be demonstrated that with the new approach it is possible to synthesize one-minute values of high statistical quality and realistic temporal variability. The independence on the location has been shown for selected cases. Such an independence would allow synthesizing one-minute time series for any location.

Conflict of Interests

The authors declare that there is no conflict of interests regarding the publication of this paper.

Acknowledgments

References

[1] R. Haselhuhn, U. Hartmann, and P. Vanicek, "Uncertainty in yield prediction—what are the causes, how can they be reduced?" in *Proceedings of the 25th European Photovoltaic Solar Energy Conference and Exhibition*, pp. 4722–4725, 2010.

[2] B. Herteleer, J. Cappelle, and J. Driesen, "Quantifying low-light behaviour of photovoltaic modules by identifying their irradiance-dependent efficiency from data sheets," in *Proceedings of the 27th European Photovoltaic Solar Energy Conference and Exhibition*, pp. 3714–3719, 2012.

[3] P. Vanicek, G. Karg, and R. Haselhuhn, "Quality of the calculation of inverter losses with standard simulation programs," in *Proceedings of the 26th European Photovoltaic Solar Energy Conference and Exhibition*, pp. 3772–3775, 2011.

[4] EEG, *Act on Granting Priority to Renewable Energy Sources*, Renewable Energy Sources Act, EEG, 2012.

[5] R. J. Aguiar, M. Collares-Pereira, and J. P. Conde, "Simple procedure for generating sequences of daily radiation values using a library of Markov transition matrices," *Solar Energy*, vol. 40, no. 3, pp. 269–279, 1988.

[6] R. Aguiar and M. Collares-Pereira, "TAG: a time-dependent, autoregressive, Gaussian model for generating synthetic hourly radiation," *Solar Energy*, vol. 49, no. 3, pp. 167–174, 1992.

[7] A. Skartveit and J. A. Olseth, "The probability density and autocorrelation of short-term global and beam irradiance," *Solar Energy*, vol. 49, no. 6, pp. 477–487, 1992.

[8] C. A. Glasbey, "Non-linear autoregressive time series with multivariate Gaussian mixtures as marginal distributions," *Journal of the Royal Statistical Society, Series C: Applied Statistics*, vol. 50, no. 2, pp. 143–154, 2001.

[9] A. Voskrebenzev, S. Riechelmann, A. Bais, H. Slaper, and G. Seckmeyer, "Estimating probability distributions of solar irradiance," *Theoretical and Applied Climatology*, 2014.

[10] H. F. Assunção, J. F. Escobedo, and A. P. Oliveira, "Modelling frequency distributions of 5 minute-averaged solar radiation indexes using Beta probability functions," *Theoretical and Applied Climatology*, vol. 75, no. 3-4, pp. 213–224, 2003.

[11] J. Tovar, F. J. Olmo, F. J. Batlles, and L. Alados-Arboledas, "Dependence of one-minute global irradiance probability density distributions on hourly irradiation," *Energy*, vol. 26, no. 7, pp. 659–668, 2001.

[12] Markov, "Rasprostranenie zakona bol'shih chisel na velichiny, zavisyaschie drug ot druga," *Izvestiya Fiziko-Matematicheskogo Obschestva pri Kazanskom Universitete, Seriya 2*, vol. 15, pp. 135–156, 1906.

[13] R. A. Howard, *Dynamic Probabilistic Systems*, vol. 1, John Wiley & Sons, New York, NY, USA, 1971.

[14] D. A. McCracken, *Synthetic high resolution solar data [M.S. thesis]*, Department of Mechanical Engineering, University of Strathclyde, 2011.

[15] G. Bourges, "Reconstitution des courbes de fréquence cumulées de l'irradiation solaire globale horaire reçue par une surface plane," Report CEE 295-77, ESF of Centre d'Energétique de l'Ecole Nationale Supérieure des Mines de Paris, tome II, Paris, France, 1979.

[16] E. L. Maxwell, "A quasi-physical model for converting hourly global horizontal to direct normal insolation," Tech. Rep. SERI/TR-215-3087, Solar Energy Institute, Golden, Colo, USA, 1987.

[17] I. Reda and A. Andreas, "Solar position algorithm for solar radiation applications," *Solar Energy*, vol. 76, no. 5, pp. 577–589, 2004.

[18] J. S. Stein, C. W. Hansen, A. Ellis, and V. Chadliev, "Estimating annual synchronized 1-min power output profiles from utility-scale PV plants at 10 locations in Nevada for a solar grid integration study," in *Proceedings of the 26th European Photovoltaic Solar Energy Conference and Exhibition*, pp. 3874–3880, 2011.

[19] W. Köppen, "Klassifikation der Klimate nach Temperatur, Niederschlag und jahreslauf," *Petermanns Geographische Mitteilungen*, vol. 64, pp. 193–203, 243–248, 1918.

[20] F. Rubel and M. Kottek, "Observed and projected climate shifts 1901–2100 depicted by world maps of the Köppen-Geiger climate classification," *Meteorologische Zeitschrift*, vol. 19, no. 2, pp. 135–141, 2010.

Submit your manuscripts at
http://www.hindawi.com
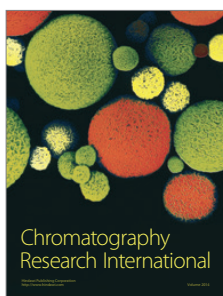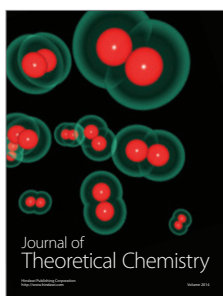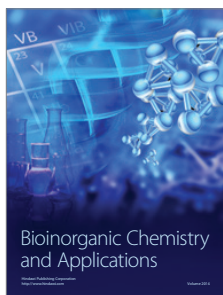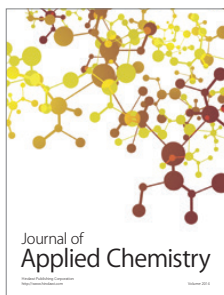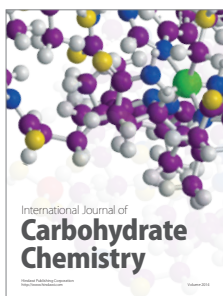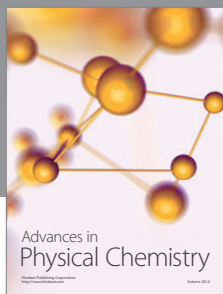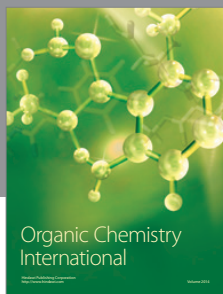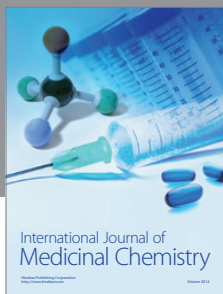
4.2 Research Article B: Comparison of Modelled and Measured Tilted Solar Irradiance for Photovoltaic Applications

4.2.1 Declaration of my contribution

The author of this thesis analyzed the data and performed the calculation used in this study. He also conceived and designed the study and wrote the draft paper. Martin Hofmann, Stefan Riechelmann, and Gunther Seckmeyer contributed to the conception and design, analysis, and interpretation of the data. All authors contributed substantially with comments and revised the manuscript. The quality of the article was further increased by the valuable remarks of the three anonymous reviewers of the article.

4.2.2 Published article

energies

MDPI

Article

Comparison of Modelled and Measured Tilted Solar Irradiance for Photovoltaic Applications

Riyad Mubarak [1,*], Martin Hofmann [1,2] (iD) **, Stefan Riechelmann [3] and Gunther Seckmeyer [1]** (iD)

[1] Institute for Meteorology and Climatology, Leibniz Universität Hannover, Herrenhäuser Straße 2, 30419 Hannover, Germany; martin.hofmann@valentin-software.com (M.H.); Seckmeyer@muk.uni-hannover.de (G.S.)

[2] Valentin Software GmbH, Stralauer Platz 34, 10243 Berlin, Germany

[3] Physikalisch-Technische Bundesanstalt (PTB), Bundesallee 100, 38116 Braunschweig, Germany; stefan.riechelmann@ptb.de

[*] Correspondence: mubarak@muk.uni-hannover.de

Abstract: This work assesses the performance of five transposition models that estimate the global and diffuse solar irradiance on tilted planes based on the global horizontal irradiance. The modelled tilted irradiance values are compared to measured one-minute values from pyranometers and silicon sensors tilted at different angles at Hannover (Germany) and NREL (Golden, CO, USA). It can be recognized that the deviations of the model of Liu and Jordan, Klucher and Perez from the measurements increases as the tilt angle increases and as the sensors are oriented away from the south direction, where they receive lower direct radiation than south-oriented surfaces. Accordingly, the vertical E, W and N planes show the highest deviation. Best results are found by the models from Hay and Davies and Reindl, when horizontal pyranometer measurements and a constant albedo value of 0.2 are used. The relative root mean squared difference (rRMSD) of the anisotropic models does not exceed 11% for south orientation and low inclination angles (β = 10–60°), but reaches up to 28.9% at vertical planes. For sunny locations such as Golden, the Perez model provides the best estimates of global tilted irradiance for south-facing surfaces. The relative mean absolute difference (rMAD) of the Perez model at NREL ranges from 4.2% for 40° tilt to 8.7% for 90° tilt angle, when horizontal pyranometer measurements and a measured albedo value are used; the use of measured albedo values instead of a constant value of 0.2 leads to a reduction of the deviation to 3.9% and 6.0%, respectively. The use of higher albedo values leads to a significant increase of rMAD. We also investigated the uncertainty resulting from using horizontal pyranometer measurements, in combination with constant albedo values, to estimate the incident irradiance on tilted photovoltaic (PV) modules. We found that these uncertainties are small or negligible.

Keywords: incident solar radiation; transposition models; isotropic models; anisotropic models; tilted surface

1. Introduction

To estimate the expected energy output of a PV system, yield estimation models are used which need specific input parameters such as global solar irradiance. Since small uncertainties in the model parameters can lead to large deviations from the expected returns on investment, uncertainties resulting from model input should be reduced as much as possible.

Estimating solar irradiation incident on tilted surfaces of various orientations is essential to estimate the electric power generated by PV, to design solar energy systems and to evaluate their long-term average performance [1]. However, the available measurement data are suboptimal, since global horizontal or diffuse horizontal irradiance measurements provided by pyranometers are often

2 of 18

the only available measurements at most locations. Even if tilted measurements are performed, the tilt angle chosen for the measurement is not necessarily the optimal tilt angle for the location. Consequently, the tilted solar irradiance must be determined by converting the solar irradiance on a horizontal surface to that incident on the tilted surface of interest [2].

Transposition models based on global and diffuse horizontal irradiance have been widely used in the solar energy industry to estimate the solar irradiance incident on tilted PV panels. The transposition models parametrize the irradiance on a tilted plane to three components: direct, diffuse and ground reflected radiation. The direct radiation can be computed by the geometrical relationship between the horizontal and tilted surfaces. The ground reflected radiation can be estimated with the aid of an isotropic model by using simple algorithms. The assumption of isotropy may be justified for estimating the influence of the albedo but is problematic for the diffuse component. This is due to the complexity of the angular dependence of the diffuse component, which depends on many factors such as solar zenith angle and clouds [3]. The continuing evolution and diversity of transposition models illustrates the complexity of the task.

Early models converted the horizontal diffuse radiation to the tilted plane by assuming that the total sky diffuse radiation is distributed isotropically over the sky dome [4–6]. However, this assumption is too simple and is inconsistent with reality. Newer transposition models treat the diffuse component as anisotropically distributed. Several anisotropic models only consider an isotropic background and an additional circumsolar region; others also take the horizon-brightening into account. However, this assumption is only valid in the absence of clouds as in overcast situations the horizon tends to be darker than the zenith [7].

Many authors have studied the accuracy of transposition models by comparing the modelled irradiance with measured values in different climate conditions. Kambezidis et al. [8] used twelve sky diffuse models to calculate the global irradiance on a south-facing surface tilted at 50° in Athens, Greece. Furthermore, four albedo models were used to assess the albedo of the measurement location. The performance of models was evaluated against hourly measurements of global solar irradiance. The transposition models proposed by Gueymard [9], Hay [10], Reindl [11], and Skartveit and Olseth [12] were found to have the best overall performances, in conjunction with either one of three albedo sub-models.

Notton et al. [13] evaluated the performance of 15 transposition models against measured hourly data for two tilted surface angles (45° and 60°) in Ajaccio, France. Among the tested models, the Perez model shows the best accuracy. The authors chose a constant value of 0.2 for the albedo as the most commonly used value in the literature for visible radiation. Gueymard et al. [14] have shown that the deviation between measured and modelled irradiance depends on the uncertainty of the global horizontal irradiance, ground albedo and other factors. Gueymard [15] compared ten transposition models that were appraised against one-minute global irradiance measured on fixed-tilt, south-facing planes (40° and 90°) and a two-axis tracker at NREL's Solar Radiation Research Lab. in Golden (CO, USA). They found that the Gueymard and Perez models provide the best estimates of global irradiance incident on tilted surfaces for sunny sites only when optimal input data (measured direct, diffuse and albedo) are used. When only global irradiance is known, the accuracy of the predicted tilted irradiance degrades significantly. Yang [16] compared the performance of 26 transposition models using 18 case studies from four sites in the USA, Germany and Singapore. Various error metrics, linear ranking, and hypothesis testing were employed to quantify the model performance. Results of the pairwise Diebold-Mariano tests concluded that no single model was universally optimal. However, he found that according to the linear ranking results on rRMSE the top four families of models are Perez, Muneer, Hay, and Gueymard.

Furthermore, there are several studies that have concentrated on the solar radiation on vertical surfaces for building application. Li et al. [17], Cucomo et al. [18], and Chirarattananon et al. [19] evaluated various models to estimate the global solar radiation on vertical surfaces. These studies have indicated that the Perez model delivers better predictions for all orientations. Loutzenhiser et al. [20]

assessed seven radiation models on inclined surfaces that were implemented in building energy simulation codes. Among the models tested in this study are the models of Hay [10] and Perez [21]. These studies revealed that even in the same region, the uncertainties of the solar radiation model were found to vary according to the direction and slope of the surface. Many other studies [22–26] have been conducted in the last two decades to evaluate transposition models and the results show that the performance of models varies, depending on the quality of the input data, the surface orientation and the measurement location.

However, no significant research has been found on how the model sensitivity is affected by using horizontal pyranometer irradiance to estimate the irradiance incident on tilted PV modules, which have different spectral and angular responses, and non-negligible temperature responses. There are also little published research about the systematic error that can be introduced.

In this study, five irradiance transposition models [4,10,11,21,27] are used to calculate the irradiance received on tilted surfaces with various tilt elevation and azimuth angles. We examined model performance for seven south-facing PV surfaces tilted at 10° intervals from 10° to 70°, six vertical tilted surfaces facing north, east, southeast, south, southwest, and west and a horizontally oriented surface. The models were chosen because they are widely used and their required input data are readily available. The validation is conducted with measurement data derived from tilted irradiance sensors, located at two different locations to derive results that hold a more general significance and are more spatially applicable. Furthermore, we investigate the uncertainties caused by the use of horizontal pyranometer measurements to compute the irradiance absorbed by the tilted PV array and the uncertainty from the use of constant albedo value in the calculations.

2. Instruments and Methods

The input data used in this study are one-minute irradiance data measured in two independent locations.

2.1. IMUK Measurements

Various irradiance measurements were performed for three years (January 2014–December 2016) on the roof of the Institute for Meteorology and Climatology (IMUK) of the Leibniz Universität Hannover (Hannover, Germany; 52.23° N, 09.42° E and 50 m above sea level).

The following irradiance measurements were conducted:

1. Global Horizontal Irradiance (GHI) from January 2014 to December 2016, measured by a CMP11 pyranometer (Kipp & Zonen, Delft, The Netherlands),
2. Diffuse Horizontal Irradiance (DHI) from January 2014 to December 2016, measured by a CMP11 pyranometer with a shadow ball (Figure 1a),
3. Global Tilted Irradiance (GTI) measured at a 40° inclined plane facing south by a CM11 pyranometer from January to December 2016,
4. Global Tilted Irradiances from January 2014 to December 2016 measured by at various orientations by 14 crystalline silicon PV device with individual temperature sensors (Mencke & Tegtmeyer GmbH, Hameln, Germany). Seven of those silicon sensors (SiS) were facing south, tilted at 0°, 10°, 20°, 30°, 40°, 50°, 60°, 70°, six sensors were tilted vertically facing N, S, E, W, SE and SW and a single sensor was oriented horizontally (Figure 1b).

All sensors are cleaned regularly to prevent the accumulation of dirt and dust. The silicon sensors have been calibrated by the manufacturer in November 2013. In addition, all SiS's at IMUK are compared after one year of measurements by placing them side by side horizontally. These comparisons were performed under different weather conditions and have showed an agreement within ±3%.

Figure 1. (**a**) Pyranometers and other instruments available and operational at Institute for Meteorology and Climatology (IMUK); (**b**) Set of solar sensors based on silicon detectors mounted in several different tilt angles and orientations, operational at the IMUK (IMUK 2017).

2.2. NREL Measurements

The NREL irradiance measurements were acquired at NREL's Solar Radiation Research Laboratory in Golden, CO, USA (latitude 39.74° N, longitude 105.18° W, elevation 1829 m). This NREL site is located on a mesa that overlooks the western side of the urban agglomeration of Denver. The data have been obtained from SRRL's download tool, http://www.nrel.gov/midc/srrl_bms for the period from March 2015 to December 2016. The NREL data includes the following values:

1. Global Horizontal Irradiance (GHI) measured by a CMP11 pyranometer,
2. Diffuse Horizontal Irradiance (DHI), measured by a CMP11 pyranometer,
3. Global Tilted Irradiance (GTI) measured at a 40° inclined plane facing south by a CMP11 pyranometer,
4. Global Tilted Irradiances measured by a silicon pyranometer LI-200 (LI-COR Inc., Lincoln, NE, USA), facing S, tilted at 40° and vertically tilted sensors facing N, S, E and W,
5. Albedo measurements, measured by two silicon pyranometers LI-200.

2.3. Preprocessing and Quality Control

The following quality control procedure was applied to the IMUK data: Using Equation (1) we corrected the irradiance measured with the SiS's at IMUK based on their temperature coefficient to take in account the drop of sensor signal due to temperature and to correct the testing conditions:

$$I = U_{sen} \times 1000 / U_{cal} / (1 + \alpha \times (T - 25\,°C)), \tag{1}$$

where I is the corrected solar irradiance, U_{sen} is the signal in (mV), U_{cal} is the calibrated value in mV/(1000 W/m^2), T is the sensor temperature, and α represents the temperature coefficient.

In addition to the temperature correction, the cosine error of the silicon sensors is determined and the optical reflectance losses were corrected by using the model of Martin and Ruiz [28]. Only GHI and DHI values recorded at solar zenith angles (SZA) less 85° were used. All GHI and DHI values less than 0 W/m^2 were removed from the analysis, since these values were likely erroneous measurements. Furthermore, any DHI measurement that exceeded the concurrent GHI measurement was set equal to the GHI measurement because it is not physically possible for DHI to exceed GHI [29]. NREL radiation values have been processed with the SERI-QC quality control software developed by NREL. SERI QC assesses the quality of solar radiation data by comparing measured values with expected values. This procedure is based on the relationship between global and direct solar radiation [30].

2.4. Transposition Models

The global tilted irradiance I_T is estimated by the sum of the beam tilted $I_{t,b}$, sky diffuse tilted $I_{t,d}$, and ground-reflected I_g irradiances:

$$I_T = I_{t,b} + I_{t,d} + I_g \tag{2}$$

Five models are selected in this study to estimate the global and diffuse solar irradiance on tilted planes based on the global and diffuse horizontal irradiance. The models are from Liu and Jordan, Klucher, Hay and Davies, Reindl and Perez. Those models have been selected since they are widely used, the necessary input data are available at the examined measurement site, and because they present the three most common model types: isotropic, anisotropic with two components and anisotropic with three components. A brief description of the selected models is given below.

2.4.1. Liu and Jordan Model

The Liu and Jordan model [4] is a simple model that assumes all diffuse sky radiation is uniform over the sky dome and that reflection on the ground is diffuse. For surfaces tilted by an angle β from the horizontal plane, total solar irradiance can be written as:

$$I_T = I_{h,b}R_b + I_{h,d}\left(\frac{1 + \cos\,\beta}{2}\right) + I_h\rho\left(\frac{1 - \cos\,\beta}{2}\right) \tag{3}$$

where I_T is the tilted irradiance, $I_{h,b}$ the beam irradiance on a horizontal surface, R_b the ratio of beam radiation on the tilted surface to that on a horizontal, $I_{h,d}$ the diffuse horizontal irradiance, β the tilt angle, I_h the global horizontal irradiance, and ρ the ground reflectance.

2.4.2. Klucher Model

Klucher found that Liu and Jordan's isotropic model gave good results only for overcast skies. However, it underestimates the irradiance under clear and partly overcast conditions, when there is increased intensity near the horizon and in the circumsolar region of the sky [27]. He developed therefore an anisotropic model by modifying the isotropic model, to take into account the horizontal and circumsolar brightening:

$$I_T = I_{h,b}R_b + I_{h,d}\left(\frac{1 + \cos\,\beta}{2}\right)\left[1 + F\sin^3\left(\frac{\beta}{2}\right)\right] \times \left[1 + F\cos^2\theta\sin^3\theta_z\right] + I_h\rho\left(\frac{1 - \cos\,\beta}{2}\right) \tag{4}$$

$$F = 1 - \left(\frac{I_{h,d}}{I_h}\right)^2 \tag{5}$$

F is the Klucher modulating factor. Under overcast skies, F becomes zero and the model reduces to the Liu & Jordan model.

2.4.3. Hay and Davies Model

The Hay and Davies diffuse model divides the sky diffuse irradiance into isotropic and circumsolar components only [31]. The horizon brightening was not taken into account:

$$I_T = (I_{h,b} + I_{h,d}A)R_b + I_{h,d}(1 - A)\left(\frac{1 + \cos\,\beta}{2}\right) + I_h\rho\left(\frac{1 - \cos\,\beta}{2}\right) \tag{6}$$

$$A = \frac{I_{bn}}{I_{on}} \tag{7}$$

A represents the transmittance of beam irradiance through the atmosphere, where I_{bn} is the direct-normal solar irradiance and I_{on} the direct extraterrestrial normal irradiance.

2.4.4. Reindl Model

The Reindl sky diffuse irradiance model represents three components of diffuse irradiance, including isotropic background, circumsolar brightening, and horizon brightening [11]:

$$I_T = (I_{h,b} + I_{h,d}A)R_b + I_{h,d}(1 - A)(\frac{1 + \cos \beta}{2}) \times [1 + \sqrt{\frac{I_{h,b}}{I_h}} \sin^3(\frac{\beta}{2})] + I_h\rho(\frac{1 - \cos \beta}{2}) \qquad (8)$$

A is the transmittance of beam radiation through the atmosphere defined in Equation (6).

2.4.5. Perez Model

Perez model represents a more detailed analysis of the sky diffuse radiation. The model, like the Klucher and the Reindl models, devided the diffuseirradiance into three components of isotropic background, circumsolar brightening and horizon brightening [21]:

$$I_T = I_{h,b}R_b + I_{h,d}[(1 - F_1)(\frac{1 + \cos \beta}{2}) + F_1\frac{a}{b} + F_2 \sin \beta] + I_h\rho(\frac{1 - \cos \beta}{2}) \qquad (9)$$

where, F_1 and F_2 are circumsolar and horizon brightness coefficients, respectively; a and b are solid angles corresponding to the circumsolar part as seen from the inclined plane. The terms a and b are computed as:

$$a = \max(0, \cos \theta) \qquad (10)$$

$$b = \max(\cos 85°, \cos \theta_z) \qquad (11)$$

F_1 and F_2 in Equation (9) are functions of clearness ε, zenith angle θ_z and brightness Δ. These factors are defined as:

$$\varepsilon = \frac{\frac{I_{h,d}+I_{bn}}{I_{h,d}} + 5.535 \times 10^{-6}\, \theta_z{}^3}{1 + 5.535 \times 10^{-6}\, \theta_z{}^3} \qquad (12)$$

$$\Delta = m\frac{I_{h,d}}{I_{on}} \qquad (13)$$

The coefficients F_1 and F_2 are then computed as:

$$F_1 = \max[0, (f_{11} + f_{12}\Delta + \frac{\pi\theta_z}{180}f_{13})] \qquad (14)$$

$$F_2 = f_{21} + f_{22}\Delta + \frac{\pi\theta_z}{180}f_{23} \qquad (15)$$

The coefficients f_{11}, f_{12}, f_{13}, f_{21}, f_{22} and f_{23} were derived based on a statistical analysis of experimental data for different locations (Table 1).

Table 1. Perez model coefficients for various values of clearness ε.

ε	f_{11}	f_{12}	f_{13}	f_{21}	f_{22}	f_{23}
[1, 1.065]	−0.008	0.588	−0.062	−0.06	0.072	−0.022
[1.065, 1.23]	0.13	0.683	−0.151	−0.019	0.066	−0.029
[1.23, 1.5]	0.33	0.487	−0.221	0.055	−0.064	−0.026
[1.5, 1.95]	0.568	0.187	−0.295	0.109	−0.152	−0.014
[1.95, 2.8]	0.873	−0.392	−0.362	0.226	−0.462	0.001
[2.8, 4.5]	1.132	−1.237	−0.412	0.288	−0.823	0.056
[4.5, 6.2]	1.06	−1.6	−0.359	0.264	−1.127	0.131
[6.2, ∞]	0.678	−0.327	−0.25	0.156	−1.377	0.251

The ability of models to estimate the solar irradiance incident on tilted surfaces is analyzed by means of the relative Root Mean Square Difference (rRMSD), relative Mean Absolute Difference (rMAD) and relative Mean Bias Difference (rMBD). These parameters are calculated using Equations (16)–(21):

$$RMSD = \sqrt{\frac{\sum (Mi - Ci)^2}{n}} \tag{16}$$

$$rRMSD = \frac{RMSD}{\bar{\bar{M}}} 100\% \tag{17}$$

$$MAD = \frac{\sum |(Mi - Ci)|}{n} \tag{18}$$

$$rMAD = \frac{MBD}{\bar{\bar{M}}} 100\% \tag{19}$$

$$MBD = \frac{\sum (Mi - Ci)}{n} \tag{20}$$

$$rMBD = \frac{MBD}{\bar{\bar{M}}} 100\% \tag{21}$$

where *Mi* is the measured irradiance on an inclined plane and *Ci* the calculated model value.

3. Results and Discussion

3.1. Measurement Validation

The two most devices used by the PV industry for measuring the solar irradiance are thermopile pyranometers and small solar cells (silicon sensors). Of the latter, only crystalline silicon (cSi) sensors provide the required stability [32].

Thermopile pyranometers are devices that consist of junctions of dissimilar metals in contact with a black surface that absorbs solar radiation (the "hot" junction) and a separate surface that does not absorb solar radiation (the "cold" junction). Pyranometers have an uniform spectral response from about 280 to about 2800 nm. They are widely used for meteorological measurements and nearly all existing irradiation databases are validated using these measurements [32].

Unlike pyranometers, silicon sensors convert incident irradiance to electrons through the photovoltaic effect. The silicon sensors are spectrally selective in the range of about 350 to about 1100 nm (Figure 2). The shorter wavelength is determined by the transmission of the front glass and encapsulant, whereas the longer wavelength is determined by the material's band gap [33]. Table 2 provides a comparison of basic specifications between the sensors used in this study.

Table 2. Comparison of the specifications of the sensors used.

Specifications	Pyranometer CMP11	Silicon Sensor SiS	Silicon Sensor Li-200
Spectral sensitivity range (nm)	285–2800	350–1100	350–1100
Response time (s)	5	<0.001	<0.001
Offset (W/m^2)	2	0	0
Temperature dependence (-10–$40\,^\circ$C) (%)	<1	0.2	±0.15
Uncertainty (W/m^2)	<5	± 5	<5
Non-linearity (100 to 1000 W/m^2) (%)	<0.5	±0.5	<1.0

Due to the different spectral response the highest absolute difference between the signal measured by a silicon sensor and a thermopile pyranometer is at clear sky conditions with a low diffuse to direct ratio [34]. Silicon sensors are fundamentally photovoltaic devices, and as such, standard American Society for Testing and Materials (ASTM) test procedures are applied to calibrate them by using a solar simulator [35].

The difference in cosine error is considered as the second important factor that sets apart the two devices. Silicon sensors have in general a higher cosine error than thermopile pyranometers [36] and therefore underestimate radiance incident from steep angles.

The difference between the sensors (see Table 2) affects the measured irradiance, as shown in Figure 3. The sensitivity of silicon sensors shows an increase during summer months, when SZAs are low compared to the winter months. The ratio of measured irradiance between the pyranometers and silicon the sensors is higher in winter. The right plots of Figure 3 show the ratios of daily horizontal irradiance measured by both sensors. The annual pyranometer irradiance at both sites is higher than the irradiance derived by the silicon sensors. At NREL, the pyranometer irradiance is higher in winter months, while irradiance measured by the Li-200 sensor is higher in summer. However, the behavior of silicon sensors against pyranometer measurements in both locations is the same, the relative sensitivity of the silicon sensors increases during the summer months.
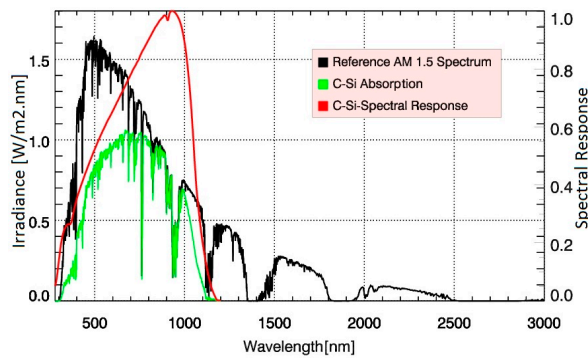
Figure 2. Global solar spectrum at air mass 1.5 (black) and the portion absorbed by a silicon device (green). The silicon sensors (SiS) can measure up to 1200 nm (compare the c-Si spectral response (red)), while the pyranometer measures up to about 2800 nm.
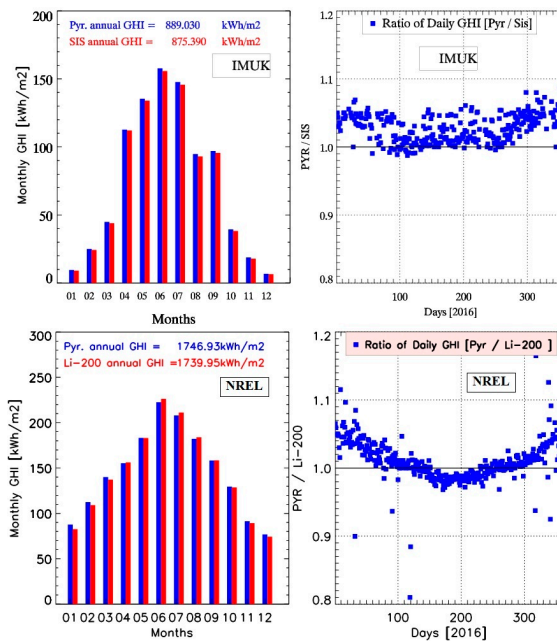
Figure 3. [**Top plots**] Monthly global horizontal irradiance (GHI) measured by thermopile pyranometers and silicon sensors (SiS) on horizontal surface (**left**) and the ratios of daily irradiances measured by both sensors (**right**), for the location of IMuK. [**Bottom plots**] the same as the top plots but at NREL. The irradiance measured by silicon sensors shows an increase during the summer months.

In the following we investigate the uncertainties associated with the use of different irradiance sensors and assumption of albedo values as the major contributors to the uncertainty.

3.1.1. Uncertainty Resulting from Using Different Sensors

Low uncertainty of the measurements is a key factor for the quality of the data. For many applications, including predictions for a return of investment, it is important to know the uncertainties resulting from using sensors of various types to measure horizontal and tilted irradiance.

In this regard, it makes sense to use the statistical indices to compare the horizontal measurements from different technologies of solar sensors. Figure 4 shows the monthly and the annual rRMSD, rMBD and rMAD between the horizontal irradiances measured by the pyranometer and the silicon sensors at both sites in 2016. The annual rRMSD and the rMBD values at IMUK are 5.2% and 3.5% respectively. The differences are largest in the winter months, as the measured signal is low and are slightly lower with increasing irradiance in the summer months. The differences between the NREL's sensors are smaller, where the annual rRMSD is 3.6% and the rMBD is 1.1%. The monthly average in the left plot shows the same behavior at NREL with negative rMBD values during the summer months (June–September). This agrees with Figure 3, where irradiance measured by the Li-200 sensor is higher in summer than the pyranometer values.
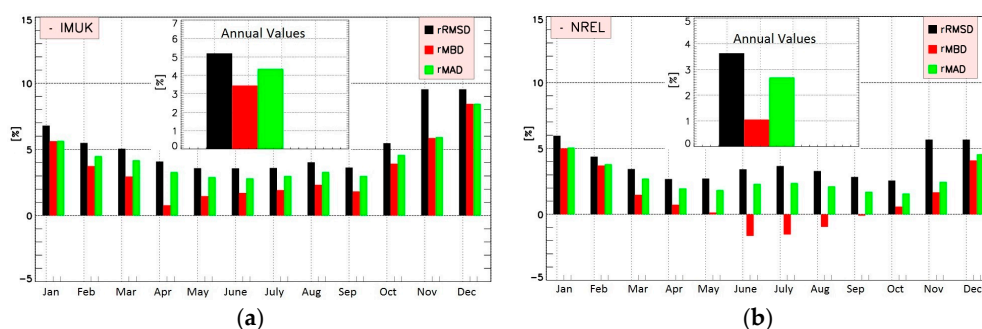

Figure 4. Monthly and annual average of the statistical indices relative Root Mean Square Difference (rRMSD), relative Mean Absolute Difference (rMBD) and relative Mean Bias Difference (rMAD) between pyranometer and silicon sensor measurements at IMUK (**a**) and at NREL (**b**). The statistical indices show clear differences in the magnitude and show a seasonal dependence.

Based on these results, it is important to investigate how the differences in the horizontal measurements of different sensors affect the calculated tilted irradiance.

For this purpose, horizontal pyranometer measurements from 2016 were used to calculate the tilted irradiance at 40° S. The results were compared with tilted irradiance measured by: (1) tilted thermopile pyranometer and (2) tilted silicon sensor (SIS) at 40° S. The rMAD resulting from the comparison with SIS values ranges from 5.1 (Reindl) to 8.4% (Liu and Jordan). The comparison with Pyranometer values leads to slightly lower differences of 5.1% and 6.5%, respectively (Figure 5). The Liu and Jordan model and the Perez model are affected more when using different instruments whereas the model of Hay and Davies and Reindl were almost unaffected. These values are for 40° S tilt, the other orientations could not be tested, because there is only one tilted pyranometer (40° S) at IMUK.

Thus, it can be concluded, that a systematic error is introduced when using horizontal pyranometer measurements to compute the irradiance absorbed by tilted PV modules, which have different spectral, angular, and temperature responses. Depending on the used model, this error has only a small or even no influence on the calculated irradiance on a tilted PV surface.
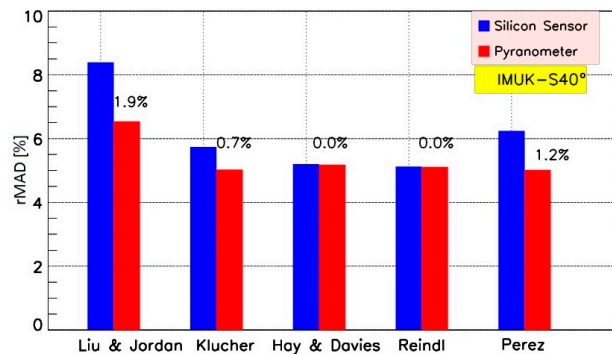
Figure 5. Dependence of the rMAD on the used sensor for the five transposition models. The performance of models is better if the model input data (GHI) and validation data (GTI) are measured by sensors of the same type.

3.1.2. Albedo and Seasonal Effects

The accuracy of ground reflection calculations depends strongly on the knowledge of albedo values used in the models; the dependence becomes stronger as the tilt angle increases [15]. Only in rare cases ground is albedo is known accurately; in most cases a constant value for albedo is used by the model.

It is useful to evaluate the uncertainty that results from using a spectrally constant albedo for calculating the tilted irradiance. For this purpose, measured albedo values and different constant values (0.2, 0.4, 0.6 and 0.9) are used to calculate the tilted irradiance on 40° and 90° tilt based on NREL data. The rMAD is used to evaluate the prediction of the models for each albedo value (Figure 6).
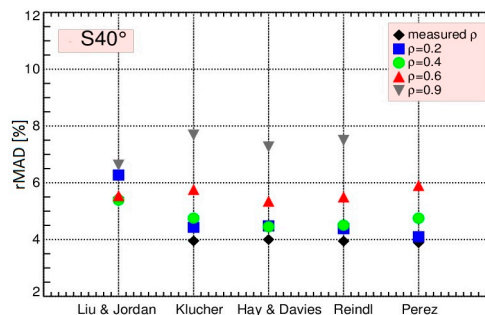
Figure 6. Dependence of the rMAD for the five models on the spectrally constant ground albedo. The tilted irradiance has been calculated based on NREL data for 40° S tilt, using different constant albedo values (0.2, 0.4, 0.6 and 0.9) and measured values at NREL. The models show lower deviations to the measurement if measured albedo values are used.

Figure 6 shows that the models are more accurate if measured albedo values are used. The rMAD increase as the albedo value increases. The use of constant albedo value of 0.2 (the most used value for models) leads to an increase of the rMAD of between 0.2% (Perez) and 0.8% (Liu and Jordan). The Figure 6 also shows that the Liu and Jordan model is less dependent on the albedo. This may be explained by the assumption of isotropic distribution of diffuse irradiance in this model.

The same calculations were done for 90° S tilt (Figure 7). It is easy to recognize that the influence of albedo on the calculated tilt irradiance is much larger. The use of a constant value of 0.2 instead of a measured value increases the rMAD by about 2.5% (Perez model) and 3.8% (Liu and Jordan). The rMAD increases also with increasing albedo values.

Figure 7. Same as Figure 6, but for 90° S. The rMAD increase as the albedo value increases. The plot illustrates albedo values on vertical tilted irradiance.

3.2. Model Validation

In order to evaluate the model performance and to consider the influence of some input parameters on the results, we use measured horizontal irradiances (global and diffuse) to calculate the tilted 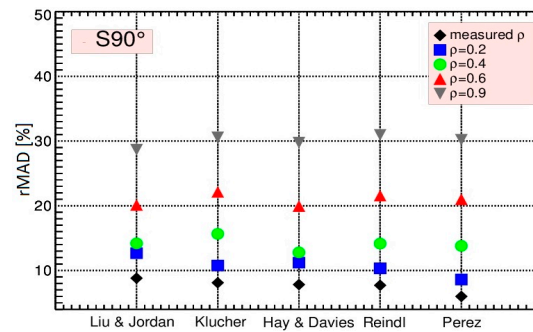irradiance at different orientations and tilt angles. The calculated values are compared with one-minute values from irradiance sensors facing the same orientation and tilt angles. The global and diffuse horizontal input values are measured at both sites by thermopile pyranometers. Furthermore, tilted pyranometers are used to measure the tilted global irradiance at 40°. Tilted irradiance at IMUK has been measured by silicon sensors (SiS) at 14 different orientations and tilt angles. At NREL, the tilted irradiance at 40° and at different vertical planes (E, W, S, N) were measured by another silicon device (Li-200). The measurements and the corresponding instruments are shown in details in Table 3.

Table 3. Components and data used for comparisons between measurements and models.

Measurements			Model			
Parameter	Description	Measuring Sensor	Parameter	Description	Inputs	Measuring Sensor
GTI south facing (IMUK)	Tilt: 10°, 20°, 30°, 40°, 50°, 60°, 70°	SiS	GTI south facing	Tilt: 10°, 20°, 30°, 40°, 50°, 60°, 70°	GHI DHI Albedo	CMP11 CMP11 Const. 0.2
GTI Vertical (IMUK)	E, S, W, N, SE, SW	SiS	GTI Vertical	E, S, W, N, SE, SW	GHI DHI Albedo	CMP11 CMP11 Const. 0.2
GTI south facing (IMUK)	Tilt: 40°	CMP11	GTI south facing	Tilt: 40°	GHI DHI Albedo	CMP11 CMP11 Const. 0.2
GTI south facing (NREL)	Tilt: 40°	Li-200	GTI south facing	Tilt: 40°	GHI DHI Albedo	CMP11 CMP11 Li-200
GTI Vertical (NREL)	E, S, W, N	Li-200	GTI Vertical	E, S, W, N	GHI DHI Albedo	CMP11 CMP11 Li-200
GTI south facing (NREL)	Tilt: 40°	CMP11	GTI south facing	Tilt: 40°	GHI DHI Albedo	CMP11 CMP11 Li-200
GTI south facing (NREL)	Tilt: 40°	Li-200	GTI south facing	Tilt: 40°	GHI DHI Albedo	CMP11 CMP11 Li-200
GTI Vertical (NREL)	S	Li-200	GTI Vertical	S	GHI DHI Albedo	CMP11 CMP11 Li-200

The results of the five models are shown in Table 4, for all available orientations and tilt angles of IMUK. It can be recognized that the deviations of the model of Liu and Jordan, Klucher and Perez from the measurements increases as the tilt angle increases and as the sensors are oriented away from the

south direction, where they receive much less direct radiation than south-facing surfaces. Accordingly, the vertical E, W and N planes show the highest deviation. In general, the best results in terms of rRMSD and rMAD are obtained with the Hay and Davies and Reindl models, while the isotropic model of Liu & Jordan provide the worst agreement for south facing planes (Figure 8).

For the vertical tilt planes, the Hay and Davies model obtains the lowest RMSD. The Klucher transposition model is most affected by errors when facing away from the south direction. The high deviation of the vertical sensors can be related to the significant change in the ratio I_d / I_h for the vertical tilt and also to the incorrect modelling of ground reflection.

It has also been observed that the anisotropic models overestimate the south-tilted irradiances (MBD ranging from -0.52 to -3.63%) and most of the vertical irradiances (MBD ranging from 3.47 to -20.1%). In contrast, the Liu and Jordan model underestimates the tilted irradiance in most directions, but not at very low tilt or on vertical surfaces away from the south quadrant.
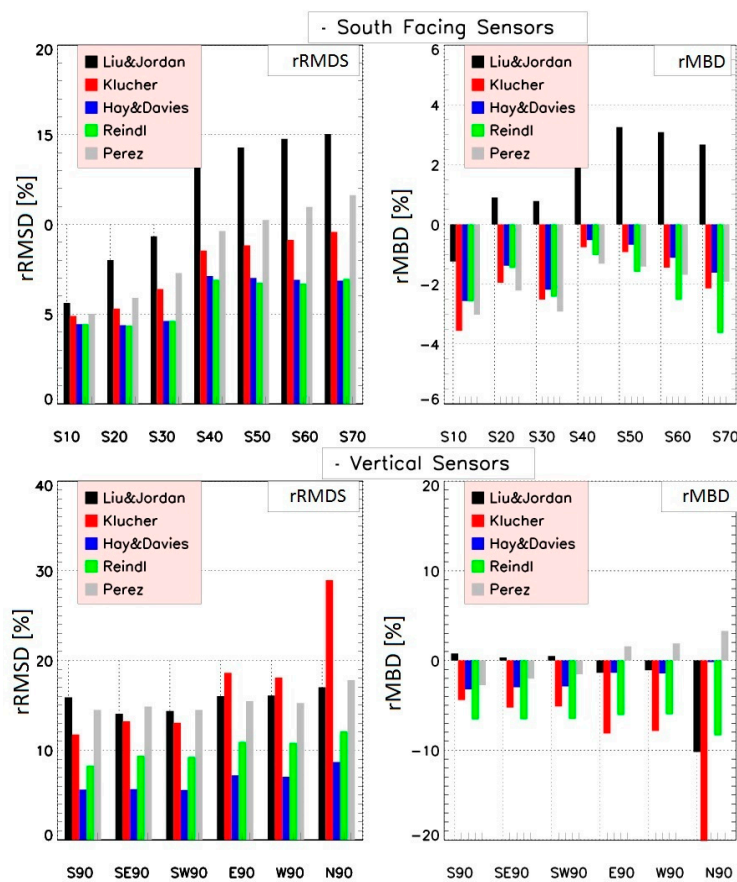
Figure 8. Root mean square difference (**left**) and mean bias difference (**right**) between model and measurements at IMUK for all south facing sensors (upper plots) and vertical sensors (lower plots). The difference increases, as the tilt angle increase.

According to the data from NREL (Table 5), the Perez model provides the best results for S and N directions, while the models of Reindl and Hay and Davies provide the lowest rRMSD for E and W orientations, which agrees with the IMUK results. The rMBD of rNREL values show that the models of Klucher and Perez overestimate the calculated irradiance (MBD ranging from -0.45 to -16.7%), while the rMBDs of the other models range between positive and negative, depending on the azimuth angle (Figure 9).

The difference in model performance between IMUK and NREL can be explained by two factors. First, by the different climates of the sites; the sky at IMUK is mostly cloudy, while NREL is a sunny site; Second, the quality of model input data; the GHI and DHI were measured by different sensors and measured albedo values are used for modelling the NREL data, which influences the calculated vertical irradiance significantly.
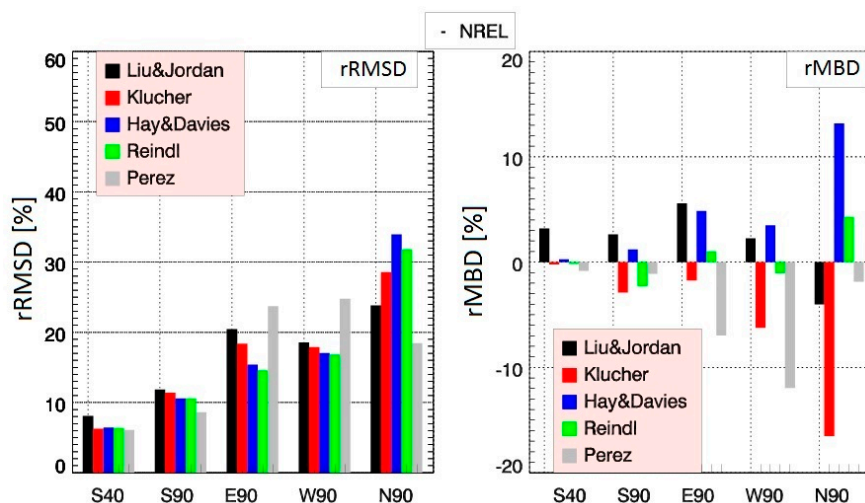

Figure 9. Root mean square difference (**left**) and mean bias difference (**right**) between model and measurements at NREL for all available orientations.

The accuracy of the modelled global tilted irradiance depends basically on two things: the availability of measured irradiance, which is a requirement for any model [14] and the accuracy of the model itself, in other words, the ability of the model to simulate the irradiance distribution in the atmosphere. It is therefore important to evaluate the uncertainty resulting from the input data of the model before evaluating the performance of the models. The measured horizontal irradiance components (global, diffuse, direct) constitute the most important input data to compute the tilted irradiance. Modelling of tilted irradiance would be ideal if measurements for all irradiance components, including ground reflectance, were available. This would avoid uncertainties that result from estimation of one component from the other two. The modelling of tilted irradiance would be less ideal but still useful if two of them are available.

All presented models use the same method for calculating beam and ground reflected irradiance on a tilted surface; the differences lie only in the calculation of the diffuse radiation. The statistical analysis showed that the Reindl and Hay and Davies models produce the best agreement with the measured tilted data in Hannover. The results of both models are very similar, even although they differ in their modeling approach for the diffuse sky radiation. This may be because both models use the same anisotropic index to weight the circumsolar and isotropic components. Moreover, the horizon brightening component has a limited effect under cloudy conditions; it is most profound in clear skies [37].

Table 4. Performance of all five transposition models, compared to IMUK measurements.

IMUK	Liu & Jordan			Klucher			Hay & Davies			Reindl			Perez		
Azimuth/Tilt	rMBD	rMAD	rRMSD	rMBD	rMAD	rRMSD	rMBD	rMAD	rRMSD	rMBD	rMAD	rRMSD	rMBD	rMAD	rRMSD
ss10	−1.24	4.32	5.62	−3.56	4.06	4.98	−2.56	3.67	4.44	−2.57	3.67	4.44	−3.02	3.94	5.01
ss20	0.90	5.61	8.01	−1.95	4.08	5.30	−1.38	3.51	4.38	−1.45	3.51	4.36	−2.21	4.19	5.90
ss30	0.78	6.55	9.33	−2.51	4.95	6.39	−2.18	3.75	4.62	−2.41	3.77	4.61	−2.91	5.08	7.28
ss40	3.03	8.71	13.49	−0.76	6.54	8.54	−0.52	5.11	07.12	−1.02	5.04	06.91	−1.31	6.40	09.62
ss50	3.25	9.11	14.29	−0.92	6.20	08.83	−0.68	5.06	07.02	−1.58	5.01	06.74	−1.41	6.88	10.24
ss60	3.08	9.37	14.76	−1.44	6.46	09.13	−1.11	5.04	06.91	−2.52	5.15	06.70	−1.68	7.41	10.97
ss70	2.57	10.96	15.03	−2.14	6.47	09.58	−1.61	5.05	06.86	−3.63	5.16	06.95	−1.93	8.05	11.63
ss90	0.76	08.04	15.89	−4.41	08.04	11.74	−3.22	04.14	05.60	−6.57	6.70	09.27	−2.75	10.25	14.48
se90	0.32	08.56	14.06	−5.26	08.42	13.20	−2.99	04.00	05.64	−6.55	06.65	09.38	−2.02	10.73	14.85
sw90	0.50	08.70	14.36	−5.12	08.43	13.05	−2.98	03.96	05.55	−6.51	06.60	09.26	−1.54	10.43	14.47
ee90	−1.37	10.29	16.02	−8.14	12.66	18.63	−1.38	05.21	07.20	−6.07	07.69	10.92	1.57	11.36	15.46
ww90	−1.09	10.46	16.10	−7.86	12.50	18.09	−1.43	05.13	07.02	−6.01	07.67	10.80	1.98	11.27	15.24
nn90	−10.20	10.48	17.00	−20.13	20.28	28.94	−0.17	06.81	08.67	−8.34	08.97	12.08	3.47	14.45	17.81
pyr40	4.66	6.64	8.69	0.74	5.03	6.74	1.45	5.68	7.59	1	5.49	7.37	0.23	5.08	6.66

Table 5. Performance of all five transposition models, based on NREL data base.

NREL	Liu & Jordan			Klucher			Hay & Davies			Reindl			Perez		
Azimuth/Tilt	rMBD	rMAD	rRMSD	rMBD	rMAD	rRMSD	rMBD	rMAD	rRMSD	rMBD	rMAD	rRMSD	rMBD	rMAD	rRMSD
S 40	2.89	5.47	7.85	−0.45	3.95	6.08	0.08	4.0	6.26	−0.36	3.94	6.18	−0.96	3.98	6.0
S 90	2.40	8.81	11.76	−3.06	8.11	11.46	1.09	7.82	10.63	−2.41	7.72	10.68	−1.13	5.99	8.72
E 90	5.48	13.87	20.5	−1.75	13.1	18.64	4.70	11.18	15.50	0.91	10.5	14.8	−6.88	17.07	24.02
W 90	2.28	13.58	18.8	−6.1	13.25	18.2	3.50	13.49	17.3	−1.02	13.05	17.1	−11.78	17.75	25.15
N 90	−4.60	18.3	24.10	−16.7	21.00	29.05	12.33	28.20	33.78	3.47	25.85	31.8	−2.65	14.31	18.89

52

As expected, the isotropic Liu and Jordan model underestimates the tilted diffuse irradiance (positive MBD) for the south-facing planes, while it shows relatively good agreement with the measurement for the other orientations, when the irradiance is low. In contrast, the anisotropic models overestimate the irradiance at IMUK, with the three-component anisotropic models tending to overestimate the diffuse irradiance more than the two-component models.

The assumed distributions for diffuse sky irradiance and the nature of the anisotropic factors are what characterizes each of the anisotropic models used in this study. For the models of Klucher and Perez, it is possible that the climate at IMUK has some characteristics that require adjustment of the coefficients used in both model.

It can be concluded that the accurate calculation of the tilted diffuse solar irradiance is what distinguishes models form each other. Moreover, the basic criterion for selecting the most suitable model for simulating the electrical output of a PV module is its ability to simulate the diffuse radiation of the sky under all weather conditions. This can be understood if we consider that an inaccurately calculated diffuse irradiance can lead to significant over- or underestimations in the annual energy yield of a photovoltaic (PV) system by as much as 8% [38] even for horizontal orientations of the PV system.

4. Conclusions

Using one-minute measured GHI and DHI data, modeling was performed to calculate the tilted irradiance for different orientations and tilt angles in Hannover (Germany) and at NREL (Golden, CO, USA). The following conclusions can be drawn from this study:

- Best results are provided by the models from Hay and Davies and Reindl, when horizontal pyranometer measurements and a constant albedo value of 0.2 are used. This agreement of the two may relate to the anisotropic index used by both models to weight the circumsolar and isotropic components.

- The anisotropic models overestimate the south tilted irradiance and most of vertical tilted irradiance. In contrast, the isotropic model underestimates the tilted irradiance in most directions.

- For the NREL location, when measured albedo is used, the Perez model provides the best estimates of global tilted irradiance.

- The deviations of the anisotropic models from the measurements increase with increasing deviation from the south direction. In this case, the ratio of direct to diffuse radiation decreases and the uncertainty in modelling the diffuse irradiance becomes dominant.

- An uncertainty is introduced when using horizontal pyranometer measurements to estimate the irradiance absorbed by tilted PV modules. Depending on the used model, this uncertainty has only a small or even no effect on the calculated irradiance.

- The influence of albedo value on the calculated tilted irradiance increases as the tilt angle increases. The use of a constant albedo value of 0.2, which is widely accepted and used in most applications, leads to an increase in the rMAD that ranges between 0.2% and 0.8% at 40° tilt and reaches up to 3.8% at 90° tilt angle. If there are surfaces with higher reflectance in the vicinity of the PV system, rMAD is significantly higher.

- The models of Hay and Davies and Reindl is recommended to estimate the tilted irradiance for south-facing modules in regions with mainly cloudy conditions and when albedo measurements are not available. The Hay and Davies model would also be useful for vertical surfaces (e.g., facades and glazing) whereas the Perez model is recommended for sunny sites and when albedo measurements are available.

The spectral distribution of sky radiance is affected by clouds and aerosols. This has a significant influence on the performance of silicon sensors, where the spectral response of silicon sensors is wavelength-dependent. Therefore, additional spectral measurements are needed to understand the

behavior of silicon sensors in the different weather conditions. Therefore, advances in the modelling of PV yields require more knowledge about spectral radiance, which is known to be anisotropic.

Author Contributions: Riyad Mubarak conceived and designed the study and wrote the draft paper; Martin Hofmann, Stefan Riechelmann and Gunther Seckmeyer contributed in conception and design, analysis and interpretation of the data. All the authors significantly contributed to the final version of the manuscript.

Conflicts of Interest: The authors declare no conflict of interest.

Nomenclature

Δ	sky's brightness, as in Perez model
ρ	ground albedo
β	tilt angle (rad)
θ	incidence angle (rad)
θ_z	solar zenith angle (rad)
ε	sky's clearness, as in Perez model [21]
a, b	sky geometry parameters, as in Perez model
A	transmittance of beam irradiance through atmosphere, as in Hay & Davies model
c-Si	crystalline silicon
F	Klucher's modulating factor
F_1, F_2	degree of circumsolar and horizon anisotropy, in the simplified Perez model
$f_{11}, f_{12}, f_{13}, f_{21}, f_{22}, f_{23}$	Perez model coefficients for irradiance
I_{bn}	direct-normal solar irradiance (DNI) (W/m^2)
$I_{h,b}$	beam horizontal irradiance (BHI) (W/m^2)
I_h	global horizontal irradiance (GHI) (W/m^2)
$I_{h,d}$	diffuse horizontal irradiance (DHI) (W/m^2)
$I_{t,b}$	beam tilted irradiance (BTI) (W/m^2)
$I_{t,d}$	diffuse tilted irradiance (DTI) (W/m^2)
I_g	ground-reflected irradiance (W/m^2)
I_{on}	direct extraterrestrial normal irradiance (W/m^2)
I_T	global tilted irradiance (GTI) (W/m^2)
MAD	mean absolute difference
MBD	mean bias difference
PV	photovoltaic
α	temperature coefficient
R_b	factor that accounts for direction of beam radiation,
RMSD	root mean square difference
SiS	silicon sensor

References

1. Mehleri, E.D.; Zervas, P.L.; Sarimveis, H.; Palyvos, J.A.; Markatos, N.C. A new neural network model for evaluating the performance of various hourly slope irradiation models: Implementation for the region of Athens. *Renew. Energy* **2010**, *35*, 1357–1362. [CrossRef]
2. Kudish, A.I.; Evseev, E.G. Prediction of solar global radiation on a surface tilted to the south. In Proceedings of the Optical Modeling and Measurements for Solar Energy Systems II, San Diego, CA, USA, 11 September 2008; p. 704603.
3. Riechelmann, S.; Schrempf, M.; Seckmeyer, G. Simultaneous measurement of spectral sky radiance by a non-scanning multidirectional spectroradiometer (MUDIS). *Meas. Sci. Technol.* **2013**, *24*, 125501. [CrossRef]
4. Liu, B.; Jordan, R. Daily insolation on surfaces tilted towards equator. *ASHRAE J.* **1961**, *10*, 526–541.
5. Duffie, J.A.; Beckman, W.A.; Worek, W.M. *Solar Engineering of Thermal Processes*, 2nd ed.; John Wiley & Sons: New York, NY, USA, 1991.

6.   Badescu, V. 3D isotropic approximation for solar diffuse irradiance on tilted surfaces. *Renew. Energy* **2002**, *26*, 221–233. [CrossRef]

7.   Grant, R.H.; Heisler, G.M. Obscured Overcast Sky Radiance Distributions for Ultraviolet and Photosynthetically Active Radiation. *J. Appl. Meteorol.* **1997**, *36*, 1336–1345. [CrossRef]

8.   Kambezidis, H.D.; Psiloglou, B.E.; Gueymard, C. Measurements and models for total solar irradiance on inclined surface in Athens, Greece. *Sol. Energy* **1994**, *53*, 177–185. [CrossRef]

9.   Gueymard, C. An anisotropic solar irradiance model for tilted surfaces and its comparison with selected engineering algorithms. *Sol. Energy* **1987**, *38*, 367–386. [CrossRef]

10. Hay, J.E. Calculation of monthly mean solar radiation for horizontal and inclined surfaces. *Sol. Energy* **1979**, *23*, 301–307. [CrossRef]

11. Reindl, D.T.; Beckman, W.A.; Duffie, J.A. Evaluation of hourly tilted surface radiation models. *Sol. Energy* **1990**, *45*, 9–17. [CrossRef]

12. Skartveit, A.; Asle Olseth, J. Modelling slope irradiance at high latitudes. *Sol. Energy* **1986**, *36*, 333–344. [CrossRef]

13. Notton, G.; Cristofari, C.; Poggi, P. Performance evaluation of various hourly slope irradiation models using Mediterranean experimental data of Ajaccio. *Energy Convers. Manag.* **2006**, *47*, 147–173. [CrossRef]

14. Gueymard, C.A. Advanced solar irradiance model and procedure for spectral solar heat gain calculation. *ASHRAE Trans.* **2007**, *113 Pt 1*, 149–164.

15. Gueymard, D.R.; Myers, C.A. *Validation and Ranking Methodologies for Solar Radiation Models*; Springer: Berlin/Heidelberg, Germany, 2008.

16. Yang, D. Solar radiation on inclined surfaces: Corrections and benchmarks. *Sol. Energy* **2016**, *136*, 288–302. [CrossRef]

17. Li, D.H.W.; Lam, J.C.; Lau, C.C.S. A new approach for predicting vertical global solar irradiance. *Renew. Energy* **2002**, *25*, 591–606. [CrossRef]

18. Cucumo, M.; De Rosa, A.; Ferraro, V.; Kaliakatsos, D.; Marinelli, V. Experimental testing of models for the estimation of hourly solar radiation on vertical surfaces at Arcavacata di Rende. *Sol. Energy* **2007**, *81*, 692–695. [CrossRef]

19. Chirarattananon, S.; Rukkwansuk, P.; Chaiwiwatworakul, P.; Pakdeepol, P. Evaluation of vertical illuminance and irradiance models against data from north Bangkok. *Build. Environ.* **2007**, *42*, 3894–3904. [CrossRef]

20. Loutzenhiser, P.G.; Manz, H.; Felsmann, C.; Strachan, P.A.; Frank, T.; Maxwell, G.M. Empirical validation of models to compute solar irradiance on inclined surfaces for building energy simulation. *Sol. Energy* **2007**, *81*, 254–267. [CrossRef]

21. Perez, R.; Ineichen, P.; Seals, R.; Michalsky, J.; Stewart, R. Modeling daylight availability and irradiance components from direct and global irradiance. *Sol. Energy* **1990**, *44*, 271–289. [CrossRef]

22. De Miguel, A.; Bilbao, J.; Aguiar, R.; Kambezidis, H.; Negro, E. Diffuse solar irradiation model evaluation in the North Mediterranean Belt area. *Sol. Energy* **2001**, *70*, 143–153. [CrossRef]

23. Pandey, C.K.; Katiyar, A.K. A comparative study of solar irradiation models on various inclined surfaces for India. *Appl. Energy* **2011**, *88*, 1455–1459. [CrossRef]

24. Demain, C.; Journée, M.; Bertrand, C. Evaluation of different models to estimate the global solar radiation on inclined surfaces. *Renew. Energy* **2013**, *50*, 710–721. [CrossRef]

25. Khalil, S.A.; Shaffie, A.M. Performance of Statistical Comparison Models of Solar Energy on Horizontal and Inclined Surface. *Int. J. Energy Power* **2013**, *2*, 8–25.

26. Wattan, R.; Janjai, S. An investigation of the performance of 14 models for estimating hourly diffuse irradiation on inclined surfaces at tropical sites. *Renew. Energy* **2016**, *93*, 667–674. [CrossRef]

27. Klucher, T.M. Evaluation of models to predict insolation on tilted surfaces. *Sol. Energy* **1979**, *23*, 111–114. [CrossRef]

28. Martin, N.; Ruiz, J.M. Annual angular reflection losses in PV modules. *Prog. Photovolt. Res. Appl.* **2005**, *13*, 75–84. [CrossRef]

29. Lave, M.; Hayes, W.; Pohl, A.; Hansen, C.W. Evaluation of global horizontal irradiance to plane-of-array irradiance models at locations across the United States. *IEEE J. Photovolt.* **2015**, *5*, 597–606. [CrossRef]

30. Maxwell, E.; Wilcox, S. *Users Manual for SERI QC Software, Assessing the Quality of Solar Radiation Data*; National Renewable Energy Laboratory: Golden, CO, USA, 1993.

31. Hay, J.E.; Davies, J.A. Calculation of the solar radiation incident on an inclined surface. In Proceedings of the First Canadian Solar Radiation Data Workshop, Toronto, ON, Canada, 17–19 April 1978; pp. 59–72.

32. Woyte, A.; Richter, M.; Moser, D.; Mau, S.; Reich, N.; Jahn, U. Monitoring of Photovoltaic Systems: Good Practices and Systematic Analysis. *J. Chem. Inf. Model.* **2013**, *53*, 1689–1699.

33. Woyte, A.; Richter, M.; Moser, D.; Reich, N.; Green, M.; Mau, S.; Beyer, H. *Analytical Monitoring of Grid-Connected Photovoltaic Systems—Good Practices for Monitoring and Performance Analysis*; Technical Report; IEA-PVPS: St. Ursen, Switzerland, 2014.

34. Glotzbach, T.; Schulz, B.; Zehner, M.; Fritze, P.; Schlatterer, M.; Vodermayer, C.; Wotruba, G.; Mayer, M. Round-Robin-Test of Irradiance Sensors. In Proceedings of the 23th PVSEC, Valencia, Spain, 1–5 September 2008.

35. King, D.L.; Myers, D.R. Silicon-photodiode pyranometers: operational characteristics, historical experiences, and new calibration procedures. In Proceedings of the Conference Record of the Twenty-Sixth IEEE Photovoltaic Specialists Conference, Anaheim, CA, USA, 29 September–3 October 1997; pp. 1285–1288.

36. Garg, H.P.; Prakash, J. *Solar Energy Fundamentals and Applications*; Tata McGraw-Hill: New York, NY, USA, 2005.

37. Perez, R.; Seals, R.; Ineichen, P.; Stewart, R.; Menicucci, D. A new simplified version of the perez diffuse irradiance model for tilted surfaces. *Sol. Energy* **1987**, *39*, 221–231. [CrossRef]

38. Hofmann, M.; Seckmeyer, G. A New Model for Estimating the Diffuse Fraction of Solar Irradiance for Photovoltaic System Simulations. *Energies* **2017**, *10*, 248. [CrossRef]

4.3 Research Article C: Why PV Modules Should Preferably No Longer Be Oriented to the South in the Near Future

4.3.1 Declaration of my contribution

The author of this thesis conceived and designed the study and wrote the draft paper. The author also analyzed the data and performed the calculation used in this study. Gunther Seckmeyer initiated the investigation on the performance of differently oriented PV modules. Gunther Seckmeyer and Eduardo. W. Luiz contributed to the conception and design, analysis, and interpretation of the data. All the authors significantly contributed to the final version of the manuscript.

4.3.2 Published article

energies

MDPI

Article

Why PV Modules Should Preferably No Longer Be Oriented to the South in the Near Future

Riyad Mubarak *, Eduardo Weide Luiz and **Gunther Seckmeyer**

Institute for Meteorology and Climatology, Leibniz Universität Hannover, Herrenhäuser Straße 2,
30419 Hannover, Germany; luiz@muk.uni-hannover.de (E.W.L.); seckmeyer@muk.uni-hannover.de (G.S.)
* Correspondence: mubarak@muk.uni-hannover.de

check for
updates

Abstract: PV modules tilted and oriented toward east and west directions gain gradually more importance as an alternative to the presently-preferred south (north in the Southern Hemisphere) orientation and it is shown to become economically superior even under the reimbursement of feed-in tariff (FIT). This is a consequence of the increasing spread between the decreasing costs of self-consumed solar power and the costs for power from the grid. One-minute values of irradiance were measured by silicon sensors at different orientations and tilt angles in Hannover (Germany) over three years. We show that south-oriented collectors give the highest electrical power during the day, whereas combinations of east and west orientations (E-W) result in the highest self-consumption rate (SC), and combinations of southeast and southwest (SE-SW) orientations result in the highest degree of autarky (AD), although they reduce the yearly PV Power by 5–6%. Moreover, the economic analysis of PV systems without FIT shows that the SE-SW and E-W combinations have the lowest electricity cost and they are more beneficial in terms of internal rate of return (IRR), compared to the S orientation at the same tilt. For PV systems with FIT, the S orientation presently provides the highest transfer of money from the supplier. However, as a consequence of the continuing decline of FIT, the economic advantage of S orientation is decreasing. E-W and SE-SW orientations are more beneficial for the owner as soon as FIT decreases to 7 Ct/kWh. East and west orientations of PV modules do not only have benefits for the individual owner but avoid high costs for storing energy—regardless who would own the storage facilities—and by avoiding high noon peaks of solar energy production during sunny periods, which would become an increasing problem for the grid if more solar power is installed. Furthermore, two types of commonly used PV software (PVSOL and PVsyst) were used to simulate the system performance. The comparison with measurements showed that both PV software underestimate SC and AD for all studied orientations, leading to the conclusion that improvements are necessary in modelling.

Keywords: incident solar radiation; PV output power modelling; tilt angle; orientation; rooftop solar

1. Introduction

Decarbonization of our energy supply is an important component to fulfill pledges of the Paris Agreement to keep the global warming below 1.5 °C, because 65% of the world's current CO_2 emissions are due to burning fossil fuels [1]. Renewable energy is one of the most cost-effective options to replace fossil fuels and to reduce electricity-related emissions. In recent years, many countries have begun a transition to more sustainable energy supply based on renewable energies. Solar energy represents the most abundant natural energy resource on the earth and has the potential to replace fossil fuels to satisfy this clean energy demand of our society in future [2]. This exceptional energy source is the most simple and economic renewable energy technology available that can be easily installed, especially on

rooftops of houses. The costs for solar modules, measured in $/Wp, have reduced by as much as 90% during the last decade and are expected to fall further in the future [3].

Consequently, the evolution of renewable energy over the past decade has surpassed most expectations. By the end of 2018, global total renewable generation capacity reached 2351 GW. PV solar electricity has developed rapidly in minor private systems, as well as in large-scale installations connected to national grids. Solar energy represented around 20.6% of renewable energy generation in 2018, with capacities of 486 GW [4].

The solar irradiance changes with geographical location, season, and time of the day according to sun position in the sky. In addition, it varies by the influence of clouds, aerosols, and ground reflection. The orientation and tilt angle of PV collectors are among the most important parameters that affect the performance of a PV system, as they determine the amount of solar radiation received by the PV collector [5]. The orientation and inclination of a PV installation has two effects on system output: On the one hand, there is a larger or smaller amount of total annual yield; on the other hand, there is an impact on the seasonal or daily timing of peak energy generation [6]. In general, PV systems are divided into fixed and tracking systems. Fixed systems are often small systems installed on the roof of a building, while tracking systems are often large PV systems installed to maximize the solar radiation that reaches them [7]. Module performance is also affected by local factors for individual locations e.g., cloudiness, temperature, shading, dust, precipitation, and bird droppings [8].

Based on Earth-sun geometry, many studies were carried out to find the optimum tilt angle and orientation of PV systems in certain areas worldwide, e.g., Italy [9], Turkey [10], Australia [11], the United States [12], India [13], China [14], and Ghana [15]. Most previous studies show that the optimal fixed tilt angle of PV collectors depends only on geographical latitude (φ), if local weather and climatic conditions are not considered. However, because of the diffuse solar radiation, the optimal tilt angles may differ from those in reality. Huld et al. [16] showed that climate characteristics have a huge influence on the optimal tilt angle in Europe. Lave and Kleissl [12] showed that the optimal tilt is reduced by up to 10 degrees when cloudiness is taken into consideration, particularly in the northern United States. European studies [17,18] concluded that the optimum tilt must be reduced by 10° to 20° between southern and northern Europe because of the same effect. Beringer et al. [19] showed that solar collectors oriented to the South at a tilt angle of 50°–70° in the winter months (October–March) and 0°–30° in the summer months (April–September) would result in the highest monthly yield for the location of Hannover, Germany.

Rooftop PV systems have gained importance in the last decade, especially from the drop in the cost of solar PV modules and the increase of end-consumer electricity tariff. According to recent studies, up to 25% of EU electricity consumption could be potentially produced in small rooftop PV systems installed in the existing EU building [20]. Other authors estimate that all electricity needs can be produced on rooftops [21]. There is increased interest in the self-consumption (SC), i.e., the part of PV power production that is consumed by the house owner. The savings from self-consumed PV-generated electricity are much higher than the profit from selling excess generation at spot prices. It may also have a positive effect on the distribution grid and make the production profiles of PV systems connected to the grid smoother.

The SC depends mainly on the system size: The more PV power installed, the more often the produced electricity exceeds consumption; i.e., it is non-linear with installed power [22]. SC can also be increased by energy storage and by load management; i.e., the influence of temporal resolution becomes less distinct with added a battery storage [23]. In practice, the SC rate can range from a few percent to a theoretical maximum of 100%, depending on the PV system size and load profile. Moreover, estimation of SC depends also on time resolution; i.e., it is overestimated when using hourly data of PV electricity production and household load profiles. Luthander et al. [24] found that for individual buildings, sub-hourly data are needed to capture the behavior of high peak power. Leicester et al. [25] found that SC is overestimated by 71.3% when using hourly data, compared with 54.8% when using one-minute data. Accordingly, high temporal resolution data are required to quantify SC accurately.

There are very limited studies that described simultaneous direct measurements of PV generation and consumption. However, one method to obtain more data with greater variety is to use PV data and separately-obtained load profile data, and estimate the SC fraction [25]. With the present reimbursement for feed-in tariffs that value just the yearly sum fed into the grid, suitability studies focused for rooftop have just concentrated on the yearly yield. Many studies and online web tools concerning the suitability of the orientation of rooftop implicitly take only the yearly sum into account [26]. Calculations for the diurnal variability are lacking.

In this study, we use one-minute data to compare the outputs of 12 solar collectors at various tilt and azimuth angles in order to propose an alternative concept for increasing SC via non-south-oriented PV systems and investigate its potential. The calculations are based on measurements from silicon sensors with different orientations and tilt angles in Hannover (Germany). The SC of all orientations is calculated by using a set of separately measured load profiles in order to evaluate the best and more-economic orientations for rooftop PV systems. The results are also compared with the simulated values of two widely used PV software packages, PVSOL [27] and PVsyst [28] to validate this software. Detailed information about the simulation parameters are listed in Tables.

2. Methodology

The input dataset used in this study is composed of one-minute output of 12 solar collectors (Figure 1) installed for three years (2016–2018) on the roof of the Institute for Meteorology and Climatology (IMUK) of the Leibniz Universität Hannover (Hannover, Germany; 52.23° N, 9.42° E and 50 m above sea level). Measurements have been made, using crystalline silicon PV devices with individual temperature sensors (Mencke and Tegtmeyer GmbH, Hameln, Germany). The PV devices have been calibrated by the manufacturer in November 2013 and they are cleaned regularly to prevent the accumulation of dirt and dust. In addition, all devices are compared after one year of measurements by placing them side by side horizontally. These comparisons were performed under different weather conditions and have showed an agreement within ±3%.

Figure 1. Set of solar PV devices based on silicon sensors mounted in several different tilt angles and orientations, operational at the IMUK (Institute for Meteorology and Climatology) [IMUK, 2017].

Two groups of identical devices are considered here: The first group consist of devices with 45° tilt, oriented to S, E, W, SE, and SW; the second group consists of vertical devices, oriented to S, E, W, SE, SW, and N. The tilt angle for the first group (45°) is chosen to represent the large number of roof pitches, where most residential houses in Germany were built with a tilted roof angle between 40° and 45° [29]. According to the initial design of the measurement system, the S measurements are conducted at tilt angles of 40° and 50°, therefore we take the average of both sensors (40° and 50°) to represent the PV outputs at 45° tilt; the uncertainty resulting from this procedure and other orientation uncertainties

are less than 1% according to PVGIS calculations. Table 1 shows an overview about the inclination uncertainty, according to a Photovoltaic Geographical Information System (PVGIS) calculation [30] for Hannover.

Table 1. Annual PV energy produced in Hannover with respect to the optimal inclination [%] according to PVGIS.

	East				←					**Azimuth**			→						**West**
tilt	90	80	70	60	50	40	30	20	10	0	10	20	30	40	50	60	70	80	90
0	86	86	86	86	86	86	86	86	86	86	86	86	86	86	86	86	86	86	86
10	86	87	88	89	90	91	92	92	93	93	93	92	92	91	90	89	88	87	86
20	84	86	88	90	92	94	95	96	97	97	97	96	96	94	93	91	89	87	84
30	81	84	87	90	93	95	97	98	99	99	99	98	97	96	93	91	88	85	81
40	78	82	85	89	92	94	96	98	99	100	99	98	97	95	92	89	86	82	78
50	74	78	82	86	89	92	94	96	97	97	97	96	95	92	90	87	83	79	74
60	70	74	78	82	85	88	90	92	93	93	93	92	91	89	86	82	79	74	70
70	65	69	73	76	80	82	84	86	87	87	87	86	85	83	80	77	73	69	65
80	59	63	67	70	73	75	77	78	79	80	79	79	78	76	73	70	67	64	60
90	53	57	60	63	65	67	69	69	70	70	70	70	69	68	66	63	60	57	54

3. PV System Output Calculation

In general, there are several ways to calculate the power output of PV systems. We used in this study a simple method for calculating it [31]:

$$P_{m,i} \;=\; P_{rel} \times \frac{I_{m,i}}{I_{UTC}} \times \left(1 + \gamma\left(T_{sen,i} - 25\,^{\circ}\text{C}\right)\right) \times PLF \tag{1}$$

where P_m is power output of the PV system, P_{rel} is the rated PV system power (the output power of PV device under standard test conditions), I_m is the measured solar irradiance, $I_{UTC} = 1000$ W/m^2, T_{sen} is the module temperature (in °C), γ is power temperature coefficient, and PLF is the power loss factor.

The equation contains the temperature coefficient to take into account the drop of sensor signal because of the temperature and to correct the testing conditions. The losses because of inverter and the degradation mechanisms of the PV sensors (0.5%/a) are included in Equation (1) as a PLF, which is time dependent because of the degradation of sensors.

3.1. Load Profile

The power generation profiles were calculated by using the Equation (1). A synthesized dataset of actual measured load profiles provided by HTW Berlin [32] is used to simulate a household's consumption pattern of electricity. The data set consists of 74 load profiles of German single-family houses with a temporal resolution of 1 min for every day of the year. The load profile used for the calculations is the average of six selected profiles which have an annual consumption between 3900 kWh and 4055 kWh. The average profile has an annual electricity consumption of 4006 kWh (Figure 2). It can be assumed that the selected profiles represent a four-person household.
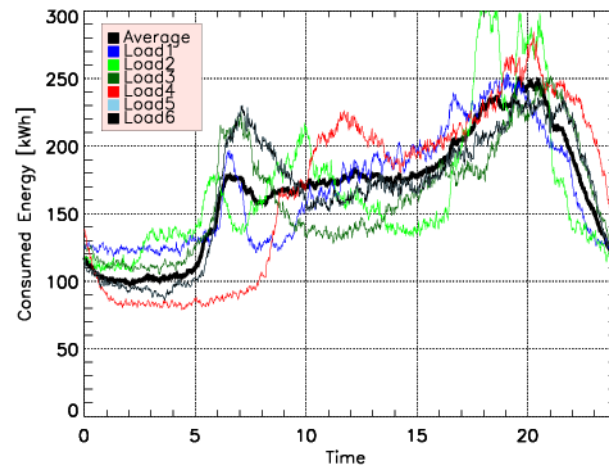
Figure 2. Six private household profiles which have an annual consumption between 3900 kWh and 4055 kWh [32]. The average profile (black curve) has an annual electricity consumption of 4006 kWh.

3.2. Economic Parameters

Feed-in tariffs are the most common policy instrument worldwide to support renewable energy. Many PV installations sell their power at local grid, and the majority of feed-in tariff contracts are at a fixed price per kWh for 10–20 years [33]. This results in an optimal orientation that is the same for both maximum economic yield and maximum energy production. The German FIT for solar photovoltaic uses varying rates depending on the size of the project. Countries in which the FIT was eliminated usually replace it by net metering schemes. The net metering is also used in many different countries under different rules, but consists of a system in which the excess electricity injected into the grid can be used at a later time to compensate the consumption when PV generation is not sufficient. The compensation usually covers a specific period (usually 1–3 years) depending on the country's regulations, and any excess energy after this period is not remunerated. So, the main idea is to configure the system settings in a way its annual production does not exceed the annual consumption, minimizing the deviation between them and increasing SC. Examples of countries using net metering schemes are: the United States (with particular conditions depending on the state), Denmark, Greece, Australia, Brazil, Mexico, and Chile [34–36].

The FIT used in the financial model for the calculation is 10.64 Ct/kWh (from July, 2019) and the price is constant for 20 years. The electricity price (30.22 Ct/kWh) considered in the calculations in this study represents the average price level for private households in Germany in 2019, including taxes and levies [37]. The increase of electricity price is expected to slow down to 2% p.a. as an average value during the next 20 years. The levelized cost of PV energy (LC) in northern Germany ranges between 9.89 Ct/kWh and 11.54 Ct/kWh, depending on the annual solar irradiance [38]; a value of 10 Ct/kWh is used in this study.

In the design of PV systems, the self-consumption rate (SC) and the degree of autarky (AD) are two important quantities used to assess the congruence of the PV generation and electricity demand profiles. The self-consumption rate is defined by the ratio of PV directly used (P_{DU}) to the total amount of PV power generated (P_m), according to Equation (2).

$$SC = \frac{P_{DU}}{P_m} \tag{2}$$

The degree of autarky is defined as a ratio of PV directly used to the total consumption by the household [39], according to Equation (3).

$$AD = \frac{P_{DU}}{L} \tag{3}$$

where L is the energy consumed by the loads.

The electricity price P_E used to evaluate the economic impact of PV system at specific orientation has been calculated according to Equation (4).

$$P_E = (P_G - P_{Fi}) + LC \tag{4}$$

where P_G is the grid electricity price, P_{Fi} is the FIT, and LC is the levelized cost of PV energy.

Figure 3 shows a workflow diagram used in this study to calculate the SC with the feed-in components. The calculations are always dependent on the consumption of electricity, with the primary objective to fulfil the demand from the PV produced energy, before purchasing from the public grid. If the produced electricity exceeds the consumption of the house, the excess is supplied to the public grid. Moreover, the internal rate of return (IRR) for all available orientations has been calculated over the life cycle of the PV system (20 years) in order to enlighten prospective owners/investors of rooftop PV systems. The IRR, defined as a discount rate that makes the net present value from all cash flows from a project equal to zero, is used to evaluate the attractiveness of a project or investment, and it is probably one of the most meaningful metric for investors [40]. The degradation mechanisms of the PV collectors (0.5%/a) and an annual increase of electricity price (2%/a) were taken into account in the IRR calculations.
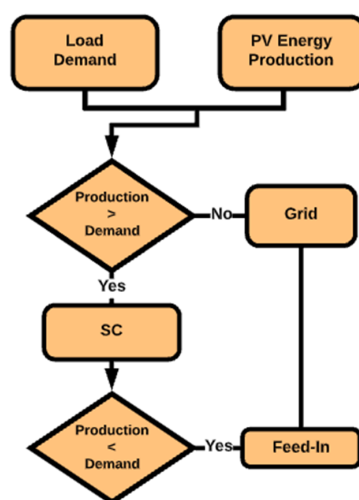

Figure 3. Schematic view of the calculation of system components. The calculations are always dependent on the load demand, with the primary objective to fulfil it from the PV produced energy, before purchasing electricity from the public grid.

3.3. PV Software

PV estimation models are generally used to estimate the expected energy output of a PV system. These models need specific input parameters such as meteorological conditions of the location, system design details, and definitions of the main components used. A variety of software for the simulation of PV systems is available in the market, including PVsyst, PVSOL, and others. PVsyst, developed at the University of Geneva, is one of the most common modeling software tools used in the PV industry to simulate the performance of grid-connected or stand-alone PV systems and calculate their energy yield.

PVsyst allows the definition of meteorological databases from many different sources and formats, as well as on-site measured data [41]. On the other hand, PVSOL is a German software developed by Valentine Software [27] for dynamic simulation with 3D visualization and detailed shading analysis of photovoltaic systems. PVSOL gives customers the best return on their investment by visualizing systems, and it can perform economic and performance analysis with comprehensive reports.

4. Results and Discussion

4.1. Production and Consumption under Different Weather Conditions

Figure 4 shows the PV production profiles for the S and E-W orientations during three days of May 2018 with different weather conditions (clear sky, partly cloudy, and fully cloudy) and correspondent customer load profiles for the same days of the year.
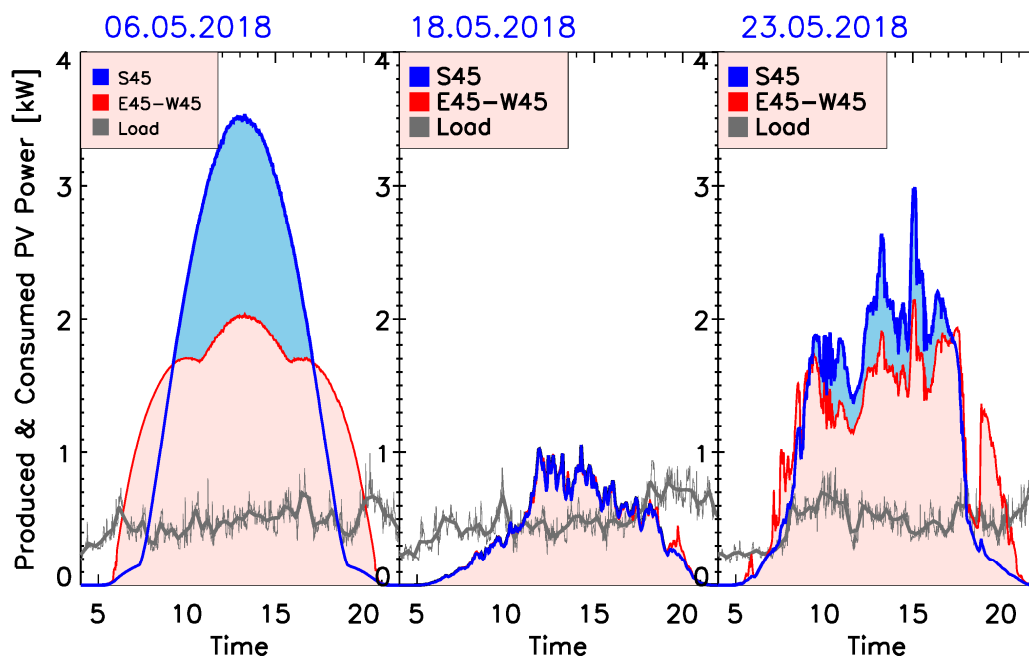

Figure 4. PV Production profiles for three days of May 2018 and the correspondent customer load profiles for the same days of the year. The thick (gray) curve represents the 10-minte average consumption.

The load profiles show different peaks over the day according to consumption patterns, while, the PV power production changes according to the movement of the sun and the weather conditions. The influence of orientation is shown clearly in clear sky days, when the energy production depends mainly on the sun's position. The E-W orientation covers more the edges of the day and reduces noon peak. On the other hand, the orientation is irrelevant under cloudy conditions, when the solar irradiance dominated by diffuse component. In general, SC rate is higher under cloudy conditions.

4.2. Annual Insolation

The annual total solar energy as function of surface azimuth and tilt angles is depicted in Figure 5. The left side histogram shows that the maximum annual total energy is for a south-facing surface with a tilt angle between 30° and 40°, closer to 40°. The annual total energy is less than the maximum by approximately 0.2% for surface orientation of 30° S, and it decreases gradually with higher or lower tilt angles. The annual produced energy for the surfaces oriented at the same tilt angle (45°) toward E and W are 77.0% and 75.9% of the optimal orientation respectively. For orientations of 45° SE or SW, the

annual total energy produced are 94.8% and 93.3% of maximum produced energy. The inequality in total energy for E and W and in SE and SW may denote asymmetric distributions of solar irradiance before and after midday. On the right histogram of Figure 4 we can see that, for a vertical surface with orientation of 90° south, the produced energy is 66.2% of the 40° tilted surface, whereas it is about 50% for E and W surfaces. The annual total energy of the northern vertical surface is reduced by about 74%.
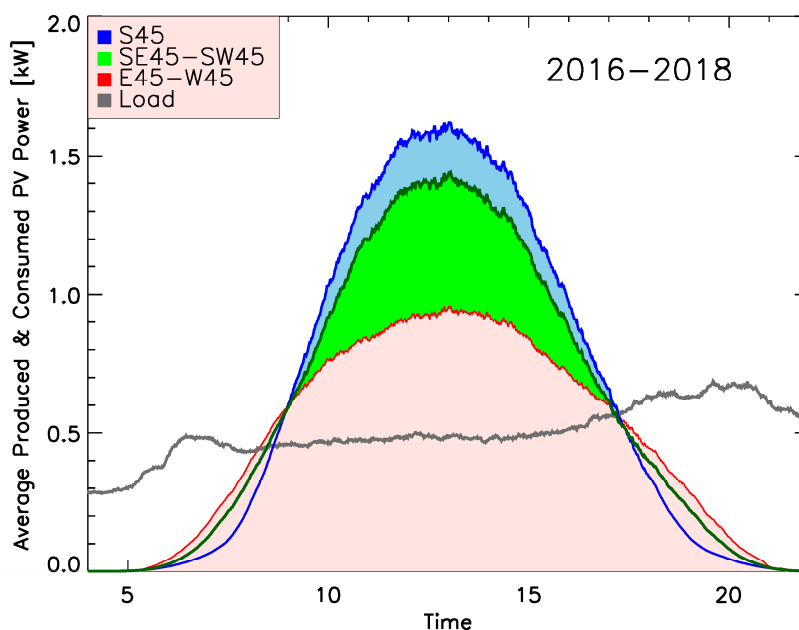

Figure 5. Produced and consumed PV power averaged over all days of the years 2016–2018 for the S, E-W, and SE-SW orientations at 45° tilt. The area below the gray curve represents the average load profile. The E-W and SE-SW facing installation produce more electricity in the mornings and evenings with a lower midday peak, so they match the load profile more closely.

In general, the amount of energy produced by a PV collector is proportional to solar radiation received by a surface in a specific orientation. Table 2 shows the annual produced energy and its percentage from the maximum value (at 45° S) for different orientations and tilt angles. The table also shows the SC rate and AD for each orientation. For 45° tilt surfaces, the lowest SC rate (37.9%) is for the S facing solar installation, while the highest SC rate (51.4%) is for the E-W combination. The high SC rate is because the power output of E-W installation matches the load profile more closely, producing more electric energy at the beginning and at the end of the day, with a lower midday peak (Figure 6). The AD has its maximum at SE-SW combination (40.7%) and its minimum at the E orientation (35.4%). Moreover, the economic efficiency of all studied orientations for the cases with and without FIT is also listed in Table 2. Overall, the E-W and SE-SW combinations have the lowest electricity cost (29.2 Ct/kWh and 29.1 Ct/kWh respectively), while the E orientation has the highest one (30.7 Ct/kWh), both cases for the system without FIT. For PV systems with FIT, the S-facing systems have the lowest electricity price (22.0 Ct/kWh) because of the high PV generation and accordingly the high feed-in amount, while the E-facing systems have the highest price (25.6 Ct/kWh).

Table 2. Results of measurement for a PV size of 4.8 kWp at different tilt angles in Hannover, Germany.

| Orientation		S45	E45	W45	E45 + W45	SE45	SW45	SE45 + SW45	S90	E90	W90	SE90	SW90	N90
Percentage of SS45 (%)		100	76.2	75.0	75.6	94.6	93.1	93.8	66.8	49.8	50.3	64.6	64.4	25.8
Annual PV Generation (kWh/a)		4145	3157	3111	3134	3921	3859	3890	2769	2064	2046	2678	2655	1069
SC rate (%)		37.9	44.9	47.9	51.4	38.6	40.7	41.9	50.9	57.4	66.2	50.0	55.4	95.1
Autarky (%)		39.2	35.4	37.2	40.3	37.8	39.2	40.7	35.2	29.6	34.5	33.4	36.7	25.4
Cost Ct/kWh	No FIT	29.5	30.7	30.1	29.2	30.5	29.5	29.1	30.9	32.7	31.1	31.4	30.4	34.0
	With FIT	22.0	25.6	25.3	24.7	23.0	22.8	22.5	27.0	30.2	29.1	27.6	27.1	33.9
IRR % Over 20 ys	No FIT	1.59	0.20	0.84	1.90	1.10	1.57	2.09	0.13	−2.15	−0.19	−0.53	0.70	−4.23
	With FIT	7.05	4.13	4.42	5.14	6.29	6.45	6.82	3.23	0.12	1.45	2.61	3.33	−4.10
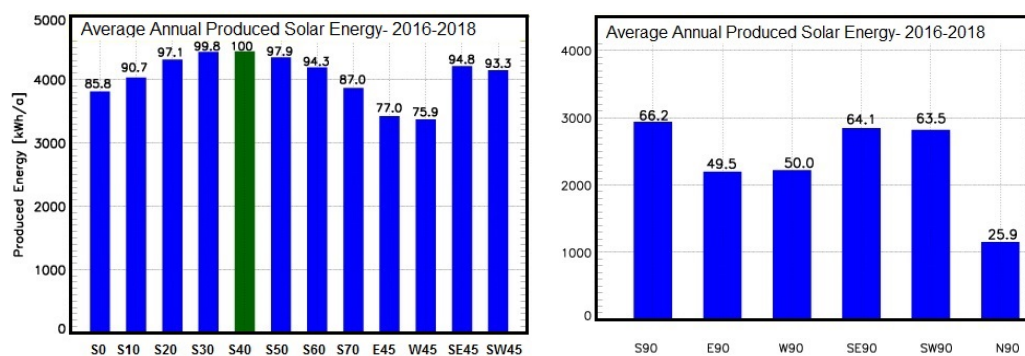
Figure 6. Average annual total solar energy (2016–2018) measured at IMUK and normalized values (in %) with respect to the annual total maximum energy at 40° S. The solar energy decreases for higher or lower tilt angles and for other azimuth angles.

The IRR analysis of PV systems without FIT shows that the SE-SW and E-W orientations tilted at 45° is more beneficial with an IRR value of 2.09% and 1.90%, respectively, when compared to the S orientation at the same tilt with 1.59%. For PV systems with FIT, the IRR for the S orientation is higher with a value of 7.05%, compared to the SE-SW and E-W orientations with 6.82% and 5.14%, respectively.

As expected, for the vertical surfaces, the S orientations gives the highest output (66.8% of the maximum), while the lowest energy is produced by N-facing surface (25.8 of the maximum), because of the Earth-sun geometry in the northern hemisphere. In terms of the SC rate, the N surfaces have the highest rate, due to the low energy production in this direction, while the lowest rate (50.0%) is for the SE surface. The AD has its maximum at SW orientation (36.7%) and it is minimum at N orientation (25.4%). Accordingly, the SW orientation has the lowest electricity cost (30.4 Ct/kWh) for the system without FIT, while the S and SW orientations have the lowest electricity cost (27.1 Ct/kWh) for PV systems with FIT. The difference between prices is found to be small and is within ±3%. However, we found that a changing the irradiance of 3% cause only a small change of the price and therefore conclude that the assessed measurement uncertainties do not significantly affect the prices.

Moreover, we examined whether the PV self-consumption will be influenced similarly in all investigated orientations, by changing the system size. For that purpose, we varied the module area by +/−50% in 5% steps (Figure 7). As expected, the SC rate increased by a reduction of the module area (in our specific case the default area was 24.3 m^2) for the orientations (S45, E45-W45, SE45-SW45). This increase only slightly depends on the orientation: The E40-W40 increased by 29% while the south orientation increased by 26% with a reduction of the module area of 50%. While it is obvious that the SC rate becomes smaller for larger module areas, an increase in module size will affect all orientations, but the S orientation will be affected slightly less than the other orientations.
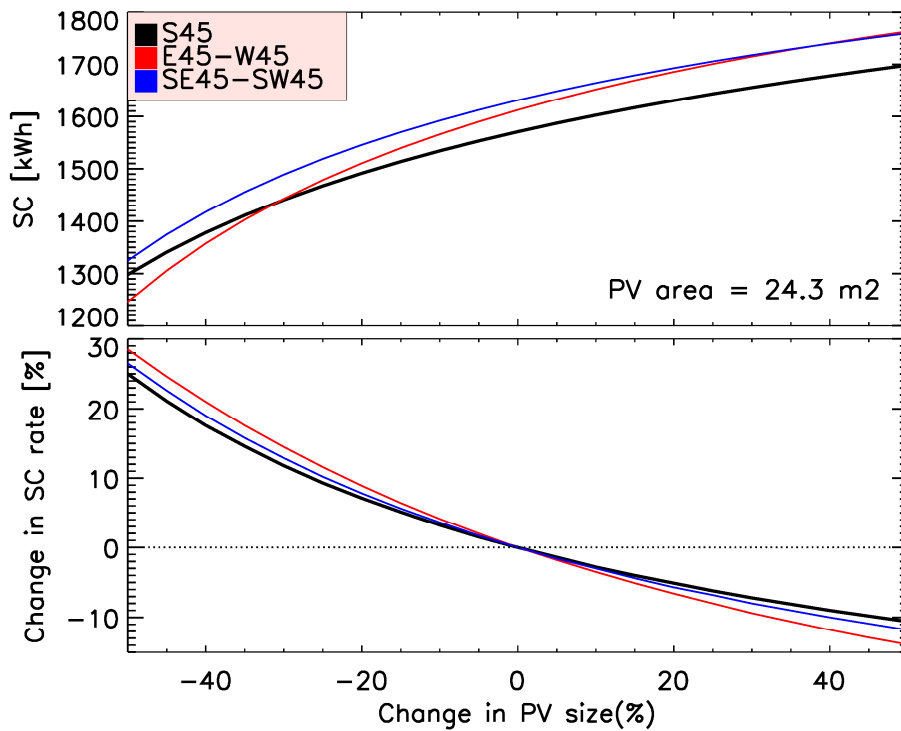
Figure 7. The change in self-consumption (SC) rate with varying the module area by +/−50% in 5% steps. The change in SC rate depends on the orientations.

4.3. Effects of the Changing Feed-In Tariffs

Feed-in tariffs of renewable energy in Germany are decreasing as each year passes and PV FIT drops faster than any other renewable power source. In the last 15 years, the FIT recorded a decrease of approximately 80% for small rooftop PV installations and 90% for medium-size PV systems [42]. Figure 8 shows the decrease in German FIT from 2000 to 2020.
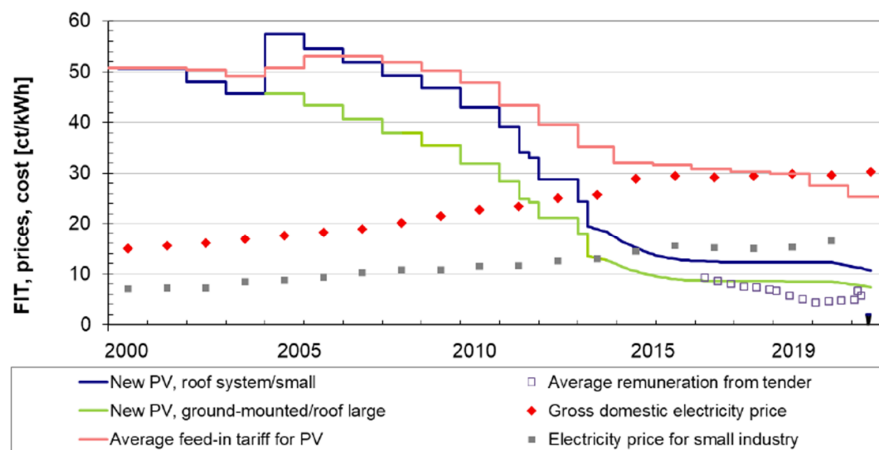

Figure 8. The changes of PV FIT and electricity price in Germany (2000 to 2020). The FIT dropped approximately 80% for small rooftop PV installations and 90% for medium-size PV systems [42].

According to Obane and Okajima [43], the FIT scheme for small PV systems is fast approaching its closure or expiration in many countries. In Germany, the EEG law stipulates that further FIT

systems will not be allowed, when the total PV installations reach 52 GW. At the end of April 2018, the country had 43.8 GW PV installed. With the current tenders of PV, this cap is expected to be reached in 2020 [44]. However, the German government presently reconsidering this plan and is considering to allow FIT in future when the 52 GW is exceeded. With decreasing FIT self-consumption is gaining higher importance, especially with increasing cost of delivering PV electricity and rapid decline in the cost of solar PV modules. In addition, after 2020, the FIT will gradually expire for the oldest PV plants [42] and the produced PV power will be mainly used for SC. Thus, E-W and SE-SW orientations will provide the highest SC rate and will be more beneficial for the householders. Our calculation shows that the higher benefit of south orientation is no longer existent if FIT decreases to 7.0 Ct/kWh or lower, where at least the SE-SW orientation will have a higher IRR that the S orientation.

The economic calculations above were done for the conditions of the present FIT in Germany. The major conclusions, however, can used for many countries around the world, which apply FIT or similar PV cost structures. The results are especially relevant for the countries, which offer a very low FIT (e.g., New Zealand and Portugal) or for which eliminated the FIT scheme (e.g., UK, Spain, Czech Republic, Italy).

4.4. Comparison with PV Software

For simulation of the IMUK measurement system, a fixed PV system configuration, consisting of a 4.8 kWp is considered in the calculations, corresponding to the installation of 24 modules. Moreover, the same load profile that is used for the calculation of SC and AD at IMUK is also used in both models. Table 3 shows the important model parameters used in the simulation.

Table 3. Model parameters used in comparison.

Parameter	Model (PVSol, PVSyst)
Modules	4.8 kWp, mono, 24 modules
Inverter	ABB, 4.6 kW
Climate data	Meteonorm 7.2
Transposition model	Perez-Ineichen model
Diffuse radiation model	Perez model

Both simulation programs have been run for each orientation separately. Table 4 shows the simulated annually produced energies for all studied orientations and tilt angles. The programs overestimate the south-tilted irradiance and most of the studied orientations. This may result from the use of an anisotropic model (Perez-Ineichen model) to calculate the tilted irradiance, where we found in a previous study [45] that anisotropic models overestimate the south-tilted irradiance and most vertical-tilted irradiances.

The table also shows the SC and AD fractions for each orientation. For the 45°-tilt surfaces, the lowest SC (PVsyst = 32.9% and PVSOL = 32.3%) are for the S orientation, while the highest SC (PVsyst = 43.1% and PVSOL = 44.5%) is for the E-W combination, which agrees with the measured results. According to PVsyst, the AD has its maximum at E-W combination (37.4%) and at S orientation (34.7%) according to PVSOL calculations, while it is minimum at the W orientation for both models (PVsyst = 34.0%, PVSOL = 31.9).

For the vertical surfaces, the results of both programs show also that the S orientations gives the highest output, while the lowest energy is produced by a N-facing surface. In terms of the SC rate, the N surface has the highest fractions (PVsyst = 85.7% and PVSOL = 89.0%), while the lowest (40.7%) are for the S surfaces. The AD has its maximum for S surfaces (PVsyst = 31.8% and PVSOL = 30.6%) and it is minimum at the N orientation (PVsyst = 24.6% and PVSOL = 24.7). Table 4 also shows that both PV programs overestimate the percentage of energy production at 45° in most orientations versus the southern maximum value.

Table 4. Results of PV software PVSPL and PVSyst for a PV size of 4.8 kWp at different orientation and tilt angles.

Orientation	S45	E45	W45	E45 + W45	SE45	SW45	SE45 + SW45	S90	E90	W90	SE90	SW90	NN90
PVsyst Annual PV (kWh)	4457	3596	3531	3564	4250	4174	4212	3161	2439	2362	3053	2938	1148
Percentage of the max (%)	100	79.5	79.3	78.7	94.8	94.1	93.9	71.0	55.1	54.6	68.4	67.2	26.0
SC (%)	32.9	40.7	38.9	43.1	34.9	33.9	36.1	40.7	49.5	46.6	42.3	40.9	85.7
AD (%)	36.2	35.6	34.0	37.4	36.4	35.1	37.3	31.8	30.1	28.0	31.9	30.3	24.6
PVSOL Annual PV (kWh)	4330	3425	3046	3148	4160	3857	3920	3012	2289	1975	2945	2629	1115
Percentage of the max (%)	100	77.8	68.7	71.3	95.9	88.3	90.1	69.9	53.1	45.9	68.4	61.1	25.8
SC (%)	32.3	39.9	43.1	44.5	33.4	35.6	35.6	40.7	50.4	57.0	41.5	45.6	89.0
AD (%)	34.7	33.4	31.9	34.1	34.5	33.8	34.5	30.6	28.8	28.1	30.5	29.9	24.7

In order to have comparable results of simulation with the measured results, the generated PV energy of the IMUK system have been controlled by changing the PV area to produce the same annual output as the inverter output of simulation software. Figure 9 shows the results of the comparison: Both PV programs underestimate SC and AD for all studied orientations; SC rate was underestimated by 0.4% to 14%, while AD values were underestimated by 1.3% to 8.1%. These results lead to the conclusion that improvements are necessary in the modelling of SC and AD.
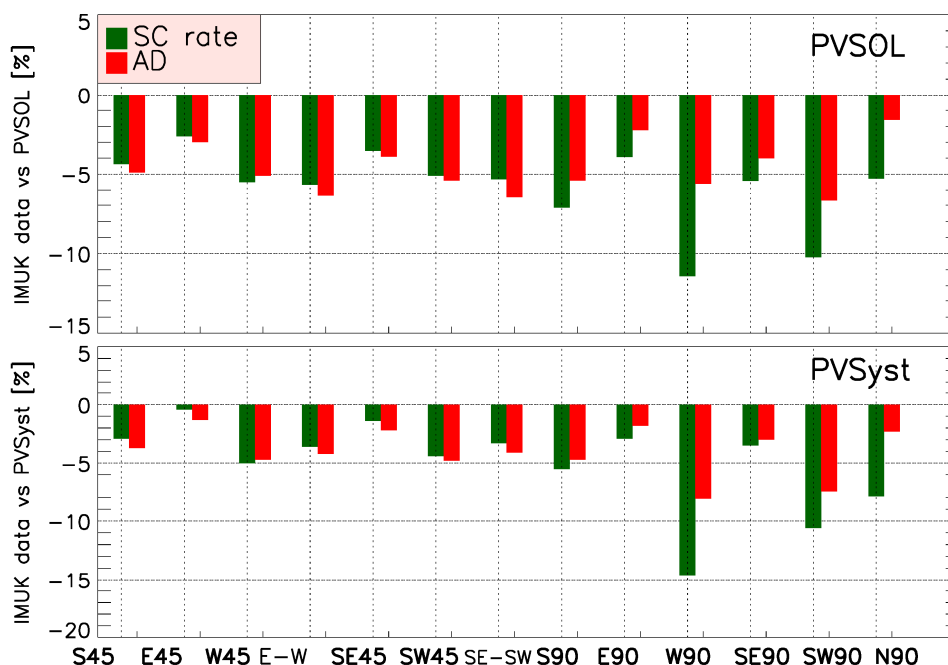

Figure 9. Comparison between IMUK results and simulated values. The used PV simulation software underestimate self-consumption and degree of autarky at all studied orientations and tilt angles.

5. Conclusions

Using one-minute measured data of PV energy, the outputs of 12 solar collectors at various tilt and azimuth angles in Hannover (Germany) were analyzed. For validation, the results were also compared with the simulated values of two widely used PV software: PVSOL and PVsyst.

The measurements show that a south-oriented generator at about 40° gives the highest electricity profile. For non-vertical devices, the combinations of E and W orientations result in the highest SC rate and combinations of SE and SW orientations result in the highest AD. E-W and SE-SW combinations have the lowest electricity coast for PV systems without FIT, while the E orientation has the highest one. For PV systems with FIT, S orientation provides the highest transfer of money from the supplier. The economic analysis using IRR of PV systems without FIT shows that the SE-SW and E-W orientations tilted at 45° is slightly more beneficial, while S orientation has higher IRR for PV systems with FIT.

However, in light of the continuing decline of FIT, the advantage of S orientation is decreasing and our results show that E-W and SE-SW orientations will be more beneficial if FIT is to 7 Ct/kWh or lower. East and west orientations of PV modules and not south orientations should be supported because they would also reduce the economic costs for storing renewable energy—regardless who would own the storage facilities—and avoid high noon peaks of solar energy production, which would become a problem for the grid for higher solar power penetrations levels.

Furthermore, the results show that the vertical tilted surfaces represent a high potential for PV energy production and facade PV systems could be an alternative for many people, especially for those who do not have access to a rooftop. So far, combinations of different vertically tilted modules as well as the combinations between vertical and 45°-tilted surfaces have not yet been taken into account because of the problems with the standardization of shadows from nearby building, trees and, other obstacles.

The calculation in this study assumed a constant price for the FIT over the day. However, if we consider the general trend to link the price of electricity with the spot market price, so that the price of selling or feeding electricity to grid changes according to the production and demand, the E-W and SE-SW orientations might become even more beneficial against S-facing PV systems. In addition, the suitability criteria for rooftops carrying solar modules must be questioned [26]. More roofs should be taken into account when diurnal variations are considered. Based on our measurements and analysis we conclude that the yearly sum of produced electricity can no longer be the only criterion for the installation of PV modules. Instead, other orientations may be more beneficial for both the owner and the society that uses solar power.

Regarding the model validation, both of the tested PV software overestimate the energy production at most studied orientations and also overestimate the percentage of these orientations when compared to the south-oriented generator. This result agrees with previous results [45], which showed that anisotropic models overestimate the S-tilted irradiance and most vertical irradiances. The need to improve existing modelling has also been shown in previous studies [46,47]. A major cause for the deviation between models and measurements may be the oversimplified assumptions about the sky radiance, which can be overcome by new measurement techniques [48,49]. Moreover, the study showed that the overestimation increases with increasing deviation from the south direction. In addition, both PV programs underestimate SC rate and AD for all studied orientations. SC rate was underestimated from 0.4% to 14%, while AD values were underestimated from 1.3% to 8.1%. These results lead to the conclusion that improvements are necessary when modelling SC and AD.

The amount of solar irradiance received by the surface of the PV collector is among the most important parameters that affect the performance of a PV system. Therefore, high-resolution tilted solar irradiance data in various orientations and weather conditions are needed to feed the models for better simulation of PV Power.

Nomenclature

SC	Self-consumption
AD	Degree of autarky
P_m	Power output of the PV system
P_{rel}	Rated PV system power
I_m	Measured solar irradiance
I_{UTC}	Solar irradiance at STC (1000 W/m^2)
T_{sen}	Sensor temperature
γ	Power temperature coefficient
Pdu	PV directly used energy
PLF	Power loss factor
φ	Geographical latitude φ
PVg	Total PV generated energy
Pe	Electricity price
PG	Grid electricity price
Pfi, FIT	Feed-in tariff
LC	Levelized coast of PV energy

References

1. Jäger-Waldau, A. Snapshot of Photovoltaics 2018. *EPJ Photovolt.* **2018**, *9*, 6. [CrossRef]
2. Ginley, D.; Green, M.A.; Collins, R. Solar energy conversion toward 1 TW. *MRS Bull.* **2008**, *33*, 355–364. [CrossRef]
3. Vartiainen, E.; Breyer, C.; Moser, D.; Medina, E.R. Impact of weighted average cost of capital, capital expenditure, and other parameters on future utility-scale PV levelised cost of electricity. *Prog. Photovolt. Res. Appl.* **2019**, 1–15. [CrossRef]
4. IRENA. Renewable Energy Statistics 2018, The International Renewable Energy Agency. Available online: https://www.irena.org//media/Files/IRENA/Agency/Publication/2019/Mar/RE_capacity_highlights_2019pdf?la=en&hash=BA9D38354390B001DC0CC9BE03EEE559C280013F (accessed on 26 October 2019).
5. Khoo, Y.S.; Nobre, A.; Malhotra, R.; Yang, D.; Ruther, R.; Reindl, T.; Aberle, A.G. Optimal orientation and tilt angle for maximizing in-plane solar irradiation for PV applications in Singapore. *IEEE J. Photovolt.* **2014**, *4*, 647–653. [CrossRef]
6. Hartner, M.; Ortner, A.; Heisl, A.; Haas, R. East to west—The optimal tilt angle and orientation of photovoltaic panels from an electricity system perspective. *Appl. Energy* **2015**, *160*, 94–107. [CrossRef]
7. Seme, S.; Krawczyk, A.; Łada, E.; Tondyra, Š.B.; Hadžiselimović, M. The Efficiency of Different Orientations of Photovoltaic Systems. *Przegląd Elektrotechniczny* **2017**, *93*, 201–204. [CrossRef]
8. Ghazi, S.; Ip, K. The effect of weather conditions on the efficiency of PV panels in southeast of UK. *Renew. Energy* **2014**, *69*, 50–59. [CrossRef]
9. Colli, A.; Zaaiman, W.J. Maximum-power-based PV performance validation method: Application to single-axis tracking and Fixed-Tilt c-Si systems in the Italian Alpine region. *IEEE J. Photovolt* **2012**, *2*, 555–563. [CrossRef]

10.   Bakirci, K. General models for optimum tilt angles of solar panels: Turkey case study. *Renew. Sustain. Energy Rev.* **2012**, *16*, 6149–6159. [CrossRef]

11.   Yan, R.; Saha, T.K.; Meredith, P.; Goodwin, S. Analysis of yearlong performance of differently tilted photovoltaic systems in Brisbane, Australia. *Energy Convers. Manag.* **2013**, *74*, 102–108. [CrossRef]

12.   Lave, M.; Kleissl, J. Optimum fixed orientations and benefits of tracking for capturing solar radiation in the continental United States. *Renew. Energy* **2011**, *36*, 1145–1152. [CrossRef]

13.   Agarwal, A.; Vashishtha, V.K.; Mishra, S.N. Comparative approach for the optimization of tilt angle to receive maximum radiation. *Int. J. Eng. Res. Technol.* **2012**, *1*, 1–9.

14.   Tang, R.; Wu, T. Optim. tilt-angles for solar collectors used in China. *Appl. Energy* **2004**, *79*, 239–248. [CrossRef]

15.   Uba, F.A.; Sarsah, E.A. Optimization of tilt angle for solar collectors in WA, Ghana, Pelagia Research Library. *Adv. Appl. Sci. Res.* **2013**, *4*, 108–114.

16.   Huld, T.; Šúri, M.; Dunlop, E.D. Comparison of potential solar electricity output from fixed-inclined and two-axis tracking photovoltaic modules in Europe. *Prog. Photovolt. Res. Appl.* **2008**, *16*, 47–59, ISSN 1099-159X. [CrossRef]

17.   Huld, T.; Müller, R.; Gambardella, A. A new solar radiation database for estimating PV performance in Europe and Africa. *Sol. Energy* **2012**, *86*, 1803–1815. [CrossRef]

18.   Quinn, S.W.; Lehman, B.A. Simple formula for the optimum tilt angles of photovoltaic panels. In Proceedings of the IEEE 14th Workshop on Control and Modeling for Power Electronics (COMPEL), Salt Lake City, UT, USA, 23–26 June 2013; pp. 1–8.

19.   Beringer, S.; Schilke, H.; Lohse, I.; Seckmeyer, G. Case study showing that the tilt angle of photovoltaic plants is nearly irrelevant. *Sol. Energy* **2011**, *85*, 470–476. [CrossRef]

20.   Bodis, K.; Kougias, I.; Jäger-Waldau, A.; Taylor, N.; Szabo, S. A high-resolution geospatial assessment of the rooftop solar photovoltaic potential in the European Union. *Renew. Sustain. Energy Rev.* **2019**, *114*, 109309. [CrossRef]

21.   Mertens, K. *Photovoltaics: Fundamentals, Technology and Practice*, 1st ed.; John Wiley & Sons, Ltd. Published: Hoboken, NJ, USA, 2014.

22.   Luthander, R. Photovoltaic System Layout for Optimized Self-Consumption. Uppsala Universitet. 2013. Available online: http://www.diva-portal.org/smash/get/diva2:637625/FULLTEXT01.pdf (accessed on 26 November 2019).

23.   Beck, T.; Kondziella, H.; Huard, G.; Bruckner, T. Assessing the influence of the temporal resolution of electrical load and PV generation profiles on self-consumption and sizing of PV-battery systems. *Appl. Energy* **2016**, *173*, 331–342. [CrossRef]

24.   Luthander, R.; Widen, J.; Nilsson, D.; Palm, J. Photovoltaic self consumprion in buidings: A review. *Appl. Energy* **2015**, *142*, 80–94. [CrossRef]

25.   Leicester, P.A.; Rowley, P.N.; Goodier, C.I. Probabilistic analysis of solar photovoltaic self-consumption using Bayesian network models. *IET Renew. Power Gener.* **2016**, *10*, 448–455. [CrossRef]

26.   Martín, A.M.; Domínguez, J.; Amador, J. Applying LIDAR datasets and GIS based model to evaluate solar potential over roofs: A review. *AIMS Energy* **2015**, *3*, 326–343. [CrossRef]

27.   PVSOL. PV*SOL Online—A Free Tool Forsolar Power (PV) Systems. 2019. Available online: http://pvsol-online.valentin-software.com/#/ (accessed on 6 May 2019).

28.   *PVSyst, Version, 6.79*; [*Computer Software*]; University of Geneva: Geneva, Switzerland, 2019.

29.   DGS. *EnergyMap.info*; Deutsche Gesellschaft für Sonnenenergie e.V.: Berlin, Germany, 2015.

30.   PVGIS. Overview of PVGIS data sources and calculation methods. European Commission. Available online: http://re.jrc.ec.europa.eu/pvg_static/methods.html (accessed on 26 November 2019).

31.   Idoko, L.; Anaya-Lara, O.; McDonald, A. Enhancing PV modules efficiency and power output using multi-concept cooling technique. *Energy Rep.* **2018**, *4*, 357–369. [CrossRef]

32.   Tjaden, T.; Bergner, J.; Weniger, J.; Quaschning, V. Repräsentative elektrische Lastprofile für Wohngebäude in Deutschland auf 1-sekündiger Datenbasis. Technical report, Berlin, Germany. Hochschule für Technik und Wirtschaft HTW Berlin. Available online: https://pvspeicher.htw-berlin.de/wp-content/uploads/2017/05/HTW-BERLIN-2015-Repr%C3%A4sentative-elektrische-Lastprofile-f%C3%BCr-Wohngeb%C3%A4ude-in-Deutschland-auf-1-sek%C3%BCndiger-Datenbasis.pdf (accessed on 26 November 2019).

33. Haysom, J.E.; Hinzer, K.; Wright, D. Impact of electricity tariffs on optimal orientation of photovoltaic modules. *Prog. Photovolt. Res. Appl.* **2015**, *24*, 253–260. [CrossRef]

34. Jager-Waldau, A.; Bucher, C.; Frederiksen, K.H.B.; Guerro-Lemus, R.; Mason, G.; Mather, B.; Mayr, C.; Moneta, D.; Nikoletatos, J.; Roberts, M.B. Self-consumption of electricity produced from PV systems in apartment buildings—Comparison of the situation in Australia, Austria, Denmark, Germany, Greece, Italy, Spain, Switzerland and the USA. In Proceedings of the 2018 IEEE 7th World Conf. Photovolt. Energy Conversion, WCPEC 2018—A Jt. Conf. 45th IEEE PVSC, 28th PVSEC 34th EU PVSEC 1424–1430, Waikoloa Village, HI, USA, 10–15 June 2018. [CrossRef]

35. Mojonero, D.H.; Villacorta, A.R.; Kuong, J.L. Impact assessment of net metering for residential photovoltaic distributed generation in Peru. *Int. J. Renew. Energy Res.* **2018**, *8*, 1200–1207.

36. Pereira da Silva, P.; Dantas, G.; Pereira, G.I.; Câmara, L.; De Castro, N.J. Photovoltaic distributed generation—An international review on diffusion, support policies, and electricity sector regulatory adaptation. *Renew. Sustain. Energy Rev.* **2019**, *103*, 30–39. [CrossRef]

37. BDEW. BDEW-Strompreisanalyse (Haushalte und Industrie). Available online: https://www.bdew.de/media/documents/190115_BDEW-Strompreisanalyse_Januar-2019.pdf (accessed on 28 January 2019).

38. Fraunhofer Institute for Solar Energy Systems (ISE). *Levelized Cost of Electricity Renewable Energy Technologies*; Fraunhofer Institute for Solar Energy Systems (ISE): Freiburg, Germany, 2018.

39. Stenzel, P.; Linssen, J.; Fleer, J.; Busch, F. Impact of temporal resolution of supply and demand profiles on the design of photovoltaic battery systems for increased self-consumption. In Proceedings of the 2016 IEEE International Energy Conference (ENERGYCON), Leuven, Belgium, 4–8 April 2016.

40. Talavera, D.L.; Nofuentes, G.; Aguilera, J. The Internal Rate of Return of Photovoltaic Grid-Connected Systems: A Comprehensive Sensitivity. *Renew. Energy* **2010**, *35*, 101–111. [CrossRef]

41. Tapia, M. Evaluation of Performance Models against Actual Performance of Grid Connected PV Systems. Master's Thesis, Carl von Ossietzky Universität, Oldenburg, Germany, 2014.

42. Fraunhofer ISE. *Recent Facts about Photovoltaics in Germany*; Fraunhofer Institute for Solar Energy Systems ISE: Freiburg, Gemmary, 2019.

43. Obane, H.; Okajima, K. Extracting issues significant to valuing electricity from small photovoltaic systems using quantitative content analysis. *Electr. J.* **2019**, *32*, 106673. [CrossRef]

44. Solar Power Europe. *Global Market Outlook for Solar Power 2018–2022*; Solar Power Europe: Brussels, Belgium, 2018.

45. Mubarak, R.; Hofmann, M.; Riechelmann, S.; Seckmeyer, G. Comparison of modelled and measured tilted solar irradiance for photovoltaic applications. *Energies* **2017**, *10*, 1688. [CrossRef]

46. Hofmann, M.; Seckmeyer, G. Influence of various irradiance models and their combination on simulation results of photovoltaic systems. *Energies* **2017**, *10*, 1495. [CrossRef]

47. Hofmann, M.; Seckmeyer, G. A New Model for Estimating the Diffuse Fraction of Solar Irradiance for PV System Simulations. *Energies* **2017**, *10*, 248. [CrossRef]

48. Seckmeyer, G.; Lagos Rivas, L.; Gaetani, C.; Heinzel, J.W.; Schrempf, M. Biologische und medizinische Wirkungen solarer Strahlung (Biological and medical effects of solar radiation). In *Promet, Heft 100 Strahlungsbilanzen*; Chapter 13; Deutscher Wetterdienst (DWD): Offenbach am Main, Germany, 2018.

49. Riechelmann, S.; Schrempf, M.; Seckmeyer, G. Simultaneous measurement of spectral sky radiance by a non-scanning multidirectional spectroradiometer (MUDIS). *Meas. Sci. Technol.* **2013**, *24*, 125501. [CrossRef]

4.4 Research Article D: Improving the Irradiance Data Measured by Silicon-Based Sensors

4.4.1 Declaration of my contribution

The author of this thesis conceived and designed the study and wrote the draft paper. The author also analyzed the data and performed the calculation used in this study. Holger Schilke contributed to the collection of the data, and supervised the measure-ments; Gunther Seckmeyer contributed to the conception and discussion of the data. All authors contributed to the final version of the manuscript.

4.4.2 Published article

energies

Article

Improving the Irradiance Data Measured by Silicon-Based Sensors

Riyad Mubarak *, Holger Schilke * and Gunther Seckmeyer *

Institute for Meteorology and Climatology, Leibniz Universität Hannover, Herrenhäuser Straße 2, 30419 Hannover, Germany
* Correspondence: mubarak@muk.uni-hannover.de (R.M.); schilke@muk.uni-hannover.de (H.S.); seckmeyer@muk.uni-hannover.de (G.S.)

Abstract: Silicon-based sensors are widely used for monitoring solar irradiance, in particular, in the field of Photovoltaic (PV) applications. We present a method to correct the global horizontal irradiance measured by silicon-based sensors that reduces the difference to the standard thermopile sensor measurements. A major motivation to use silicon-based sensors for the measurements of irradiance is their lower cost. In addition, their response time is much lower, and their spectral response is much closer to that of the PV systems. The analysis of the differences is based on evaluating four parameters that influence the sensor measurements, namely the temperature, cosine error, spectral mismatch, and calibration factor. Based on the analysis, a correction model is applied to the silicon sensors measurements. The model separates measurements under a clear sky and cloudy sky by combining the clearness index and the solar zenith angle. By applying the correction model on the measurements of the silicon-based sensor, the differences between sensor readings have been reduced significantly. The relative root mean squared difference (rRMSD) between the daily solar irradiation measured by both sensors decreased from 10.6% to 5.4% after applying the correction model, while relative mean absolute difference (rMAD) decreased from 7.4% to 2.5%. The difference in total annual irradiation decreased from 70 KWh/m^2 (6.5%) to 15 kWh/m^2 (1.5%) by the correction. The presented correction method shows promising results for a further improvement in the accuracy of silicon-based sensors.

Keywords: incident solar radiation; pyranometer; silicon sensors; solar reference cell

1. Introduction

Solar irradiance provides the energy that powers the earth's climate and biosphere. This energy is the primary source for many processes on earth, including processes that sustain living systems and circulation of the atmosphere and oceans [1]. This energy is also readily available for providing electricity and heat for industrial and domestic applications [2]. Accurate measurements of solar irradiance are needed for understanding the primary source of energy input to the earth–atmosphere–ocean system and for evaluation of photovoltaic (PV) power profiles [3]. Moreover, solar irradiance is the most important input parameter for PV software to predict the expected solar energy.

The global horizontal irradiance (GHI) is the most commonly measured component of solar radiation [4] and includes both direct beam and diffuse radiation. GHI is of particular interest to photovoltaic installations and is defined as the total solar radiation per unit area that is intercepted by a flat, horizontal surface.

Due to the increasing interest in solar energy and climate changes, solar irradiance measurements are gaining higher importance compared to recent years. According to IPCC [5], a small variation in solar irradiance can produce natural forcing of earth's climate with global and regional-scale responses. Therefore, accurate irradiance measurements are essential for the detection and attribution of climate change [6].

Instruments measuring solar irradiance may be classified as thermal sensors (thermopile pyranometers) and silicon-based (PV) sensors. Radiometers equipped with thermal sensors are widely used to measure broadband solar irradiance due to their nearly constant spectral response over the whole solar spectral range [7]. However, thermal sensors are costly in terms of hardware and calibration.

On the other hand, silicon-based radiation sensors provide the simplest and cheapest alternative. However, these sensors only respond to wavelengths between 300 and 1200 nm, and their spectral response within this interval is not uniform. The response to the red and near-infrared light is noticeably higher than for blue and ultraviolet light. This limited and non-uniform spectral response causes a spectral mismatch of the broadband irradiance measurement [8].

Many studies have highlighted the differences between both sensors and evaluated the uncertainties for solar radiation measurements. Understanding these differences is important because PV system performance analysis often depends on accurate solar irradiance data, and sensors of different technologies may be used. Dunn et al. [9] calculated typical measurement uncertainties for PV sensor and thermopile pyranometer measurements. The calculations were performed for a fixed-tilt system under clear sky conditions. They found the uncertainties in irradiance measurements to be in the order of $\pm 2.4\%$ for PV reference devices and $\pm 5\%$ for thermopile pyranometers. Meydbray et al. [10] considered the spectral effect and calculated the deviation of the two sensors in four different locations in the USA. They found that the daily solar irradiation deviation can amount up to 3% and that this deviation is highly variable over days, weeks, and months. Azouzoute et al. [11] compared the Plane of Array irradiance data, measured at a tilt plan of 32° by a first-class thermopile sensor and a reference PV cell. They found that the monthly deviation between the solar irradiation measurements from both devices ranges between -4.8% in June to -0.7% in December. Several researchers have developed correction methods that reduce the systematic errors of silicon sensors. The temperature correction is almost similar in all versions, while the methods used to correct the spectral effects vary between the publications. The corrections depend on the sensor temperature, the solar zenith angle (SZA), air mass (AM), diffuse horizontal irradiance (DHI), and global horizontal irradiance (GHI).

In the following, we present different approaches for spectral corrections. Alados-Arboledas et al. [12] used tabular factors for different sky parameters and a functional correction depending on the solar incidence angle. King and Myers [13] proposed functional corrections based on air mass and the angle of incidence derived for global irradiation. Vignola [14] further developed this approach and included diffuse and subsequently direct beam irradiance. Moreover, the German Aerospace Center (DLR) has developed a method using functional corrections, including a particular spectral parameter. The method was developed in 2003 and based on global, diffuse, and direct irradiance [15]. Forstinger et al. [16] suggested a new correction and calibration method based on a physical approach. The method aimed to remove the systematic errors and is based on information of the sensor properties, which includes its directional response and the site's atmospheric conditions.

This study aims to examine the differences in the readings of thermopile pyranometer and silicon sensor at a timescale of minutes, days, months, and years in Hannover. The goal is to evaluate the irradiance data from each sensor, identify contributing factors behind the variations between the readings, and create simple empirical correction methods that require a minimum number of inputs to improve the silicon sensor measurements and reduce the differences between both sensors.

2. Instruments

The measurement system installed on the rooftop of IMUK consists of different meteorological and radiation instruments. The systems have been described shortly in Mubarak et al. [17,18]. We will focus only on the irradiance devices, as their data will be used in this work, namely the thermopile pyranometers and silicon-based sensors.

2.1. Thermopile Pyranometer

Pyranometers are broadband instruments that measure global solar irradiance received from the whole skydome (2 Ω solid angle). Besides global irradiance, pyranometers can also measure diffuse irradiance. For this, a small shading disk can be mounted on an automated solar tracker. Alternatively, a shadow ring may prevent the direct component from reaching the sensor the whole day. The International Standard [19] and the World Meteorological Organization (WMO) distinguishes three classes of pyranometers based on performance characteristics and specifications: the best class is called secondary standard, the second-best is called first class, and the third is called second-class. The thermopile sensors used in this study are CMP11 pyranometers from Kipp & Zonen [20] (hereafter referred to simply as Pyr). The sensors were used to measure GHI and DHI.

A typical pyranometer (Figure 1) consists of a black-painted disk (detector) sealed by two glass domes, which protect the sensor from thermal convection and weather threat (e.g., rain and wind). The double glass domes also limit the instrument's spectral sensitivity in the wavelength range between 280 nm and 2800 nm and usually have a bubble for silicon-based. Moreover, the specially designed double glass domes also produce a more accurate angular response in the instrument and reduce thermal losses [21].
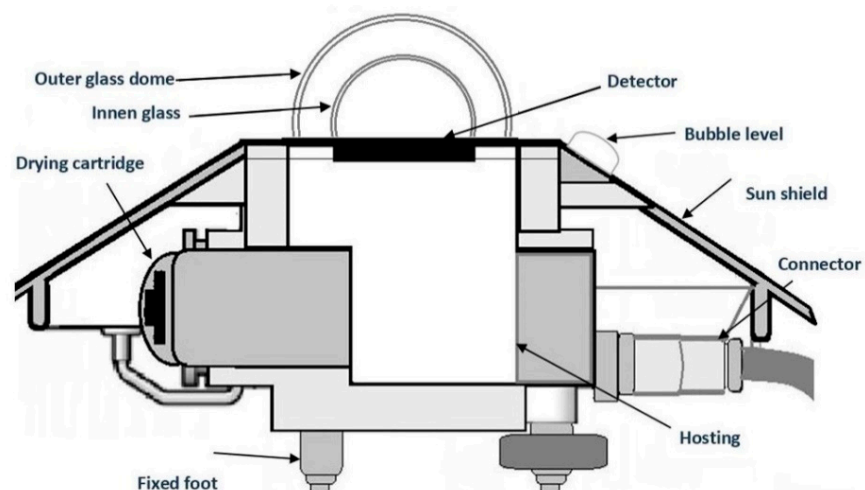

Figure 1. Thermopile Pyranometer.

2.2. Silicon Sensors

During the last decade, silicon-based sensors have been used as low-cost radiation instruments to monitor PV plants [22]. Silicon-based sensors have a similar spectral response (300–1200 nm) as a solar panel. As a result, silicon sensors provide a more accurate representation of the energy available for conversion to electricity by a solar panel at a tenth of the cost of a thermopile pyranometer [23]. In general, there exist two main types of silicon sensors to monitor PV solar systems, specifically silicon-photodiode pyranometers and reference solar cells. A photodiode-based pyranometer essentially monitors the short circuit current of a solar cell under a diffusing lens. The pyranometer body and diffusing lens are designed to minimize deviations from a true angular response [22]. However, the irradiance values indicated by these pyranometers, without correction, may differ from the "true" broadband solar irradiance by over 10% [24].

Unlike photodiode-based pyranometers, reference cells do not contain a diffuser; they have glazing, which allows as much of the incident solar radiation as possible to pass inside, such as PV modules (see Figure 2). Reference solar cells are expected to have a similar spectral response as photodiode-based pyranometers since photodiodes and reference cells are both solar cells for which the output is monitored in a short circuit configuration [21].

Generally, reference cells have an internal temperature measurement that can be used to adjust the temperature dependence of the measured irradiance.

Silicon sensors used in this research are monocrystalline solar cells from Ingenieurbüro Mencke and Tegtmeyer (IMT) [25] (hereafter referred to simply as SiS). The solar cells are in an aluminum casing with a glass cover and a Pt100 temperature sensor to measure the cell temperature. According to manufacturer specifications, the sensor's reading should agree within 5% with the thermopile pyranometer's reading within an ambient temperature between -20 to 70 °C and normal incident irradiance.
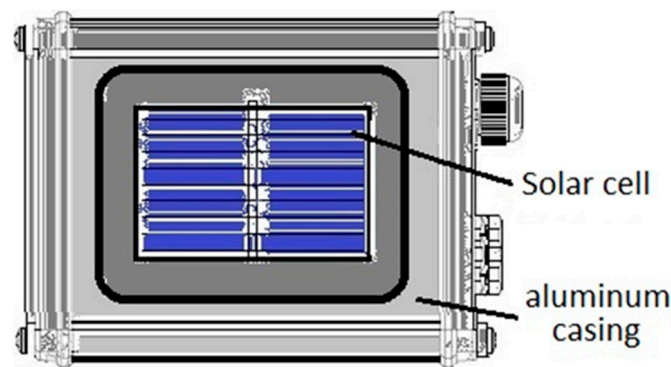

Figure 2. Silicon sensor (SiS) from IMT [26].

Measurements of both sensors were carried out from January 2016 to December 2019. The data were stored in data loggers. The loggers recorded all data, such as irradiation and temperature, from the sensors every one minute. In the following, the main differences between sensors will be discussed.

2.3. Differences between Sensors

As explained above, both sensors demonstrate differences in the used technology, measuring principle, and reactions to incident solar irradiance, as well as making differences in measured irradiance (Table 1). The main differences between the sensors will be further demonstrated and discussed.

Table 1. Analysis of the differences between sensors (linear calibration, offset, spectral response, angular response according to the manufacturers [20,25]).

Specifications	CMP11	Si-mV-85
Spectral sensitivity range (nm)	285–2800	360–1200
Response time (s)	<5	<0.001
Offset (W/m^2)	<2	0
Temperature dependence (-20–40 °C) (%)	<1	0.2
Uncertainty (W/m^2)	<5	± 5
Non-linearity (100 to 1000 W/m^2) (%)	<0.2	± 0.1
Angular response (% up to 80° SZA)	<1	<30

2.3.1. Temperature Response

The influence of temperature on the irradiance sensor signal is lower in thermopile pyranometers [26,27] than in silicon devices [13,28]. The different reaction of sensors to temperature is due to the different measurement principle. In the case of silicon-based sensors, the temperature affects the short circuit current of monocrystalline silicon cells; it records higher values at higher temperatures [29]. The used silicon sensors do not have a temperature compensation that reduces temperature dependence. Accordingly, the temperature change during the measurements should be taken into account and corrected. The

available SiS have internal temperature sensors that can be used to adjust the temperature dependence of the measured irradiance.

2.3.2. Spectral Response

The spectral response (SR) describes the sensor's sensitivity to radiation of different wavelengths. As defined, thermopile pyranometers measure solar irradiance within a wide wavelength range (290–2800 nm). Unlike thermopile pyranometers, silicon sensors do not respond to all incident wavelengths equally. Thus, they have a non-flat spectral response (Figure 3). The SR of silicon describes how well a material can utilize the light of a specific wavelength to generate an electric current. The SR of a silicon-based sensor has an upper limit of approximately 1200 nm, which is mainly determined by the spectral response of the used PV material. The spectral response of the used SiS has been shown in previous work [17].
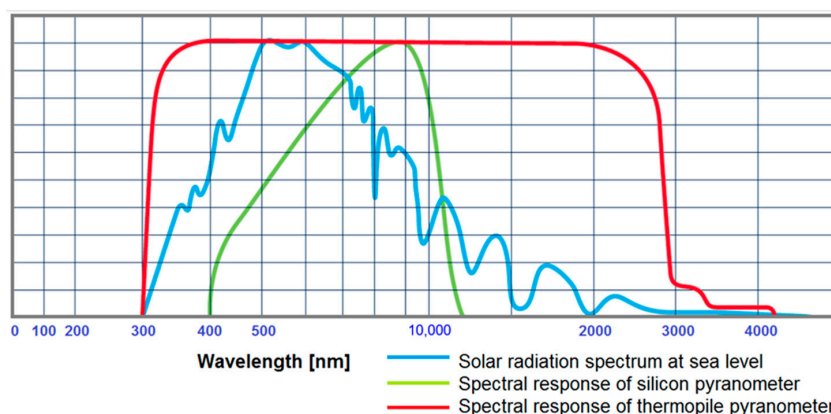

Figure 3. Spectral response curves of silicon, thermopile pyranometers, and solar spectrum at sea level [20].

2.3.3. Angular Response

The angular "cosine" response reflects the fact that the response of the irradiance sensor varies with the angle of incidence [30]. Global irradiance is measured with instruments assumed to have a true angular response. However, we know from different studies [31–33] that no instrument is perfect in this regard. The deviation of global irradiance measurements from the ideal cosine law is known as cosine error. The angular response of thermopile pyranometers is determined by the glass domes and the spectral and spatial uniformity of the thermopile detector. The used thermopile pyranometer has a good angular response, where the maximum deviation from the ideal angular response is less than 10 W/m^2 (up to an incidence angle of 80°) with respect to 1000 W/m^2 irradiance at normal incidence (0°) [34].

The angular response of a silicon sensor can be described as the reduction in sensor output when solar radiation impinges at angles deviating from the normal to the surface. This deviation affects the calibration of sensors and introduces energy losses in photovoltaic conversion. King et al. [13] attributed this decrease to two sources: The first one is a geometrical factor (cosine law). The second source results from the optical properties of the used sensor, primarily from the reflectance of input optics. The influence of incidence angle on the SiS response is shown in Figure 4. With an increasing incidence angle, the relative deviation rises significantly.
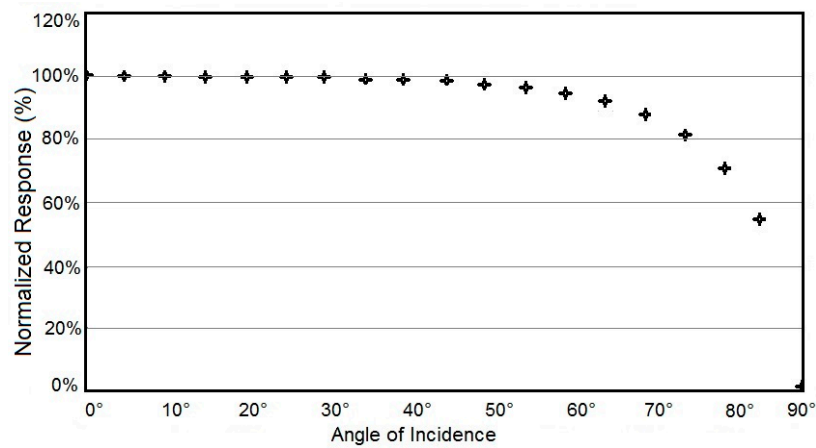
Figure 4. Normalized angular response of SiS versus solar angle-of-incidence measured by the manufacturer [25] under STC.

Figure 5 shows the difference between GHI measured by the Pyr and that measured by the SiS under a clear sky and overcast conditions. Under clear sky conditions, the Pyr measured higher irradiance, and the difference between both sensors increases in the morning and evening hours when the solar zenith angle is high. This may mainly be due to the higher cosine error of the used SiS.
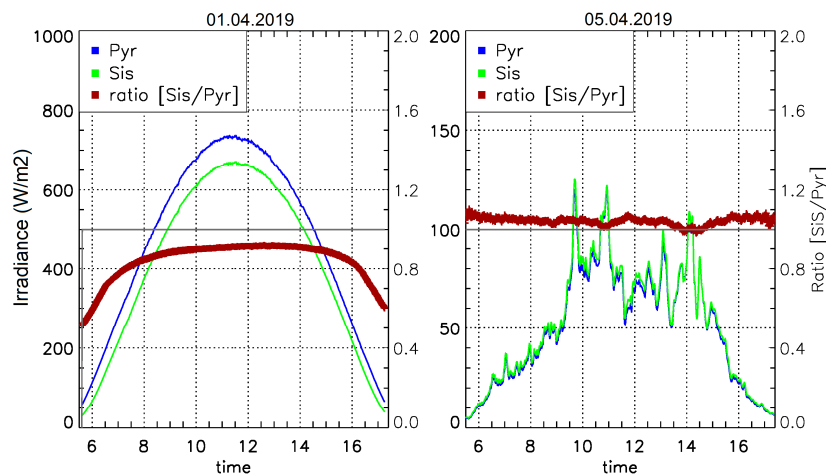

Figure 5. GHI measured by SiS on an overcast day (5 April 2019, **right**) and on a clear sky day (1 April 2019, **left**) and the ratios (SiS/Pyr). Under clear sky conditions, Pyr measured higher than SiS; the difference between sensor increased in the morning and evening hours. The sensitivity of the SiS increased under cloudy conditions due to the change in the spectral distribution of incident diffuse radiation.

Once the sun is totally covered by clouds and the present irradiance is only diffuse, the sensitivity of the SiS increases compared to calibration conditions. The SiS measures a higher solar irradiance than Pyr, which has nearly constant spectral sensitivity over the complete solar spectrum. This result confirms that the spectral distribution of incident solar irradiance significantly impacts the irradiance measured by silicon-based sensors.

It is also worth investigating the influence of these differences between the sensors on the monthly and annual irradiation. Figure 6 shows the average total monthly and annual uncorrected global horizontal irradiation (2016–2019) measured by both sensors.

GHI measured by the thermopile pyranometer was overall higher than the SiS irradiance. The monthly differences ranged between 3.7% in July and 17.1% in January. The annual Pyr irradiation was 6.5% higher.
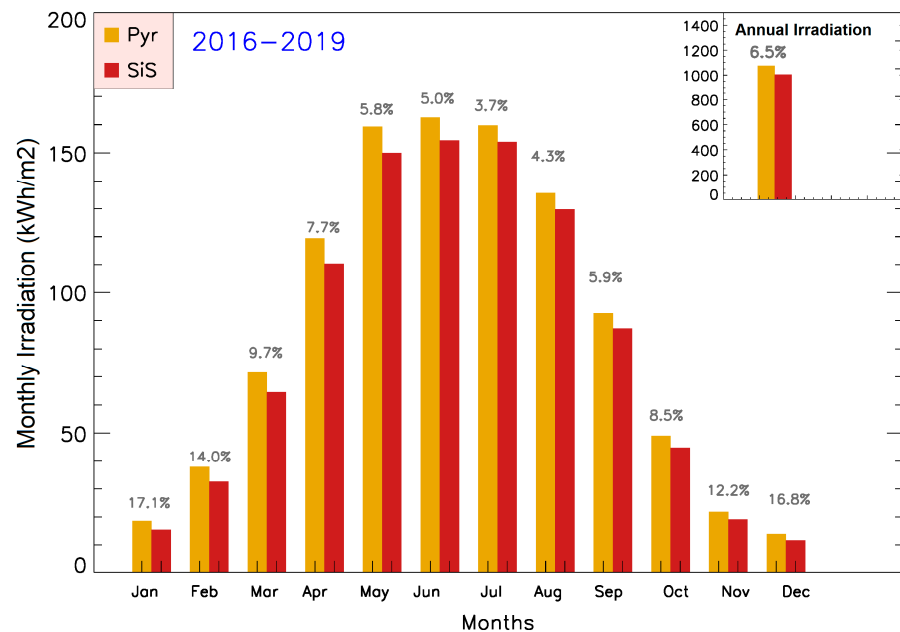

Figure 6. Monthly and annual global irradiation measured by both SiS and Pyr (2016–2019) and the percentage difference between them. The graphics show remarkable variation in monthly irradiation.

The results demonstrate that both sensors measure close to each other. The difference between their readings is minimal during summer months (when solar irradiance level around midday is close to STC value). Once the solar elevation angle decreased in winter months and accordingly, the solar irradiance was lower compared to the STC value, the SiS measured lower than Pyr, and the difference between the sensors was higher. This result agrees with the results achieved in [17].

3. Methods

3.1. Measurement Site

The measurements, which this work is based on, were performed over the course of four years (January 2016–December 2019) on the roof of the Institute for Meteorology and Climatology (IMuK) of the Leibniz Universität Hannover (Hannover, Germany; 52.23° N, 09.42° E and 50 m above sea level). To better evaluate the results, it is necessary to give an overview of the prevailing solar radiation conditions in the measurement site. According to the German Weather Service (DWD), the average annual global horizontal irradiation in Germany (1981–2010) ranges between 951 kWh/m^2 and 1257 kWh/m^2 [35]. Solar radiation in Hannover as a north German city is close to the minimum value, representing a low radiation climate in this region. Ground measurements for GHI at IMUK in the last ten years (2010–2019) showed that the global irradiation ranged between 989 kWh/m^2 and 1162 kWh/m^2 (Figure 7, upper graphic). The results were within the range of DWD.
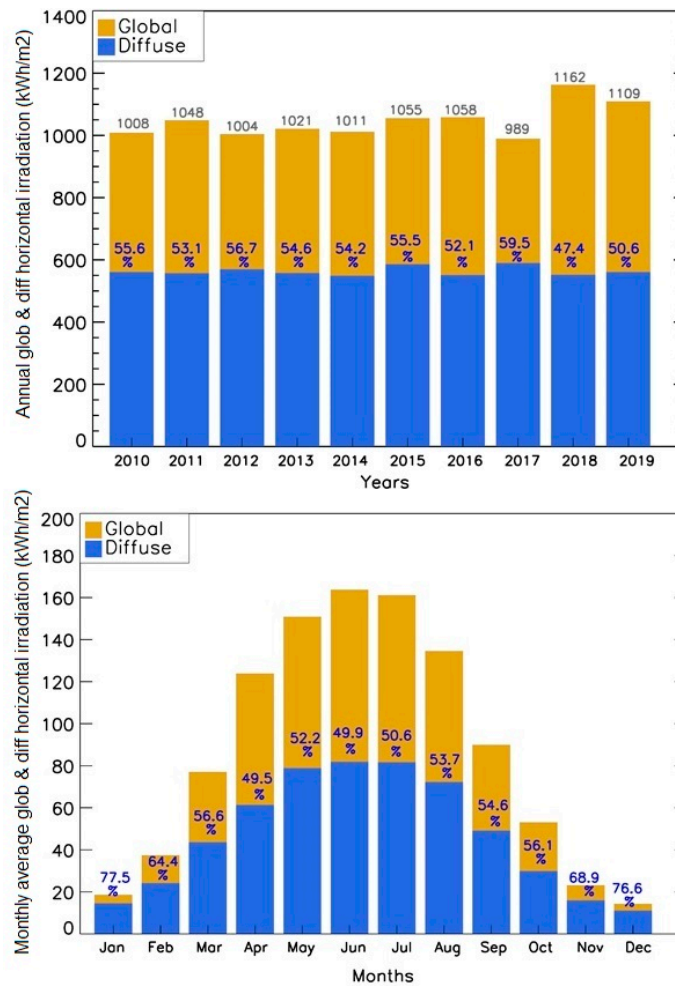
Figure 7. Annual global and diffuse horizontal irradiation in Hannover, measured from 2010 to 2019 (**upper** graphic), and monthly average values, measured in the same period (**lower** graphic). The measurements were performed on the roof of the IMuK by thermopile pyranometers.

The lower graphic of Figure 7 shows the monthly average of global- and diffuse horizontal irradiation in Hannover within the last ten years. GHI had its maximum in June due to the height of the sun and sunshine duration in this month compared to other months. It can be seen that the lowest irradiation values were registered in the winter months when the sunshine duration at its minimum. The monthly average in the summer months was eight to nine times higher than in the winter months. The sun's height is not the main factor that determines the amount of diffuse irradiance, but the atmospheric conditions in the measurement location play an essential role. The monthly diffuse irradiation makes up about half of the global irradiation during summer months and more than two-thirds of global irradiation in winter months. These values can give an idea about the solar radiation climate of Hannover. The big difference between summer and winter irradiation and the distribution of diffuse radiation over the year influences the tilt angle and orientation at which the maximum annual solar radiation is collected.

3.2. Correction Model

One of the aims of this work is to improve the SiS solar irradiance measurements and reduce the difference to the thermopile sensor. Therefore, we proposed a set of correlations

and equations as a correction model to improve the measured SiS-irradiance and to approach the reading of Pyr. The model addressed the main measurement uncertainties that the SiS suffers from in relation to the thermopile pyranometer. The temperature correction was first applied to correct the temperature error caused by changing temperatures during the measurements and the deviation from the STC value. The model started with this correction because the temperature correction depends only on sensor temperature, regardless of sky conditions (clear or cloudy). In the second step, the clear sky data was separated from cloudy-sky conditions using the clearness index (K_t) and SZA. Then cosine, spectral, and calibration corrections were applied according to sky conditions. Figure 8 shows a block diagram of the calculation process of the model.
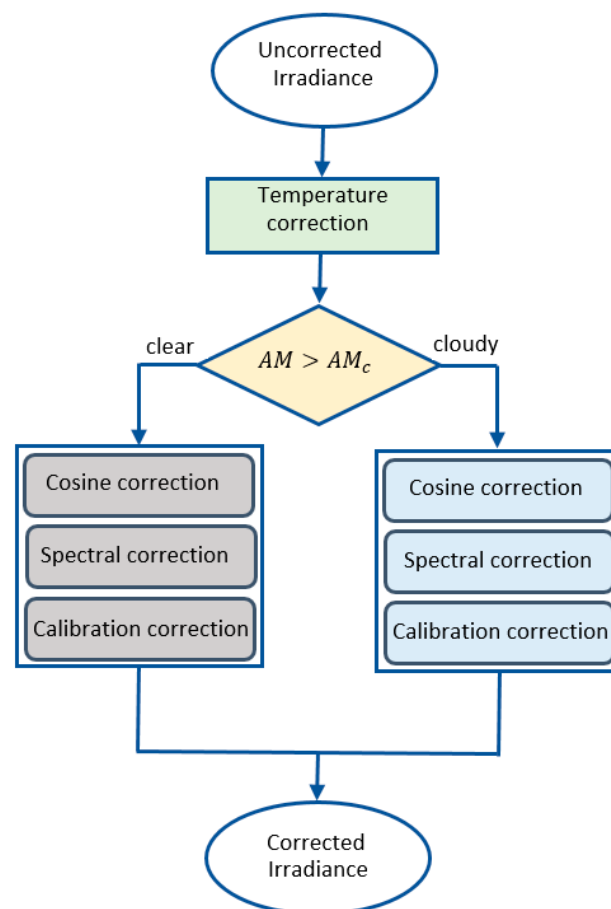
Figure 8. Block diagram of the correction steps in the correction model.

3.2.1. Temperature Correction (C_T)

The daytime temperature of SiS as a reference PV cell differs from the ambient temperature since cells are dark in color and accordingly absorb a greater amount of solar energy [36]. During the day, the silicon sensor becomes hotter than the ambient temperature by a factor that depends on incident solar irradiance. It is known that the short circuit current (I_{sc}) increases with increasing cell temperature [36]. The used silicon sensors operate next to a short circuit [25], and accordingly, the sensor's sensitivity increased as the temperature increase. The influence of temperature on a sensor's response is usually corrected using a temperature coefficient α, which represents the change in I_{sc} with temperature changes related to the temperature value under STC. A typical value of the temperature coefficient for a crystalline silicon (c-Si) PV device is 0.05%/°C [37]. The

temperature coefficient is considered by the manufacturer (IMT), and the correction is done according to Equation (1):

$$(SMM, CosEr, Cf) = \frac{E(T_d, \; SMM, CosEr, Cf)}{1 + \alpha(T_{sen} - 25°C)} \tag{1}$$

where $E(T_d,SMM,CosEr,Cf)$ and $E(SMM,CosEr,Cf)$ are the SiS Irradiance before and after applying the C_T, T_{sen} is the sensor temperature measured by the integrated Pt100 temperature sensor that was mounted to the back of the sensor, and α represents the temperature coefficient (0.05%/°C). The C_T depends only on the sensor's temperature, and therefore, the same correction can be applied to the SiS measurements under all weather conditions.

In the next step, the model separated the clear sky from cloudy measurements. In this work, a combination of the clearness index (K_t) and the SZA was used to separate the clear sky measurements from those measured under cloudy conditions. Figure 9 shows the change in (K_t) with SZA for clear sky and cloudy global irradiances.

$$K_t = \frac{E}{E_0} \tag{2}$$

where E_0 is the extraterrestrial irradiance, and E is the measured global irradiance.
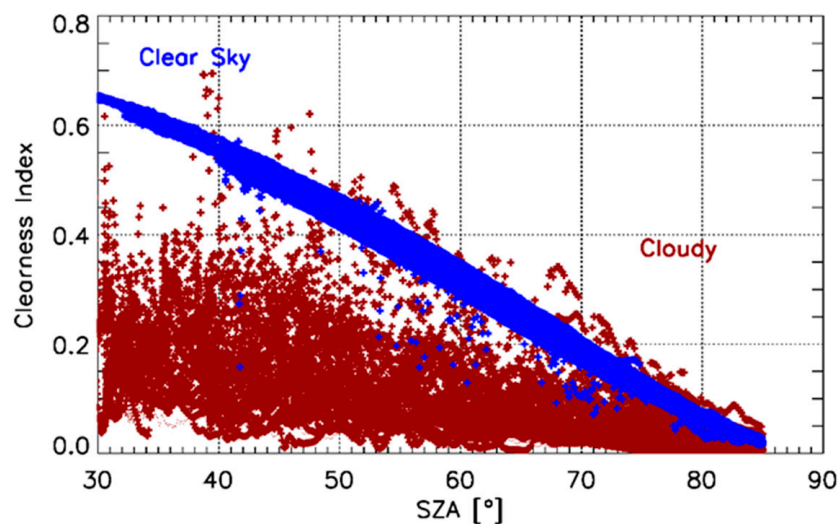
Figure 9. Change in clearness index (K_t) with SZA for clear sky measurements (**blue**) and measurements under cloudy conditions (**brown**) for the year 2019. The clear sky global irradiance has different values of K_t than cloudy measurements under the same SZA.

The extraterrestrial irradiance was calculated as described by Duffie and Beckman (1980) [1]. The values of K_t were different in both cases for the same SZA. We used these differences in the clearness index for each SZA range to separate the clear sky irradiance from those measured under cloudy conditions. Therefore, we defined a critical clearness index value (K_{tc}) for every SZA-range according to Table 2.

Table 2. Separation clear sky global irradiance ($K_t > K_{tc}$) from which measured under cloudy conditions.

| SZA Range	Clearness Index
$40° > $ SZA	$K_t > 0.50$
$40° < $ SZA $< 50°$	$K_t > 0.40$
$50° < $ SZA $< 55°$	$K_t > 0.30$
$55° < $ SZA $< 60°$	$K_t > 0.27$
$60° < $ SZA $< 65°$	$K_t > 0.20$
$65° < $ SZA $< 70°$	$K_t > 0.15$
$70° < $ SZA $< 75°$	$K_t > 0.10$
$75° < $ SZA $< 80°$	$K_t > 0.05$
$80° < $ SZA $< 82°$	$K_t > 0.04$
$82° < $ SZA $< 84°$	$K_t > 0.02$
$84° < $ SZA $< 85°$	$K_t > 0.015$

3.2.2. Cosine Correction (C_c)

Cosine error affects mainly the beam irradiance, while diffuse irradiance has less dependence on SZA. Accordingly, the correction model treated the measurement data differently according to sky conditions. The SiS angular response that was measured in the laboratory of manufacture (Figure 3) was used to correct the clear sky global irradiance. In the case of cloudy days, GHI was corrected for the CosEr using a correction factor, which was obtained as a fit function through empirical measurements. The ratio (E_{SiS}/E_{Pyr}) vs. the SZA is plotted (Figure 10), and a polynomial fitting to the cloudy irradiance tendency was obtained and used to correct the GHI measured in cloudy days according to Equation (3).

$$E(SMM, Cf) = \frac{E(CosEr, SMM, Cf)}{-0.0000007(SZA)^3 + 0.00006(SZA)^2 - 0.0009(SZA) + 0.9856}$$ (3)

where E(CosEr,SMM,Cf) and E(SMM,Cf) are the solar global irradiance before and after applying cosine correction.
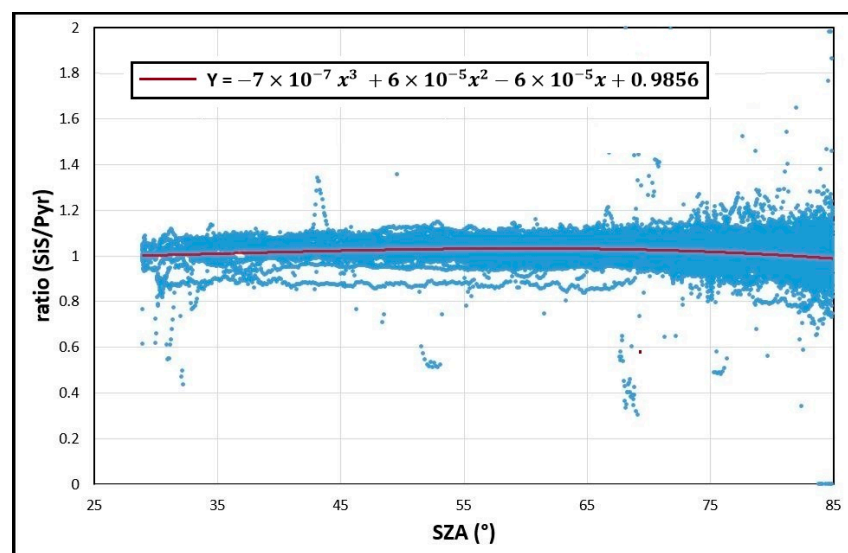
Figure 10. The ration (E_{SiS}/E_{pyr}) under cloudy conditions plotted against SZA. The red line represents the polynomial fit equation of cloudy data.

3.2.3. Spectral Mismatch Correction (C_s)

The spectral distribution of the incident solar irradiance varies during the day, and it is also affected by the atmospheric conditions. As a result, it is generally different from the STC spectrum (AM1.5). These spectral mismatches lead to a measurement uncertainty sometimes noted as spectral mismatch error that is quantified by the spectral mismatch factor (SMM) [38]. The SMM depends on the semiconductor materials used in PV sensors and the atmospheric conditions in terms of cloud cover and aerosol content [13,39]. The spectral distribution of the beam irradiance differs from that of the diffuse irradiance. Accordingly, spectral mismatch affects both irradiance components differently. The model treated the spectral mismatch of clear sky measurements in a way that differed from cloudy conditions.

One way to determine the magnitude of SMM of the sensor under clear sky conditions is to measure the spectral distribution over the day and compare it to the AM1.5 spectral distribution that is used for the calibration. The air mass is calculated using the formula of Kasten and Young [40]. Due to the unavailability of simultaneous spectral measurements, we calculated the spectral irradiance in this work using the UVSPEC model in the Libradtran package [41,42]. As an input parameter, horizontal visibility of 20 km, perceptible water of 15 kg/m^2, an albedo of 0.02, and a total ozone column of 300 DU were used (Figure 11, left). First, the pyranometer irradiance (E_{Pyr}) was calculated, and then the SiS irradiance (E_{SiS}) was determined according to Equations (4) and (5). Then the spectral irradiances at AM1.5 were calculated and used as reference values for both sensors ($E_{Pyr.cal}$, $E_{SiS.cal}$). The spectral mismatch factor was calculated according to Equation (8),

$$E_{Pyr} = \int_{285}^{2800} E(\lambda) d\lambda \tag{4}$$

$$E_{SiS} = \int_{360}^{1200} E(\lambda) SR(\lambda) d\lambda \tag{5}$$

$$E_{Pyr.cal} = \int_{285}^{2800} E_{AM1.5}(\lambda) d\lambda \tag{6}$$

$$E_{SiS.cal} = \int_{360}^{1200} E_{AM1.5}(\lambda) SR(\lambda) d\lambda \tag{7}$$

$$\text{SMM} = \frac{\int_{360}^{1200} E(\lambda) SR(\lambda) d\lambda \cdot \int_{285}^{2800} E_{AM1.5}(\lambda) d\lambda}{\int_{285}^{2800} E(\lambda) d\lambda \cdot \int_{360}^{1200} E_{AM1.5}(\lambda) SR(\lambda) d\lambda} \tag{8}$$

where, $E_{AM1.5}$ is the spectral irradiances at AM1.5.

The corrected irradiance was then calculated by dividing the uncorrected value by the SMM:

$$E(Cf) = \frac{E(SMM, Cf)}{SMM} \tag{9}$$

where *E(SMM,Cf)*, *E(Cf)* are the solar irradiance before and after applying the spectral correction.

For cloudy days, the SMM was obtained as a fit function through empirical measurements. The ratio (E_{SiS}/E_{Pyr}) vs. the air mass is plotted in Figure 11 (right), and a polynomial fitting to the cloudy irradiance tendency was obtained and used to correct the GHI measured in cloudy days according to Equation (10).

$$E(Cf) = \frac{E(SMM, Cf)}{\left(0.0029(AM)^2 - 0.0001\,(AM) + 1.0144\right)} \tag{10}$$
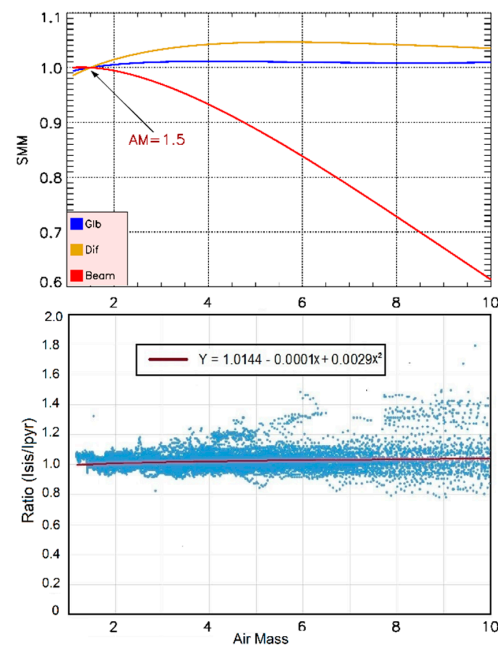
Figure 11. The spectral mismatch factor SMM for global, diffuse, and beam irradiances plotted against AM (upper graphic). The calculations were based on the radiative transfer model libRadtran under clear sky conditions. Lower graphic shows the ratio (E_{SiS}/E_{Pyr}) under cloudy conditions plotted against AM. The red line represents the polynomial fit equation for cloudy data.

It is essential to refer here that the SMM may be strongly influenced by the atmospheric conditions and the PV semiconductor materials [39].

3.2.4. Calibration Correction (C_{cal})

The calibration of silicon sensors was carried out under STC: 1000 W/m^2 of irradiance, AM1.5 spectrum, and 25 °C of cell temperature. In fact, these reference conditions were hardly obtainable in the outdoor measurements as they combined the irradiance of a clear summer day with the sensor temperature of a clear winter day and the spectrum of a clear spring day. Operating the sensors under real atmospheric conditions that deviate from the STC introduces a calibration error. This deviation depends on the real atmospheric conditions that were changing continuously, making the exact evaluation of the error more complicated. We calculated the calibration deviation factor for both clear and cloudy conditions differently in this work. The most influential parameter that affected the calibration factor's magnitude was the solar irradiance prevailing in the field. Calibration factor correction for clear sky conditions (Cf-cl) was calculated by comparing the irradiance measured by both sensors around noontime (about ± 60 min). The calculations were performed after applying the temperature, cosine, and spectral mismatch corrections.

The calibration correction factor (C_{cal}) was calculated by plotting the ratio (E_{SiS}/E_{Pyr}) vs. the SZA_{min} (as the irradiance is maximum) and obtaining the correlation equation as a linear fit. The obtained equation was then multiplied by SiS irradiance according to Equation (11):

$$E_{corr} = E(Cf - cl) * (0.0009(SZA_{min}) + 1.0005) \tag{11}$$

where *E(Cf-cl)*, E_{corr} are the solar irradiance before and after applying the calibration correction for clear sky measurements and SZA_{min} is the minimum daily SZA value.

In the case of cloudy conditions, there was, unfortunately, no reliable cloudy diffuse reference to which the measurements could be compared. Thus, the calibration factor was obtained as a fit function through empirical measurements. The ratio (E_{SiS}/E_{Pyr}) vs.

the SZA was plotted (after applying the other corrections), and a correlation equation was applied as a correction factor to correct the GHI measured under cloudy conditions Equation (12).

$$E_{corr} = \frac{E(Cf - cd)}{(0.0006(SZA) + 0.969)} \tag{12}$$

where *E(Cf-cd)*, (E_{corr}) are the overcast irradiance before and after applying calibration correction.

4. Results and Discussion

This section presents the results of applying the correction model on SiS measurements. We will start by investigating the effect of individual corrections, namely temperature, cosine, spectral, and calibration corrections, as well as evaluating the magnitude of each correction on the measured irradiance. Finally, we apply all corrections on the SiS measurements and compare them to the Pyr irradiance before and after applying the corrections.

Figure 12 describes the influence of individual correction factors on the measured SiS irradiance for two clear sky days. The two case-study days on 29 June (upper graphic) and 16 April (lower graphic) were chosen to investigate the influence of the model on clear sky conditions in different temperatures and solar heights. The value of temperature correction affected the measured irradiance according to sensor temperature with relation to calibration value (green curve). When sensor temperature exceeded the calibration value (25 °C), the SiS measured higher values than it should be, and then the purpose of C_T was to reduce the SiS irradiance.

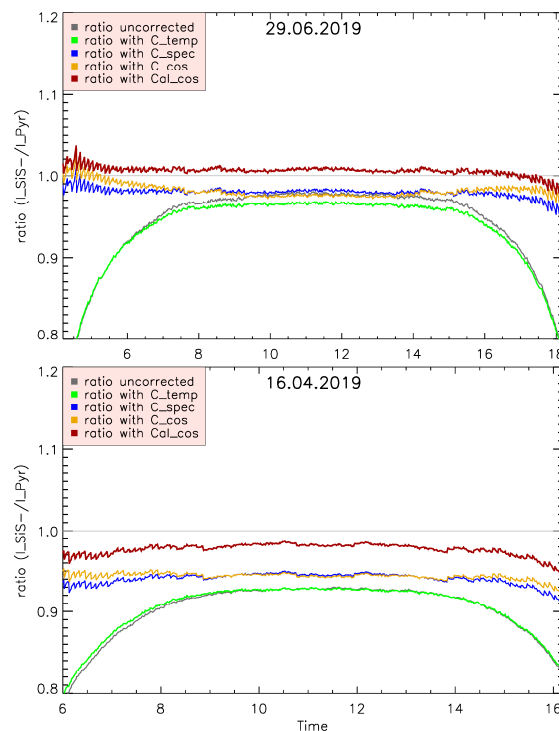**Figure 12.** The daily curve of the ratio (E_{SiS}/E_{Pyr}) for two clear sky days (16 April 2019, 29 June 2019) before (gray) and after applying each step of the correction model. The corrections were applied to the raw data one after another. First, the temperature correction was applied (green), then cosine correction (gold), then spectral correction (blue), and finally, the calibration correction (brown).

The reduction had its maximum at about noon when the irradiance and thus the temperatures were at maximum. The influence of C_T decreased with increasing SZA, where the temperatures decreased. Once the temperature was below 25 °C, C_T had an increasing influence on SiS irradiance (Figure 10, right).

Due to a large cosine error of the used silicon sensors, the cosine correction played the greatest role in correcting the SiS irradiance (golden curve). The losses of SiS irradiance due to cosine error were the highest under clear sky conditions, as shown in Figure 12. C_c increased the SiS irradiance depending on the SZA, and its influence was strongest in early mornings and late afternoons.

The blue curve shows the influence of spectral mismatch correction on the SiS irradiance after applying the temperature and cosine corrections. C_s increased the SiS irradiance as long as the AM was below the calibration value (AM1.5). Once the air mass exceeded 1.5, the path of solar radiation through the atmosphere was longer, and the incident radiation contained more red light. Accordingly, the response of SiS irradiance increased compared to STC, and then the purpose of C_s was to decrease the SiS irradiance. Therefore, the blue curve on both days under study lay above the golden curve around noontime (Am < 1.5) and lay below in the morning and evening hours (Am > 1.5). In general, the spectral mismatch showed seasonal variation depending on the semiconductor material of the sensor [2]. The spectral effect of the SiS (C-si) was smaller, and there was a small seasonal variation [2,3]. Applying the correction model on the SiS measurements under clear sky conditions increased the SiS irradiance (independent of the time of the day) and thus decreased the difference to the Pyr irradiance.

The influence of the correction model on the monthly and annual values is shown in Figure 13. The deviation of the SiS irradiation from the Pyr values decreased significantly after applying the correction model on the SiS measurements. The differences in total annual irradiation decreased from 70 KWh/m² to 15 kWh/m² with the correction.
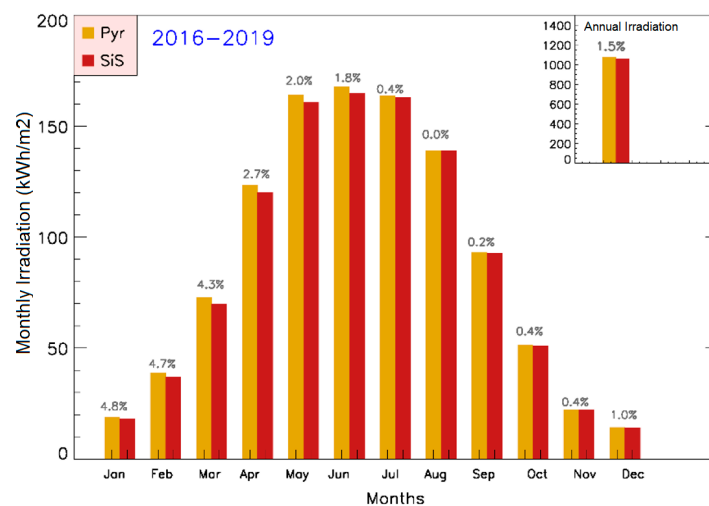
Figure 13. Monthly and annual differences between SiS and Pyr GHI (2016–2019) after applying the correction model on SiS measurements. The differences between the sensor readings decreased significantly after the correction. The difference in total annual irradiation between the sensor readings decreased from 6.5% to 1.5%.

The ability of the model to decrease the difference between the sensors under cloudy conditions was limited due to the anisotropic distribution of sky radiation and a combination of multiple influencing factors. Figure 14 shows the results of applying the correction model on an overcast day, 16 September 2019. It can be seen that the temperature and cosine corrections had a small increasing influence on the SiS irradiance due to the low

sensor temperature (below 25 °C) and the cosine error of the sensor. On the other hand, the spectral correction decreased the irradiance due to the high AM values. However, applying the model to the measurements decreased the SiS irradiance and reduced the difference to the Pyr irradiance.

Figure 14. The daily curve of the ratio (E_{SiS}/E_{Pyr}) for an overcast day (16 September 2019) before (**gray**) and after applying each step the correction model. First, the temperature correction was 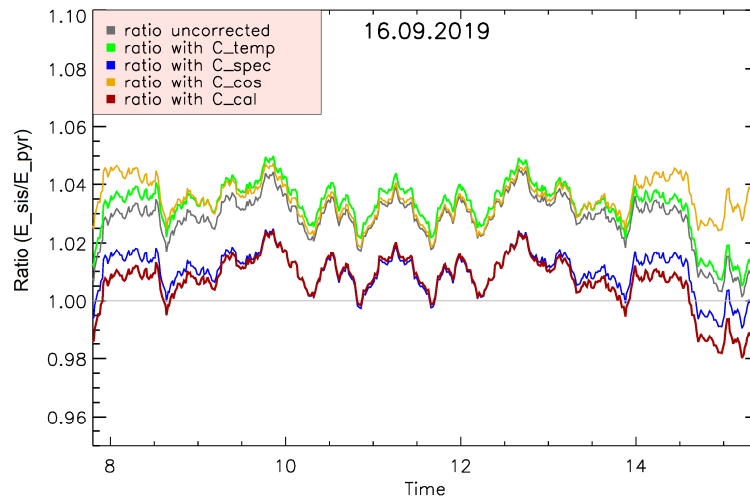applied (**green**), then cosine (**gold**) and spectral correction (**blue**), and finally the calibration correction (**brown**).

The ability of the correction model to correct the GHI measured by the SiS was also analyzed by means of the relative Root Mean Square Difference (rRMSD) and relative Mean Absolute Difference (rMAD). Table 3 shows the average deviation of the sensors' readings after each correction step. The rRMSD of daily irradiation between SiS and Pyr decreased from 10.6% to 5.4% after applying the correction model, while the rMAD values decreased from 7.4% to 2.5%.

Table 3. Statistical indices of the daily irradiation after each correction step, compared to Pyr measurements.

	Ucalb	C_T	C_c	C_s	C_{Tcal}
rRMSD (%)	10.6	10.8	7.5	7.6	5.4
rMAD (%)	7.4	7.6	4.7	4.8	2.5

5. Conclusions

In this work, we focused on the differences between two of the commonly used solar sensors: thermopile pyranometer and silicon-based sensor. These sensors were different in the used technology, measuring principle, and responses to incident solar irradiance. Therefore, the values of irradiance measured with these sensors were different. We aimed to analyze these differences in order to propose a method to improve the SiS measurements by minimizing the difference between SiS and Pyr readings using the minimum number of input parameters. Reducing the errors of silicon-based sensors can open a new avenue for using these sensors as low-cost irradiance sensors. We discussed four parameters that influence the sensor measurements, namely the temperature, cosine error, spectral mismatch, and calibration factor. In order to eliminate the uncertainty caused by these parameters, a correction model based on the analysis was applied to SiS measurements.

Applying the temperature correction on the SiS measurements increased the measured value of irradiance in the winter months when the cell temperature was below the calibration value (25 °C). On the other hand, the correction caused a decrease in the measured value of SiS irradiance on hot days when cell temperatures were above 25 °C.

In comparison to temperature and spectral corrections, the effect of cosine error correction on the SiS irradiance was greater due to a large cosine error of the silicon sensors under investigation for SZAs larger than 60°, which is shown in Figure 12. The influence of this correction appeared to be more marked at sunsets and sunrises of clear sky days. Cosine error affects mainly the beam irradiance, while diffuse irradiance had less dependence on SZA.

Spectral mismatch correction increases or decreases the SiS irradiance, depending on the air mass with respect to the AM1.5 spectrum used in STC. For AM values below AM1.5, the correction increased the SiS irradiance. For air mass higher than AM1·5, the spectral distribution of the global solar irradiance changed in favor of the spectral response of SiS. Accordingly, the correction decreased the measured SiS irradiance (Figure 12, blue curve). The spectral mismatch and the spectral correction were strongly influenced by the used PV material and atmospheric conditions.

The model applied as a last correction the calibration factor correction that stems from calibration of SiS under STC, which deviated from the real atmospheric conditions. The magnitude of this correction in clear sky days depends on the solar irradiance; its value is greater in winter months than in summer months. This correction increased the SiS irradiance in clear sky conditions by 2–5% and decreased by up to 3% for overcast conditions.

As a result of applying the correction model on the GHI of SiS, the differences between the values measured with both sensors were reduced significantly. The daily rRMSD between SiS and Pyr irradiances decreased from 10.6% to 5.4% after applying the correction model, while the rMAD decreased from 7.4% to 2.5%.

The differences in the total annual GHI decreases from 70 KWh/m^2 (6.5%) to 15 kWh/m^2 (1.5%) by the correction.

The model was used to correct the GHI measurements. The accuracy of the model for correcting tilted irradiance was not tested due to the unavailability of thermopile measurements on inclined surfaces. However, we assumed that this model can be used to correct the SiS irradiance measured on tilted surfaces. The assumption is based on the fact that the temperature factor depends only on the sensor temperature and the cosine error depends on the angle of incident (AOI). In addition, the spectral mismatch factor has a negligible dependence on the tilt angle of the sensor [2], and the calibration factor depends on the level of incident irradiance.

It can be concluded that applying the correction model on the SiS irradiance significantly reduces the differences between the readings of the sensors and makes the SiS more useful as a low-cost instrument to measure GHI.

Nomenclature

GHI	Global Horizontal Irradiance
DHI	Diffuse Horizontal Irradiance
AM	Air Mass
Pyr	Thermopile Pyranometer
SiS	Silicon Sensor
SR	Spectral Response
Δ	difference between cell temperature and STC value (25 °C)
α	temperature coefficient
K_t	Clearness Index
SZA	Solar Zenith Angle
λ	Wavelength of Irradiance
Tf	Temperature factor
MFF	Spectral Mismatch Factor
CosEr	Cosine error
Cf	Calibration factor
T_{sen}	Temperature of Sensor
E	Global Irradiance
SZA_{min}	Minimum Solar Zenith Angle
C_T	Temperature correction
C_s	Spectral correction
C_c	Cosine correction
C_{cal}	Calibration correction
I_{sc}	Short circuit current

References

1. Wright, S. Second Law Analysis of the Earth System with a Radiative Model. *Int. J. Thermodyn.* **2002**, *5*, 57–65.
2. El-Shirbeny, M.A.; Abdellatif, B. Reference evapotranspiration borders maps of Egypt based on kriging spatial statistics method. *Int. J. Geomate* **2017**, *13*, 37. [CrossRef]
3. Spertino, F.; di Leo, P.; Cocina, V. Accurate measurements of solar irradiance for evaluation of photovoltaic power profiles. In Proceedings of the 2013 IEEE Grenoble Conference PowerTech, Powertech 2013, Grenoble, France, 16–20 June 2013.
4. Pereira, G.M.S.; Stonoga, R.L.B.; Detzel, D.H.M.; Küster, K.K.; Neto, R.A.P.; Paschoalotto, L.A.C. Analysis and Evaluation of Gap Filling Procedures for Solar Radiation Data. In Proceedings of the 2018 IEEE 9th Power, Instrumentation and Measurement Meeting, EPIM 2018, Salto, Uruguay, 14–16 November 2018.
5. IPCC. Climate Change 2007-The Physical Science Basis: Working Group I Contribution to the Fourth Assessment Report of the IPCC. *Science* **2007**, *4*, 8117.
6. Kopp, G.; Lean, J.L. A new, lower value of total solar irradiance: Evidence and climate significance. *Geophys. Res. Lett.* **2011**, *1*, 38. [CrossRef]
7. Paulescu, M.; Paulescu, E.; Gravila, P.; Badescu, V. Weather Modeling and Forecasting of PV Systems Operation. *Green Energy Technol.* **2013**, *5*, 232.
8. Wilbert, S.; Geuder, N.; Schwandt, M.; Kraas, B.; Jessen, W.; Meyer, R.; Nouri, B. *Best Practices for Solar Irradiance Measurements with Rotating Shadowband Irradiometers*; International Energy Agency: Paris, France, 2015.
9. Dunn, L.; Gostein, M.; Emery, K. Comparison of pyranometers vs. PV reference cells for evaluation of PV array performance. In Proceedings of the Conference Record of the IEEE Photovoltaic Specialists Conference, Austin, TX, USA, 3–8 June 2012.
10. Meydbray, J.; Riley, E.; Dunn, L.; Emery, K.; Kurtz, S. *Pyranometers and Reference Cells: Part 2: What Makes the Most Sense for PV Power Plants*; National Renewable Energy Lab: Golden, CO, USA, 2012.
11. Azouzoute, A.; Merrouni, A.A.; Bennouna, E.G.; Gennioui, A. Accuracy measurement of pyranometer vs reference cell for PV resource assessment. *Energy Procedia* **2019**, *157*, 1201–1209. [CrossRef]
12. Alados-Arboledas, L.; Batlles, F.J.; Olmo, F.J. Solar radiation resource assessment by means of silicon cells. *Sol. Energy* **1995**, *54*, 183–191. [CrossRef]
13. King, D.L.; Myers, D.R. Silicon-photodiode pyranometers: Operational characteristics, historical experiences, and new calibration procedures. In Proceedings of the Conference Record of the IEEE Photovoltaic Specialists Conference, Anaheim, CA, USA, 3 October 1997.
14. Vignola, F. Removing systematic errors from rotating shadowband pyranometer data. In Proceedings of the American Solar Energy Society-Solar 2006: 35th ASES Annual Conf., 31st ASES National Passive Solar Conference, 1st ASES Policy and Marketing Conf., ASME Solar Energy Division Internationnal Solar Energy Conference, Denver, CO, USA, 13 July 2006.
15. Geuder, N.; Pulvermüller, B.; Vorbrugg, O. Corrections for rotating shadowband pyranometers for solar resource assessment. In Proceedings of the Optical Modeling and Measurements for Solar Energy Systems II, San Diego, CA, USA, 11 September 2008.

16. Forstinger, A. Physically based correction of systematic errors of Rotating Shadowband Irradiometers. *Meteorol. Z.* **2020**. Available online: https://elib.dlr.de/121698/1/__ASFS01_Group_Literature_Database_SolarResearch.Data_PDF_Bachelorthesis_Forstinger-1058268416_Bachelorthesis_Forstinger.pdf (accessed on 21 March 2021). [CrossRef]

17. Mubarak, R.; Hofmann, M.; Riechelmann, S.; Seckmeyer, G. Comparison of modelled and measured tilted solar irradiance for photovoltaic applications. *Energies* **2017**, *10*, 1688. [CrossRef]

18. Mubarak, R.; Luiz, E.W.; Seckmeyer, G. Why PV modules should preferably no longer be oriented to the south in the near future. *Energies* **2019**, *12*, 4528. [CrossRef]

19. International Organization for Standardization. *ISO 9060: Solar Energy-Specification and Classification of Instruments for Measuring Hemispherical Solar and Direct Solar Radiation*; International Organization for Standardization: Geneva, Switzerland, 1990.

20. CMP11 Secondary Standard Pyranometer-Kipp & Zonen. Available online: https://www.kippzonen.com/Product/13/CMP11-Pyranometer#.YFdMeucxlaQ (accessed on 21 March 2021).

21. Vignola, F.; Peterson, J.; Chiu, C.Y.; Dooraghi, M.; Sengupta, M.; Mavromatakis, F. Comparison of pyranometers and reference cells on fixed and one-Axis tracking surfaces. In Proceedings of the ASES SOLAR 2017-46th Annual National Solar Conference, Denver, CO, USA, 9–12 October 2017.

22. Vignola, F.; Peterson, J.; Kessler, R.; Dooraghi, M.; Sengupta, M.; Mavromatakis, F. Evaluation of Photodiode-based Pyranometers and Reference Solar Cells on a Two-Axis Tracking System. In Proceedings of the 2018 IEEE 7th World Conference on Photovoltaic Energy Conversion, WCPEC 2018-A Joint Conference of 45th IEEE PVSC, 28th PVSEC and 34th EU PVSEC, Waikoloa, HI, USA, 10–15 June 2018.

23. King, D.L.; Boyson, W.E.; Hansen, B.R. *Improved Accuracy for Low-Cost Solar Irradiance Sensors*; Sandia National Labs.: Albuquerque, NM, USA, 1997.

24. Myers, D.R.; Emery, K.A.; Stoffel, T.L. Uncertainty estimates for global solar irradiance measurements used to evaluate PV device performance. *Sol. Cells* **1989**, *27*, 455–464. [CrossRef]

25. Si Sensor: Ingenieurbüro Mencke & Tegtmeyer GmbH. Available online: https://www.imt-solar.com/solar-irradiance-sensors/si-sensor/ (accessed on 21 March 2021).

26. Dutton, E.G.; Michalsky, J.J.; Stoffel, T.; Forgan, B.W.; Hickey, J.; Nelson, D.W.; Alberta, T.L.; Reda, I. Measurement of the broadband diffuse solar irradiance using current commercial instrumentation with a correction for thermal offset errors. *J. Atmos. Ocean. Technol.* **2001**, *18*, 297–314. [CrossRef]

27. Reda, I.; Stoffel, T.; Myers, D. A method to calibrate a solar pyranometer for measuring reference diffuse irradiance. *Sol. Energy* **2003**, *74*, 103–112. [CrossRef]

28. Michalsky, J.J.; Harrison, L.; LeBaron, B.A. Empirical radiometric correction of a silicon photodiode rotating shadowband pyranometer. *Sol. Energy* **1987**, *39*, 87–96. [CrossRef]

29. Perraki, V.; Kounavis, P. Effect of temperature and radiation on the parameters of photovoltaic modules. *J. Renew. Sustain. Energy* **2016**, *8*, 013102. [CrossRef]

30. Iqbal, M. *An Introduction to Solar Radiation*; Elsevier: Amsterdam, The Netherlands, 2012.

31. Michalsky, J.J.; Harrison, L.C.; Berkheiser, W.E. Cosine response characteristics of some radiometric and photometric sensors. *Sol. Energy* **1995**, *54*, 397–402. [CrossRef]

32. Zibordi, G.; Bulgarelli, B. Effects of cosine error in irradiance measurements from field ocean color radiometers. *Appl. Opt.* **2007**, *46*, 5529–5538. [CrossRef] [PubMed]

33. Cordero, R.R.; Seckmeyer, G.; Labbe, F. Cosine error influence on ground-based spectral UV irradiance measurements. *Metrologia* **2008**, *45*, 406. [CrossRef]

34. Kipp, Z. Solar Radiation Measurements for Solar Energy Applications. Available online: file:///C:/Users/MDPI/AppData/Local/Temp/KippZonen_Solar_Energy_Guide-1.pdf (accessed on 21 March 2021).

35. Wetter und Klima-Deutscher Wetterdienst-Our Services-Maps of Global Radiation, Monthly and Annual Sum. Available online: https://www.dwd.de/EN/ourservices/solarenergy/maps_globalradiation_sum.html?nn=495490 (accessed on 1 April 2021).

36. Elminir, H.; Benda, V.; Tousek, J. Effects of solar irradiation conditions and other factors on the outdoor performance of photovoltaic modules. *J. Electr. Eng.* **2001**, *52*, 125–133.

37. Shukla, A.K. *Experimental Methods in the Physical Sciences*; Elsevier: Amsterdam, The Netherlands, 2009.

38. Huang, X.; Quan, C.; Kng, J. Comparison of two methods for short circuit current measurement of large size solar cell. In Proceedings of the International Conference on Optical and Photonic Engineering (icOPEN2015), Singapore, 17 July 2015; p. 95242A.

39. Stark, C.; Theristis, M. The impact of atmospheric parameters on the spectral performance of multiple photovoltaic technologies. In Proceedings of the 2015 IEEE 42nd Photovoltaic Specialist Conference (PVSC), New Orleans, LA, USA, 14–19 June 2015; pp. 1–5.

40. Kasten, F.; Young, A.T. Revised optical air mass tables and approximation formula. *Appl. Opt.* **1989**, *28*, 4735–4738. [CrossRef] [PubMed]

41. Mayer, B.; Kylling, A. Technical Note: The libRadtran Software Package for Radiative Transfer Calculations-Description and Examples of Use. *Atmos. Chem. Phys.* **2005**, *5*, 1855–1877. [CrossRef]

42. Amillo, A.M.G.; Huld, T.; Vourlioti, P.; Müller, R.; Norton, M. Application of satellite-based spectrally-resolved solar radiation data to PV performance studies. *Energies* **2015**, *8*, 3455–3488. [CrossRef]

5 Summary and Conclusion

Over the past decades, solar radiation has become a significant means of power production, and its variability became a key factor influencing the terrestrial climate. The most frequently measured component of solar radiation is the global horizontal irradiance. However, solar energy systems are not projected and installed horizontally but at a certain tilt angle to optimize solar radiation collection and to avoid water or dust accumulation. Hence, the actual amount and the spectral distribution of a tilted solar irradiance may well deviate from the measured one on a horizontal surface. Due to the high cost of installing pyranometers with various tilt angles, irradiance data on inclined surfaces are rarely available, and the tilted solar radiation is estimated from horizontal solar data. However, measured data of tilted solar irradiance is required for better understanding of the changes that occur with changing the collector inclination angle. This thesis is based on solar irradiance data collected at different orientations and tilt angles. The measurements have been conducted over many years in Hannover, Germany by using silicon solar sensors (SiS) and thermopile pyranometers (Pyr) in order to investigate the following research objectives:

(1) How accurate are the available transposition models that estimate the global and diffuse solar irradiance on tilted planes?

(2) Is there an alternative concept for increasing self-consumption via the use of other orientations of photovoltaic (PV) systems?

(3) How accurate are the silicon-based irradiance sensors and what is the deviation to thermopile sensors?

In order to answer the first research question, the accuracy of several transposition models that are used in photovoltaic prediction models for estimating the global and diffuse solar irradiance on tilted surfaces was investigated. Five transposition models were selected to estimate the tilted irradiance based on the global and diffuse horizontal irradiance. The selected models are from Liu and Jordan, Klucher, Hay and Davies, Reindl, and Perez. These models were chosen because of their widespread use and available input data. Model performance was examined for seven south-facing PV surfaces tilted at $10°$ intervals between $10°$ and $70°$; and six vertical tilted surfaces facing S, E, W, SE, SW, and N, as well as a horizontally oriented surface. The calculated values were compared with one-minute values from irradiance sensors facing the same orientation and tilt at the city of Hannover, Germany and NREL Golden (CO, USA) in order to produce more significant and spatially applicable results. In addition, the uncertainty caused by using constant albedo value in the calculations was analyzed.

The analysis shows that the anisotropic models overestimate the south-facing irradiance and most of the vertical tilted irradiance. The deviations of the anisotropic models from the measurements increase with increasing the angular distance from the south direction. Conversely, the isotropic model of Liu and Jordan underestimates the tilted irradiance in most directions. The models from Hay and Davies, and Reindl provided the best results for Hannover, when horizontal pyranometer measurements and a constant albedo value of 0.2 are used. For the NREL location, the Perez model provided the best estimates of global tilted irradiance, when measured albedo values are used. The influence of albedo value on the calculated tilted irradiance increases as the tilt angle increases. The use of a constant albedo value of 0.2, which is widely accepted and used in most applications, leads to an increase in the rMAD that ranges between 0.2% and 3.8%, depending on the tilt angle of the receiving surface.

Based on the results achieved within this thesis, it could be recommended the use of the models from Hay and Davies and Reindl to estimate the tilted irradiance for south-facing modules in regions with mainly cloudy conditions and when albedo measurements are not available. Both models provided the best match to the measured data. The Hay and Davies model would also be useful for simulating the vertical surfaces (e.g., facades and glazing), while the Perez model is recommended for sunny sites and when albedo measurements are available. The analysis results helped answer important questions about model uncertainties for calculating the irradiance for differently oriented PV modules.

Temporary energy production is a severe disadvantage of photovoltaic systems because of its fluctuation between low and high levels throughout the day or even non-existence at some times. In contrast, the electricity demand is a continuous process with respect to time. Therefore, PV energy by itself can't provide a reliable power supply and will cause a problem for the distribution grid because of the higher PV energy production around noontime. In addition, PV self-consumption (SC) represents a key issue to achieve high PV system profitability. Nevertheless, increasing the SC may have a positive effect on the distribution grid and makes the production profiles of PV systems connected to the grid smoother. The second research topic discussed the alternative possibility for increasing SC via use of different orientations of photovoltaic (PV) systems other than south. Using the measured irradiance data, the PV energy outputs of 12 solar collectors at various tilt and azimuth angles were analyzed to identify the best orientation of solar panels in the city of Hannover that matches timing of the peak demand on the load profile and to optimize the economic profitability of the system. The results were also compared with the simulated values of two widely used PV software: PVSOL and PVsyst.

The results show that the south-facing PV generator at about 38° gives the highest annual electricity power in Hannover. The monthly optimum tilt angles range between 30° and 70° depending on the sun's height. For the PV systems without feed-in to the grid, the optimum tilt angle is the angle at which the degree of autarky (AD) is at the maximum. For these systems, the results show that the horizontal collectors provided the maximum AD during the hot season, and a tilt of 50° provided the maximum AD during the winter months. In terms of annual AD-value, the 30° tilt represents the optimal tilt angle.

For non-vertical orientations, it could be also concluded that the combinations of E and W at 45° tilt result in the highest SC rate, and a combination of SE and SW at the same tilt result in the highest AD. In addition, the economic analysis of PV systems without feed-in tariff shows that the SE-SW and E-W orientations tilted at 45° are slightly more beneficial, while S orientation has higher Internal Rate of Return for PV systems with feed-in tariff. In light of the continuing decline of feed-in tariff, the advantage of S orientation is decreasing, and our results show that E-W and SE-SW orientations will be more beneficial if feed-in tariff decreases to 7 Ct/kWh or lower.

The calculation assumed a constant price for the feed-in tariff over the day. However, if we consider the general trend to link the price of electricity with the spot market price, so that the price of selling or feeding electricity to the grid changes according to the production and demand, the E-W and SE-SW orientations might become even more beneficial against S-facing PV systems.

Regarding the PV model validation, the results show that both of the tested PV software overestimate the energy production at most studied orientations; the overestimation increases with increasing deviation from the south direction. Moreover, both PV software underestimate SC rate and AD for all studied orientations. These results lead to the conclusion that improvements are necessary when modelling SC and AD.

Since accurate measurements of global irradiance are required for many applications ranging from weather forecasting to climate studies and energy meteorology, the third part of the thesis focus on the irradiance sensors that are usually used in solar measurements. Two commonly used irradiance

sensors, namely thermopile pyranometers and silicon-based sensors, have been presented, and the factors that affect the accuracy of the measurements were discussed.

Thermopile pyranometers are based on the thermoelectric detection principle and widely used in solar irradiance measurements for climatological research and weather monitoring purposes. This is greatly due to its nearly constant spectral sensitivity over the whole solar spectral range; however, these sensors have the drawback of being expensive. A second drawback is its time response, which is typically in the order of 1 to 10 s. This prevents the following of rapid changes of solar irradiance associated with clear/cloudy transitions during partly cloudy conditions. Silicon-based sensors, on the other hand, are based on the photovoltaic effect and used as a low-cost alternative to the thermopile sensors to provide integrated solar resource information for climatological and photovoltaic research. Unlike thermopile sensors, silicon-based sensors have a response time in the range of milliseconds. However, using these sensors as radiation sensors poses some problems associated with their limited and non-uniform spectral response. Another problem is their temperature dependency, which could cause a relevant change in sensitivity during hot days. Moreover, reference solar cells deviate significantly from a true cosine response at larger solar zenith angles. So, both thermopile and silicon-based sensors demonstrate differences in the used technology, measuring principle, and interactions with the incident solar irradiance. These differences cause deviations in the measured irradiance of both sensors.

Thus, as the last part of the thesis, the irradiance data from each sensor were evaluated and four parameters that influence the sensor measurements have been discussed, in particular temperature, cosine error, spectral mismatch, and calibration factor. In order to eliminate the uncertainty caused by these parameters, a correction model based on the analysis was developed and applied to SiS measurements.

The temperature coefficient α, which represents the change in the sensor's output with temperature changes was used to correct the temperature related error. Applying the temperature correction on the SiS measurements increases the measured irradiance in winter months when the cell temperature is below 25°C, while it decreases the SiS irradiance on hot days.

In the next step, the correction model separates the clear sky from cloudy data in order to correct the cosine, spectral, and correction errors because these errors behave differently depending on sky conditions. A combination of the clearness index and SZA is used to separate the clear sky irradiance from measurements under cloudy conditions. The model then applies the cosine correction. The angular response of the SiS was measured in the manufacturer's laboratory and used to correct the clear sky irradiance. In the case of cloudy conditions, global horizontal irradiance is corrected for the cosine error using a correction factor obtained as a fit function through empirical measurements. The influence of the cosine correction appears to be stronger during clear-sky days when beam radiation dominates. The cosine correction corrects the angular losses and increases the measured irradiance, especially at low-sun altitudes. The effect of cosine correction on the SiS irradiance is large compared to temperature and spectral corrections because of the large cosine error of the used sensors. As the next correction, the spectral correction is applied. Spectral correction can increase or decrease the SiS irradiance under clear-sky depending on the air mass. The correction increases the SiS irradiance for AM values below 1.5 (the value used at STC). For AM values above AM1.5, the spectral distribution of the solar irradiance changes in favor of the spectral response of SiS, increasing the measured irradiance; the purpose of spectral correction then is to reduce the measured data.

The model applied as a last correction is the calibration correction that stems from calibration of SiS under STC, which differs from real conditions. The magnitude of this correction in clear-sky days depends on the solar irradiance, with higher values in winter months than in summer months. This correction increases the SiS measurements in clear-sky conditions by 2% - 5% and decreases it by up to 3 % for overcast conditions.

As a result of applying the correction model on the global horizontal irradiance of SiS, the dif-

ferences between the values measured with both sensors have been reduced significantly. The daily rRMSD between SiS and Pyr irradiations decreased from 10.6% to 5.4% after applying the correction model, while the rMAD decreased from 7.4% to 2.5%. The differences in the total annual irradiation decreases from 70 KWh/m^2 (6.5%) to 15 kWh/m^2 (1.5%) by the correction.

After discussing the differences between the two sensors and the advantages and disadvantages of each one of them, the question arises of which sensor is better for measuring solar irradiance. To answer this question, we need firstly to define the purpose of the measurements and determine wheather we aim to measure the total (broadband) solar irradiance or the amount of solar irradiance that is useable for the PV systems. Indeed, thermopile sensors may still be useful for comparing observed broadband irradiance to historic broadband irradiance, especially because most long-term resource datasets contain only broadband irradiance data and, therefore, most resource assessments and initial performance projects are conducted using broadband irradiance data that is measured by thermopile pyranometers.

However, for monitoring a PV solar system and evaluating the actual solar radiation used by the PV cells, the use of silicon-based sensors is more practical. In other words, silicon sensors (reference PV cell) are designed to measure the irradiance that is available to a PV module for conversion into electricity (fuel in). The use of these sensors should reduce uncertainty in performance and the working cost of capital for the plant owner. This leads to decreasing the Levelized Cost of Electricity.

The results presented in the thesis provided more detailed knowledge about the effect of surface orientation on the amount of solar energy that can be collected and improved our understanding of the tilted solar irradiance. It could be concluded that more roof orientations should be taken into account when installing the PV systems. E and W orientations of PV modules, rather than the south orientations, should be supported because they reduce the cost of storing renewable energy regardless of the ownership of the storage facilities and will avoid high noon peaks of solar energy production, which would become a problem for the grid for higher solar power penetration levels. Based on our measurements and analysis, the yearly sum of produced electricity can no longer be the only criterion for the installation of PV modules. Instead, other orientations may be more beneficial for both the owner and the society that uses solar power. The results also showed that the vertical tilted surfaces represent a high potential for PV energy production, and facade PV systems could be an alternative for many people, especially for those with no access to a rooftop.

6 Outlook

During this thesis, solar irradiance measurements at different orientations and tilt angles were conducted using various sensors and techniques, which later were used as a basis for investigating tilted solar irradiance and energy yield in Hannover. There are several possibilities for further work based on the methodology and results in this thesis. Some suggestions are as follows:

- Within the thesis, the silicon-based sensors were used to measure the solar irradiance on south-facing surfaces and several vertical orientations. However, the spectral distribution of solar radiance is affected by clouds and aerosols. This has a significant influence on the performance of silicon-based sensors, where the spectral response of these sensors is wavelength dependent. Therefore, additional spectral measurements are needed to improve our knowledge about the spectral distribution of solar irradiance under different sky conditions, and for advances in the modelling of PV yields.

- We studied the economic efficiency of non-vertical orientations for the cases with and without FIT. However, the combinations between vertical surfaces (facade PV installation) were not included in this work. The results show that the vertical tilted surfaces represent a high potential for PV energy production. Calculating the performance of vertical tilted surfaces is actually more complicated than the rooftop installation because of the shadow caused by nearby buildings, trees, and other obstacles. It would be feasible to research the vertical-vertical and 40°-vertical combinations, taking the influence of shadow into consideration.

- An empirical model for correcting the SiS irradiance data was presented within this thesis. The model was able to improve the global horizontal irradiance and reduce the deviation to the thermopile sensor. However, the accuracy of the model for correcting tilted irradiance was not tested due to the unavailability of thermopile measurements on inclined surfaces. We assumed that this model can be also used to correct the SiS irradiance measured on inclinded surfaces; in particular, the temperature factor depends only on the sensor temperature and the cosine error depends on the angle of incident (AOI). However, this need to be tested, before circulating the use of the model for the tilted irradiance. Therefore, thermopile pyranometer measurements on tilted surfaces should be conducted and compared to the corrected SiS data to evaluate and validate the correction model.

Bibliography

[1] Belessiotis, V.G. *Availability of Solar Radiation and its Estimation*. Renewable Enerdy Systems and Desalination, 2001. Sub-Chapters 10.2.1.1 to 10.2.1.6, Eolss (Encyclopedia of life support system).

[2] Qiang, F. U. Radiation (solar). *Elsevier Science*, 81:1859–1863, 2003.

[3] Wald, L. Basics in Solar Radiation at Earth Surface. working paper or preprint, 2018.

[4] Meftah, M.; Dame, L.; Bolsee, D.; Hauchecorne, A.; Pereira, N., Sluse, D.; Cessateur, G.; Irbah, A.; Bureau, J.; Weber, M.; Bramstedt, K.; Hilbig, T.; Thieblemont, R.; Marchand, M.; Lefevre1, F. Sarkissian, A.; Bekki, S. A new reference spectrum based on SOLAR/SOLSPEC observations. *Astronomy and Astrophysics*, 611:1108–1110, 2018.

[5] Liang, S. ; Wang, J. Chapter 5- Solar radiation. In *Advanced Remote Sensing-Second Edition*, pages 157–191. Academic Press, Second Edition edition, 2020.

[6] Sanderson, M. *Prevailing trade winds : climate and weather in Hawaii*. University of Hawaii Press, 1993.

[7] . G173-03: Standard tables for reference solar spectral irradiances-direct normal and hemispherical on 37 tilted surface. 2003.

[8] Dornelles, K. A.; Roriz, M.; Roriz,V.; Caram, R. Thermal Performance of White Solar-Reflective Paints for Cool Roofs and the Influence on the Thermal Comfort and Building Energy Use in Hot Climates. 2011.

[9] Sen, Z. *Solar energy fundamentals and modeling techniques: atmosphere, environment, climate change and renewable energy*. Springer Science & Business Media, 2008.

[10] Vita-Finzi C. *The Sun Today* . Springer, 2000.

[11] Klassen, S.; Bugbee, B. *Shortwave Radiation*. American Society of Agronomy, 2005.

[12] Wright, S. Second Law Analysis of the Earth System with a Radiative Model. *International Journal of Thermodynamics*, 5:57–65, 2002.

[13] Seckmeyer, G.; Bais, A.; Bernhard, G.; Blumthaler, M.; Lantz, K.; McKenzie, R.L.; Kiedron, P.; Drüke, S.; Riechelmann, S. Instruments to measure solar ultraviolet radiation, part4 Array Spectrometers. *WMO-GAW report 191*, TD:5038, 2010.

[14] Koussa, M.; Saheb-Koussa, D.; Hamane, M.; Boussaa, Z.; Lalaoui, M. A. Effect of a daily flat plate collector orientation change on the solar system performances. *2016 7th International Renewable Energy Congress (IREC)*, pages 1–6, 2016.

[15] Demain, C.; Journee, M.; Bertrand, C. Evaluation of different models to estimate the global solar radiation on inclined surfaces. *Renewable Energy*, 50:710 – 721, 2013.

[16] Khatib, T. ; Mohamed, A. ; Mahmoud, M.; Sopian, K. Optimization of the Tilt Angle of Solar Panels for Malaysia. *Energy Sources, Part A: Recovery, Utilization, and Environmental Effects*, 37:606 – 613, 2015.

[17] Meyer, R.; Schlecht, M.; Chhatbar, K. Solar resources for concentrating solar power (CSP) systems. *Oxford; Philadelphia : Woodhead Publishing*, 2012.

[18] Bhattacharya, A.B.; Kar, S.K.; Bhattacharya, R. Diffuse solar radiation and associated meteorological parameters in India. *Copernicus GmbH*, 14(10):1051–1059, 1996.

[19] Toledo, C. ; Amillo, A. G.; Bardizza, G.; Abad, J.; Urbina, A. Evaluation of Solar Radiation Transposition Models for Passive Energy Management and Building Integrated Photovoltaics. *Energies*, 13:702, 2020.

[20] Ineichen, P.; Perez, R.; Seal, R.; Maxwell, E.; Zalenka, A. Dynamic global-to-direct irradiance conversion models. *Ashrae Transactions*, 98:354–369, 1992.

[21] Polo, J. ; Gaston, M.; Vindel, J.M. ; Pagola, I. Spatial variability and clustering of global solar irradiation in Vietnam from sunshine duration measurements. *Renewable and Sustainable Energy Reviews*, 42:1326–1334, 2015.

[22] Wild, M.; Folini, D.; Schaer, C.; et al. The global energy balance from a surface perspective. *Clim Dyn*, 40:3107–3134, 2013.

[23] Eltbaakh, Y. A. ; Ruslan, M.H. ; Alghoul, M.A. ; Othman, M.Y.; Sopian, K. ; Razykov, T.M. Solar attenuation by aerosols: An overview. *Renewable and Sustainable Energy Reviews*, 16(6):4264–4276, 2012.

[24] Bais, A.F.; Lubin, D.; Arola, A.; Bernhard, G.; Blumthaler, M., Chubarova, N., Erlick, C., Gies, H.P., Krotkov, N., Lantz, K.; Mayer, B.; McKenzie, R.L.; Piacentini, R.D.; Seckmeyer, G.; Slusser, J.R.; Zerefos, C.S. Surface Ultraviolet Radiation: Past, Present, and Future. *WMO/UNEP ozone assessment*, WMO():, 2007.

[25] Saffaripour, M.H. ; Mehrabian, M.A. Numerical methods applied to global solar radiation modeling-comparison with measured data. *International Journal of Numerical Methods for Heat & Fluid Flow*, 2009.

[26] Riordan, C. J. ; Hulstrom, R. L. ; Myers, D. R. Influences of atmospheric conditions and air mass on the ratio of ultraviolet to total solar radiation. *Solar Energy Research Inst., Golden, CO (USA)*, 6344084(DOE/CE), 8 1990.

[27] Cronin, T.W. ;Johnsen, S.; Marshall, N.J.; Warrant, E.J. *Visual Ecology: 2. Light and the Optical Environment*. Princeton University Press, 2014.

[28] Psiloglou, B.E. ; Santamouris, M. ; Asimakopoulos, D.N. Predicting the broadband transmittance of the uniformly mixed gases (CO2, CO, N2O, CH4 and O2) in the atmosphere, for solar radiation models. *Renewable Energy*, 6(1):63–70, 1995.

[29] Sambo, A. S; Doyle, M.D.C. Estimation of the Global and DiffuseComponents of Solar Radiation for some Nigerian Cities. *Nigerian Journal of Solar Energy*, 5:16–24, 1986.

[30] Fröhlich, C. ; Shaw, G. E. New determination of Rayleigh scattering in the terrestrial atmosphere. *Applied Optics*, 19(11):1773–1775, 1980.

[31] Tang, J.W. ; Li, Y. ; Eames, I. ; Chan, P.K.S.; Ridgway, G.L. Factors involved in the aerosol transmission of infection and control of ventilation in healthcare premises. *Journal of Hospital Infection*, 64(2):100–114, 2006.

[32] Stefanutti, L. ; Di Donfrancesco, G. ; Cairo, F. Airborne Instrumentation for Aerosol Measurements. *Encyclopedia of Analytical Chemistry: Applications, Theory and Instrumentation*, 2006.

[33] Lang-Yona, N. ; Abo-Riziq, A. ; Erlick, C. ; Segre, E.; Trainic, M. ; Rudich, Y. Interaction of internally mixed aerosols with light. *Physical Chemistry Chemical Physics*, 12(1):21–31, 2010.

[34] Ångström, A. On the Atmospheric Transmission of Sun Radiation and on Dust in the Air. *Geografiska Annaler*, 11:156–166, 1929.

[35] Mie, G. Articles on the optical characteristics of turbid tubes, especially colloidalmetal solutions. *Annalen der Physik*, 25(3):377–445, 1908.

[36] Johnson, B.T. ; Shine, K.P. ; Forster, P.M. The semi-direct aerosol effect: Impact of absorbing aerosols on marine stratocumulus. *Quarterly Journal of the Royal Meteorological Society*, 130(599):1407–1422, 2004.

[37] Menon, S.; Hansen, J.; Nazarenko, L. ; Luo, Y. Climate effects of black carbon aerosols in China and India. *Science*, 297(5590):2250–2253, 2002.

[38] Koren, I. ; Martins, J V. ; Remer, L. A. ; Afargan, H. Smoke invigoration versus inhibition of clouds over the Amazon. *Science New York*, 321(5891):946–949, August 2008.

[39] Badescu; V.; Dumitrescu, A. New models to compute solar global hourly irradiation from point cloudiness. *Energy Conversion and Management*, 67:75–91, 2013.

[40] Turner, D. D.; Vogelmann, A. M.; Austin, R. T.; Barnard, J. C. ; Cady-Pereira, K. ; Chiu, J. C.; Clough, S. A.; Flynn, C.; Khaiyer, M. M.; Liljegren, J.; Johnson, K.; Lin, B.; Long, C.; Marshak, A. ; Matrosov, S. Y. ; McFarlane, S. A. ; Miller, M.; Min, Q. ; Minimis, P.; OHirok, W.; Wang, Z.; Wiscombe, W. Thin Liquid Water Clouds: Their Importance and Our Challenge. *Bulletin of the American Meteorological Society*, 88(2):177 – 190, 01 Feb. 2007.

[41] Hansen, J. E. ; Travis, L. D. Light scattering in planetary atmospheres. *Space Sci. Rev.*, 16:527–610, 1974.

[42] Sanchez, G.; Serrano, A.; Cancillo, M.L. Effect of cloudiness on solar global, solar diffuse and terrestrial downward radiation at Badajoz(Southwestern Spain). *Optica Pura y Aplicada*, 45(1):33–38, 2012.

[43] Kokhanovsky, A. Optical properties of terrestrial clouds. *Earth-Science Reviews*, 64(3-4):189–241, 2004.

[44] Mayer, B.; Kylling, A. Technical note: The libRadtran software package for radiative transfer calculations- description and examples of use. *Atmospheric Chemistry and Physics*, 5(7):1855–1877, 2005.

[45] Kasten, F.; Young, A. T. Revised optical air mass tables and approximation formula. *Appl. Opt.*, 28(22):4735–4738, 1989.

[46] Morton, O. Solar energy: a new day dawning? Silicon Valley sunrise. *Nature*, 443(7107):19–22, September 2006.

[47] Rai, G.D. *Solar Energy Utilisation*, page 44. Khanna Publishers, 1980.

[48] PVGIS. The European Commission's science and knowledge service. https://ec.europa.eu/jrc/en/pvgis, 2020. (accessed on 21 December 2020).

[49] Nogueira,C. E. C. ; Bedin, J. ; Niedzialkoski, R. K.; deSouza, S. N. M.; das Neve, J. C. M. Performance of monocrystalline and polycrystalline solar panels in a water pumping system in Brazil. *Renewable and Sustainable Energy Reviews*, 51:1610–1616, 2015.

[50] Kou, Q. ; Klein, S.A. ; Beckman, W.A. A method for estimating the long-term performance of direct-coupled PV pumping systems. *Solar Energy*, 64(1):33–40, 1998.

[51] Carstensen, J. ; Popkirov,G. ; Bahr, J. ; Foell, H. CELLO: an advanced LBIC measurement technique for solar cell local characterization. *Solar Energy Materials and Solar Cells*, 76(4):599–611, 2003.

[52] Li, D.H.W. ; Cheung, G.H.W. ; Lam, J.C. Analysis of the operational performance and efficiency characteristic for photovoltaic system in Hong Kong. *Energy Conversion and Management*, 46:1107–1118, 2005.

[53] Castaner, L. ; Silvestre, S. *Modelling photovoltaic systems using PSpice*. John Wiley and Sons, 2002.

[54] Bentham . Technical Note: Spectral Characterisation of Photovoltaic Devices. *Bentham*, 2014.

[55] Fernandez,E. F. ; Soria-Moya, A. ; Almonacid, F. ; Aguilera, J. Comparative assessment of the spectral impact on the energy yield of high concentrator and conventional photovoltaic technology. *Solar Energy Materials and Solar Cells*, 147:185–197, 2016.

[56] Emery, K. Measurement and characterization of solar cells and modules. *Handbook of photovoltaic science and engineering*, pages 738–745, 2003.

[57] Dirnberger, D. ; Blackburn, G. ; Mueller, B.; Reise, C. On the impact of solar spectral irradiance on the yield of different PV technologies. *Solar Energy Materials and Solar Cells*, 132:431–442, 2015.

[58] Sharaf, O. Z.; Taylor, R. A.; Abu-Nada, E. On the colloidal and chemical stability of solar nanofluids: From nanoscale interactions to recent advances. *Physics Reports*, 867:1–84, 2020.

[59] Mubarak, R.; Hofmann, M.; Riechelmann, S. ; Seckmeyer, G. Comparison of modelled and measured tilted solar irradiance for photovoltaic applications. *Energies*, 10(11):1688, 2017.

[60] Mubarak, R.; Luiz E. W. ; Seckmeyer, G. Why PV modules should preferably no longer be oriented to the south in the near future. *Energies*, 12:4528, 2019.

[61] Mubarak, R.; Schilke, H.; Seckmeyer, G. Improving the irradiance data measured by silicon-based sensors. *Energies*, 10(11):1688, 2021.

[62] Alados-Arboledas, L.; Batlles, F.J.; Olmo, F.J. Solar radiation resource assessment by means of silicon cells. *Solar Energy*, 54(3):183–191, 1995.

[63] Dooraghi, M.R.; Sengupta, M.; Vignola, F.; Peterson, J.; Mavromatakis, F.; Chiu, C-Y. Comparison of Pyranometers and Reference Cells on Fixed and One-axis Tracking Surfaces. *ASES National Solar Conference 2017 Proceedings*, NREL/CP-5D00-70285(), 2017.

[64] Kipp & Zonen. Solar Radiation Measurements. Available online:https://www.kippzonen.com/, 2020. (accessed on 01 April 2021).

[65] Kipp & Zonen. Instruction Manual,CMP series Pyranometer. Available online:https://www.kippzonen.com/Download/73/Instruction-Sheet-Pyranometers-CMP-series?ShowInfo=true, 01 2013. (accessed on 15 May 2021).

[66] Kerr, J. P.; Thurtell, C. B.; Tanner, C. B. An integrating pyranometer for climatological observer stations and mesoscale networks. *J Appl Meteorol*, 6:688–694, 1967.

[67] Michalskv, J. J.; Harrison, L.; LeBaron, B. A. Empirical radiometric correction of a silicon photodiode rotating shadowband pyranometer. *Solar Energy*, 39:87–96, 1987.

[68] Meydbray, J.; Riley, E.; Dunn, L.; Emery, K.; Kurtz, S. Pyranometers and Reference Cells: Part 2: What Makes the Most Sense for PV Power Plants? *PV Magazine*, (), 10 2012.

[69] Vignola, F.; Peterson, J.; Kessler, R.; Dooraghi, M.; Sengupta, M.; Mavromatakis, F. Evaluation of Photodiode-Based Pyranometers and Reference Solar Cells on a Two-Axis Tracking System. In *2018 IEEE 7th World Conference on Photovoltaic Energy Conversion (WCPEC)(A Joint Conference of 45th IEEE PVSC, 28th PVSEC & 34th EU PVSEC)*, pages 2376–2381. IEEE, 2018.

[70] Ingenieurbüro Mencke & Tegtmeyer GmbH. Solar Irradiance Sensors. Available online:https://www.imt-solar.com/solar-irradiance-sensors/si-sensor, 2020. (accessed on 15 May 2021).

[71] Lave, M.; Hayes, W.; Pohl, A.; Hansen, C. Evaluation of Global Horizontal Irradiance to Plane-of-Array Irradiance Models at Locations Across the United States. *IEEE Journal of Photovoltaics*, 5:597–606, 2015.

[72] Kerr, J. P.; Thurtell, C. B.; Tanner, C. B. Correction Methods for Thermal Offset Errors in TBQ-2-B Pyranometers. *Journal of Tropical Meteorology*, 20(4):376–385, 2014.

[73] Dutton, G.; Michalssky, J.; Stoffel, T.; Forgan, B.; Hickey, J.; Nelson, D.; Alberta, T.; Reda, I. Measurement of Broadband Diffuse Solar Irradiance Using Current Commercial Instrumentation with a Correction for Thermal Offset Errors. *Journal of Atmospheric and Oceanic Technology*, 18:297–314, 2001.

[74] Reda, I. ; Myers, D. A Method to Calibrate a Solar Pyranometer for Measuring Reference Diffuse Irradiance. *Solar Energy*, 74:103–112, 2003.

[75] King, D. L.; Myers, D. Silicon-photodiode pyranometers: operational characteristics, historical experiences, and new calibration procedures. *Conference Record of the Twenty Sixth IEEE Photovoltaic Specialists Conference-1997*, :1285–1288, 1997.

[76] Perraki, V. ; Kounavis, P. Effect of temperature and radiation on the parameters of photovoltaic modules. *Journal of Renewable and Sustainable Energy*, 8:013102, 2016.

[77] Javed, A. The effect of temperatures on the silicon solar cell. *International Journal of Emerging Technologies in Computational and Applied Sciences (IJETCAS)*, 2:305–308, 2014.

[78] Elminir, H. K.; Benda, V.; Touvsek, J. Effects of solar irradiation conditions and other factors on the outdoor performance of photocoltaic modules. *Journal of Electrical Engeneering*, 52:125–133, 2001.

[79] Bais, A.F.; Kazadzis, S.; Balis, D.; Zerefos, C.S.; Blumthaler, M. Correcting global solar ultraviolet spectra recorded by a Brewer spectroradiometer for its angular response error. *Appl. Opt.*, 37(27):6339–6344, Sep 1998.

[80] Michalsky, J.J.; Harrison, L.C.; Berkheiser, W.E. Cosine response characteristics of some radiometric and photometric sensors. *Solar Energy*, 54(6):397–402, 1995.

[81] Driesse, A.; Zaaiman, W.; Riley, D.; Taylor, N.; Stein, J. S. Indoor and Outdoor Evaluation of Global Irradiance Sensors. *31st European Photovoltaic Solar Energy Conference and Exhibition*, Germany, 2015.

[82] Nann, S. Potentials for tracking photovoltaic systems and V-troughs in moderate climates. *Solar Energy*, 45(6):385–393, 1990.

[83] Hirata, Y.; Tani, T. Evaluation of photovoltaic modules considered spectral solar radiation, 1993.

[84] Garg, H. P. ; Meinel, A. Treatise on Solar Energy, Volume 1: Fundamentals of Solar Energy. *Journal of Solar Energy Engineering*, 106(3):376–377, 08 1984.

[85] Duffie, J. A.; Beckman, W. A. *Solar engineering of thermal processes*. John Wiley & Sons: New York, NY,USA, 1991.

[86] Hailu, G.; Fung, A. S. Optimum tilt angle and orientation of photovoltaic thermal system for application in greater Toronto area, Canada. *Sustainability*, 11(22):6443, 2019.

[87] Balcombe, P.; Rigby, D. ; Azapagic, A. Energy self-sufficiency, grid demand variability and consumer costs: Integrating solar PV, Stirling engine CHP and battery storage. *Applied Energy*, 155:393–408, 2015.

Acknowledgments

This PhD thesis is the result of the effort and support of several people, to whom I am extremely grateful. I would like to thank my supervisor, Prof. Dr. Gunther Seckmeyer, for giving me the opportunity to write this thesis, and for all his valuable support over the years. Without his guidance and constant feedback, this PhD would not have been achievable.

Furthermore, I would like to thank all of the members of the Radiation and Remote Sensing workgroup for their support. Special thanks to Holger Schilke, Stefan Riechelmann, Cristian Crisosto, Martin Hoffman, and Eduardo Luiz. I wish you all the best.

There have, of course, been many others who have helped with my work, so I must thank the following people for their time and input: Maan Sabagh, Max Rose, and Zaid Qarout.

This acknowledgment would not be complete without the mention of my family for their patience, continuous encouragement, and support. My wife has supported me throughout this entire process and has made countless sacrifices to help me get to this point. She also supported the family during much of my studies. Along with her, I want to acknowledge my daughter and my sons. They have never known their dad as anything but a student, it seems.

My parents and my brothers deserve special thanks for their continued support and encouragement. Without such a strong team behind me, I doubt that I would be in this place today.

Curriculum Vitae

Personal Details	Family Name First Name Date of birth Place of birth	Mubarak Riyad 04 October 1969 Alnusairat, Palestine
Career	Since 05/2016	**Senior Meteorologist** at WeatherTec GmbH, Germany
	04/2010 - 01/2012	**Meteorologist** at Meteo System International AG, Switzerland
Academic Career	09/2013 - 04/2016	**Research associate** at the Institute of Meteorology and Climatology, Leibniz Universität Hannover, Germany
	07/2006 - 03/2010	**Research associate** at the Institute of Meteorology and Climatology, Leibniz Universität Hannover, Germany
University Education	05/2006	**German "Diplom" in meteorology**. Final grade: magna cum laude (1.5). Diploma thesis on "Geographische Unterschiede der spektralen Bestrahlungsstärke in Hannover und am Toten Meer- Vorbereitende Messungen und Modellrechnungen".
	10/1998 - 05/2006	**Studies in Meteorology**, Leibniz Universität Hannover, Germany
	10/1989 - 05/1994	**Studies in Physics**, Universita of Garyounis, Benghazy, Libya.

Publications	**Mubarak, R.; Schilke, H.; Seckmeyer, G.**: Improving the Irradiance Data Measured by Silicon-Based Sensors. Energies 2021, 05, 4528. https://doi.org/10.3390/en14102766

Mubarak, R.; Weide Luiz, E.; Seckmeyer, G.: Why PV Modules Should Preferably No Longer Be Oriented to the South in the Near Future. Energies 2019, 12, 4528. https://doi.org/10.3390/en12234528, 2019.

Crisosto, C.; Hofmann, M.; Mubarak, R.; Seckmeyer, G.: One-Hour Prediction of the Global Solar Irradiance from Allsky-Images using Artificial Neural Networks. Special Issue Solar and Wind Energy Forecasting, Energies, DOI: 10.3390/en11112906, 2018.

Mubarak, R.; Hofmann, M.; Riechelmann, S.; Seckmeyer, G., Comparison of Modelled and Measured Tilted Solar Irradiance for Photovoltaic Applications, Energies, vol. 10, no. 11, p. 1688, Oct. http://www.mdpi.com/1996-1073/10/11/1688, 2017.

Cordero, R.R.; Damiani, A.; Seckmeyer, G.; Jorquera, J.; Caballero, M.; Rowe, P. Ferrer, J.; Mubarak, R.; Carrasco, J.; Rondanelli, R.; Matus, M. Laroze, D.: The solar Spectrum in the Atacama Desert, Scientific Reports DOI: 10.1038/srep22457, 2016.

Hofmann, M.; Riechelmann, R.; Crisosto, C.; Mubarak, R.; Seckmeyer, G.: Improved synthesis of global irradiance with one-minute resolution for PV system simulations, International Journal of Photoenergy, DOI: 10.1155/2014/808509, 2014.